

See discussions, stats, and author profiles for this publication at: <https://www.researchgate.net/publication/348806406>

# Study of the quantum interference between singly and doubly resonant top-quark production in proton–proton collisions at the LHC with the ATLAS detector

Thesis · December 2020

DOI: 10.13140/RG.2.2.34038.42561

---

CITATIONS

0

READS

252

1 author:



Gianluca Bianco

University of Bologna

4 PUBLICATIONS 0 CITATIONS

SEE PROFILE

ALMA MATER STUDIORUM · UNIVERSITY OF BOLOGNA

---

---

School of Science  
Department of Physics and Astronomy  
Master Degree in Physics

**Study of the quantum interference between  
singly and doubly resonant top-quark  
production in proton-proton collisions at  
the LHC with the ATLAS detector**

**Supervisor:**  
Prof. Maximiliano Sioli

**Submitted by:**  
Gianluca Bianco

**Co-supervisor:**  
Dott. Marino Romano

Academic Year 2019/2020



*“Our virtues and our failures are inseparable, like force and matter. When they separate, man is no more.”*

---

Nikola Tesla

*To all those who have never stopped believing in their dreams.*



## Abstract

The top quark is the heaviest known elementary particle of the Standard Model. Thanks to its particular properties, it allows to explore unique physics domains, inaccessible otherwise. One of them is the quantum interference between singly ( $tW$ ) and doubly ( $t\bar{t}$ ) resonant top quark production in proton-proton collisions, which can lead to identical  $WbWb$  final-states when an additional  $b$ -quark is radiated during a singly-resonant production. Studying this process is very important for a better knowledge of the Standard Model, but also to investigate some Beyond the Standard Model processes: for example, the search for top squarks suffers a large background contamination from  $tW$  and  $t\bar{t}$  in the interference region.

In this work, the measurement of the particle-level differential cross-section of the  $WbWb$  final-state in the  $e\mu$  dilepton channel is provided, in order to better investigate the interference-sensitive region of these processes. The measurement is performed using the full dataset collected by the ATLAS detector from proton-proton collisions at the LHC during Run-2 at  $\sqrt{s} = 13$  TeV corresponding to an integrated luminosity of  $139 \text{ fb}^{-1}$ . The differential cross-section has been measured as a function of two interference-sensitive variables, defined as  $m_{bl}^{\minimax}$  and  $\Delta R(b_1, b_2)$ . Besides the single-differential cross-sections as a function of  $m_{bl}^{\minimax}$  and  $\Delta R(b_1, b_2)$ , also the double-differential cross-section as a function of  $m_{bl}^{\minimax}$  in bins of  $\Delta R(b_1, b_2)$  is measured.

The  $WbWb$  differential cross-section has been successfully extracted and compared to different schemes: the Diagram Removal and the Diagram Subtraction. This two predictions model in a different way the quantum interference description.



# Contents

<b>Introduction</b>	<b>1</b>
<b>1 Physical foundations</b>	<b>3</b>
1.1 The Standard Model of particle physics . . . . .	3
1.1.1 Particles and forces classification . . . . .	4
1.1.2 Quantum Electrodynamics (QED) . . . . .	5
1.1.3 Quantum Flavordynamics (QFD) . . . . .	7
1.1.4 Quantum Chromodynamics (QCD) . . . . .	9
1.1.5 Electroweak theory . . . . .	11
1.2 Top quark physics . . . . .	13
1.2.1 The top particle . . . . .	13
1.2.2 Fundamental properties of top quark . . . . .	15
1.2.3 Impacts of top quark in SM and BSM physics . . . . .	18
1.3 The quantum interference between $t\bar{t}$ and $tW$ production processes . . . . .	21
1.3.1 Top pair production process: $t\bar{t}$ . . . . .	21
1.3.2 Single top production process: $tW$ . . . . .	23
1.3.3 Quantum interference between $t\bar{t}$ and $tWb$ processes . . . . .	26
1.3.4 Interference term in BSM context . . . . .	29
1.3.5 State-of-the-art of the measurements . . . . .	31
<b>2 The ATLAS detector</b>	<b>33</b>
2.1 The LHC collider . . . . .	33
2.1.1 Luminosity . . . . .	35
2.1.2 Magnets . . . . .	37
2.1.3 Beam injection and acceleration . . . . .	38
2.2 The ATLAS detector at the LHC . . . . .	39
2.2.1 Detector reference frame and requirements . . . . .	41
2.2.2 Magnet system . . . . .	43
2.2.3 Tracking system . . . . .	45
2.2.4 Calorimetry . . . . .	46
2.2.5 Muon spectrometer . . . . .	48

2.2.6	Trigger and data acquisition system . . . . .	50
<b>3</b>	<b>Objects reconstruction</b>	<b>52</b>
3.1	Electron reconstruction . . . . .	52
3.1.1	Electron identification . . . . .	54
3.1.2	Electron isolation . . . . .	55
3.1.3	Electron triggers . . . . .	58
3.2	Muon reconstruction . . . . .	59
3.2.1	Muon identification . . . . .	60
3.2.2	Muon isolation . . . . .	61
3.2.3	Muon triggers . . . . .	61
3.3	$\tau$ -lepton reconstruction . . . . .	62
3.3.1	$\tau$ -identification and triggers . . . . .	64
3.4	Jet reconstruction and calibration . . . . .	65
3.4.1	$b$ -tagging algorithms . . . . .	66
3.4.2	Jet triggers . . . . .	67
3.5	Missing Transverse Energy (MET) reconstruction . . . . .	69
3.5.1	Missing Transverse Energy (MET) triggers . . . . .	69
3.6	Overlap removal . . . . .	71
<b>4</b>	<b>Differential cross-section measurement in the dilepton channel</b>	<b>73</b>
4.1	Data and Monte Carlo samples . . . . .	73
4.1.1	Data sample . . . . .	74
4.1.2	Monte Carlo simulated samples . . . . .	74
4.2	Event selection . . . . .	76
4.2.1	Control plots . . . . .	77
4.3	Particle-level objects . . . . .	81
4.3.1	Particle-level selection . . . . .	82
4.4	Studied observables . . . . .	82
4.4.1	The $m_{bl}^{\text{minimax}}$ variable . . . . .	82
4.4.2	The $\Delta R(b_1, b_2)$ . . . . .	83
4.5	Analysis strategy . . . . .	83
4.5.1	Unfolding procedure . . . . .	84
4.5.2	Binning choice and resolution studies . . . . .	87
4.5.3	Closure tests . . . . .	91
4.6	Systematic uncertainties . . . . .	94
4.6.1	Detector related systematics . . . . .	94
4.6.2	Signal modelling . . . . .	95
4.6.3	Systematic uncertainties summary . . . . .	95
4.7	Results . . . . .	98

<b>Conclusions and outlook</b>	<b>101</b>
<b>A Physical foundations complements</b>	<b>103</b>
A.1 Dirac and Pauli matrices . . . . .	103
A.2 Cross section theory and perturbative expansions . . . . .	104
<b>B Object reconstruction complements</b>	<b>107</b>
B.1 Jet trigger efficiencies plots . . . . .	107
<b>C Differential cross-section measurement complements</b>	<b>109</b>
C.1 Study of the impact parameters of final-state lepton tracks . . . . .	109
C.2 Resolution plots and binning choice complements . . . . .	114
C.2.1 Resolution plots for $t\bar{t}$ and $tW$ . . . . .	114
C.2.2 Binning and resolution plots for $\Delta R(b_1, b_2)$ in bins of $m_{bl}^{\text{minimax}}$ . .	118
C.3 Closure tests for $\Delta R(b_1, b_2)$ in bins of $m_{bl}^{\text{minimax}}$ . . . . .	120
C.4 Systematic uncertainties not used in the analysis . . . . .	121
<b>Acknowledgments</b>	<b>123</b>
<b>List of Figures</b>	<b>126</b>
<b>List of Tables</b>	<b>135</b>
<b>Bibliography</b>	<b>136</b>

# Introduction

The Standard Model (SM) of particle physics is, at the moment, the most complete theory to describe matter particles and their interactions. In the SM, the heaviest elementary particle known so far is the top quark.

The study of the top quark physics is a fundamental particle physics topic nowadays; it is useful not only for a better understanding of the SM, but also to explore proposed Beyond the Standard Model (BSM) physics. The top quark represents one of the fundamental building blocks of our universe and is significantly different with respect to other particles. Due to its large mass, it may undergo some kind of processes that can't be seen with the other lightest particles.

An interesting process to study is the quantum interference between singly ( $tWb$ ) and doubly ( $t\bar{t}$ ) resonant top quark production that can be studied in proton-proton collisions (at the LHC for example). At the next-to-leading-order (NLO) QCD corrections, the cross-section for a process with initial-state particles  $\alpha$  and  $\beta$  that gives products  $t$ ,  $W$  and  $b$  is proportional to the amplitude:

$$|\mathcal{A}_{\alpha\beta}|^2 = \left| \mathcal{A}_{\alpha\beta}^{(Wt)} \right|^2 + \left| \mathcal{A}_{\alpha\beta}^{(t\bar{t})} \right|^2 + 2 \operatorname{Re} \{ \mathcal{A}_{\alpha\beta}^{(Wt)} \mathcal{A}_{\alpha\beta}^{(t\bar{t})} \}$$

The first term is associated to the singly resonant diagrams (where only one top quark is on-shell), the second one is related to the doubly resonant diagrams and the last one is the quantum interference between singly and doubly resonant top-quark production. The interference is caused by the identical final states  $WbWb$  of both terms. The measurements of the interference region can be performed considering the dilepton channel final states of the  $WbWb$  decay, in particular the channel with a pair of oppositely charged (OS) light leptons ( $ee$ ,  $e\mu$  and  $\mu\mu$ ), originating from  $W$  and  $\tau$  decays.

The experimental measurement of this interference term is fundamental test for the SM, but it also aim at improving particular BSM searches: where background regions are enriched in  $Wt$  events in the interference region. For example, these regions need to be deeply understood in order to discriminate signal from background in several SUSY searches. This measurement can also help to solve a similar problem in  $t\bar{t}H$  vs.  $tWH$  or  $t\bar{t}\gamma$  vs.  $tW\gamma$  processes.

The LHC is the largest and most powerful particle accelerator in the world, at the moment. It hosts four main experiments and one of them is ATLAS.

Here we present the measurement of the single-differential (1D) and double-differential (2D)  $WbWb$  cross-sections in the  $e\mu$  channel at the particle level. For this analysis we considered only the OS  $e\mu$  final-state for two reasons: firstly, this channel, among all the dileptonic final-states, allows to strongly suppress the  $Z \rightarrow ll$  background and secondly, because we expect the  $2b4l$  predictions be  $e\mu$  only. This measurement has been performed on the full data collected by ATLAS from proton-proton collisions at the LHC, during the Run-2, at  $\sqrt{s} = 13$  TeV corresponding to an integrated luminosity of  $139\text{ fb}^{-1}$ . The differential cross-section has been measured as a function of two interference-sensitive variables, named  $m_{bl}^{\text{minimax}}$  and  $\Delta R(b_1, b_2)$ , by using an iterative Bayesian unfolding procedure. In particular, the measurement has been performed for 1D  $m_{bl}^{\text{minimax}}$  and  $\Delta R(b_1, b_2)$  and for 2D  $m_{bl}^{\text{minimax}}$  in bins of  $\Delta R(b_1, b_2)$ .

The thesis is structured as follows:

- **Chapter 1:** here the physical foundations of the measurement are explained. Firstly, the SM of microcosm is introduced, than the top quark particle is presented and finally the quantum interference between  $t\bar{t}$  and  $tW$  is described from a theoretical point of view. Complements to this chapter are in [Appendix A](#).
- **Chapter 2:** where the ATLAS experiment is briefly introduced. First, a basic introduction to the LHC collider is provided and than a more detailed explanation of the ATLAS detector and its components is provided.
- **Chapter 3:** in this chapter the reconstruction of the fundamental particles detected by ATLAS is shown. The interested reconstructed objects are: electrons, muons,  $\tau$ -leptons, jets and missing transverse energy. An extra section about the overlap removal procedure is reported in the last section. Complements to this chapter can be found in [Appendix B](#).
- **Chapter 4:** in this final chapter all the fundamental steps of the analysis are pointed out. First, data and Monte Carlo (MC) samples are presented. Then, the event-selection and the discriminating variables, used for the unfolding, are shown. Finally, in the last sections, the unfolding procedure and the final results are reported. Complements to this chapter are located in [Appendix C](#).
- **Conclusions:** where discussions, conclusions and future outlooks of the analysis are discussed.

# Chapter 1

## Physical foundations

Particle physics is at the heart of our understanding of the laws on nature. It treats the fundamental constituents of our universe, the **particles**, and how they interact each other through **forces**. At the moment, the **Standard Model (SM)** (introduced in Section 1.1) is considered as one of the most powerful theories to describe the particles and their interactions. Despite some problems in the description of the theory, it seems to be able to provide a successful picture of a good part of the current experimental data.

Among all the elementary particles, there is one of them that behaves in a different manner with respect to the others: the **top quark** (described in Section 1.2). Due to its incredible properties, as the huge mass and the fact that it decays before hadronization, it is able to participate in many interesting processes, inaccessible otherwise.

One of them is the **quantum interference between singly  $t\bar{t}$  and doubly  $tWb$  resonant top quark production** in proton-proton ( $pp$ ) collisions (described in Section 1.3) [1].

### 1.1 The Standard Model of particle physics

As mentioned before, the SM is actually one of the most suitable theories to describe the nature and the particles. Recently, some issues have been discovered and confirmed<sup>1</sup>, questioning the validity of this model. Also other **Beyond the Standard Model (BSM)** theories like the **Super-Symmetry (SUSY)** got in trouble the infallibility of this theory, but, in spite of everything, it is currently one of the best choices to describe the microcosm. It is based on three gauge groups:

$$SU(3)_C \otimes SU(2)_L \otimes U(1)_Y \quad (1.1)$$

where first one is associated to the strong interaction and second and third one to electroweak one.

---

<sup>1</sup>Neutrino masses and flavor oscillations for example.

### 1.1.1 Particles and forces classification

Fundamental “matter” particles of the SM are called **fermions** and have semi-integer spin. They are:

$$\left. \begin{array}{l} \text{6 Leptons with Spin} = \frac{1}{2} \\ \text{6 Quarks with Spin} = \frac{1}{2} \end{array} \right\} \text{with also the corresponding anti-particles.}$$

Fermions are divided into three families, each of them composed by two leptons:

$$\begin{pmatrix} e \\ \nu_e \end{pmatrix}, \begin{pmatrix} \mu \\ \nu_\mu \end{pmatrix}, \begin{pmatrix} \tau \\ \nu_\tau \end{pmatrix} \quad (1.2)$$

and two quarks:

$$\begin{pmatrix} u \\ d \end{pmatrix}, \begin{pmatrix} c \\ s \end{pmatrix}, \begin{pmatrix} t \\ b \end{pmatrix} \quad (1.3)$$

Each of the six quarks has 3 possible colors, conventionally named: red, blue and green. Anti-fermions have opposite-sign quantum numbers with respect to fermions. The total number of fundamental constituents is therefore 24 fermions and 24 antifermions [2]. Ordinary matter is composed mainly by  $e$ ,  $u$  and  $d$ .

Particles are subject to forces, or more appropriately, to interactions, that explain the way in which matter is bound together. To allow for an action at distance that doesn't violate the relativity principles, it is necessary that forces be exchanged through a mediator, which needs to be a particle with integer spin, namely a vector **boson**: this is required by the **Quantum Field Theory (QFT)**. The four known fundamental interactions are: **gravitational interaction** (it doesn't enter the SM at the moment), **electromagnetic interaction (QED)**, **weak interaction (QFD)** and **strong interaction (QCD)**. In Table 1.1 the properties of each mediator are shown. Interactions

Interaction	Mediator	Symbol	Spin	Mass
Gravitational	Graviton (1)	G	2	0
Electromagnetic	Photon (1)	$\gamma$	1	0
Strong	Gluons (8)	g	1	0
Weak	W and Z (3)	$W^+, W^-, Z$	1	$\approx 100$

Table 1.1: Representation of the 4 fundamental forces mediators. The spin is reported in multiples of  $\hbar$ , the mass in  $\text{GeV}/c^2$ .

described by massless mediators have infinite range. This doesn't happen for weak interactions, because of the massive W and Z bosons, neither for the strong interaction, due to quark confinement.

Another fundamental scalar boson for the theory is the **Higgs boson** H, that through the **Brout-Englert-Higgs mechanism (BEH)** gives masses to the other particles.

Therefore, the total number of fundamental fermions and bosons in the theory is [3]:

$$48 \text{ (fermions)} + 12 \text{ (bosons)} + 1 \text{ (Higgs)} = 61 \quad (1.4)$$

In Figure 1.1 the SM fundamental particles with some of their properties are shown.

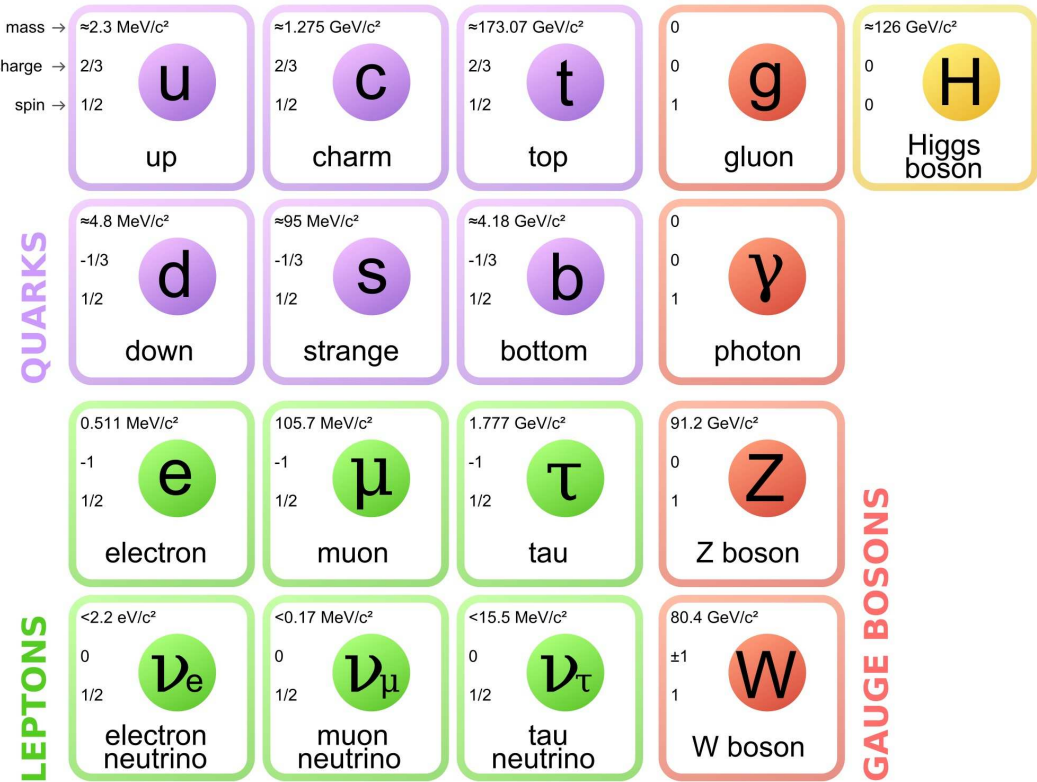


Figure 1.1: Fundamental particles of the SM with some of their properties.

### 1.1.2 Quantum Electrodynamics (QED)

The **electromagnetic (EM)** interaction is classically defined as the interaction between two electrically charged bodies that exchange a massless boson, called photon, as described by the Maxwell equations. At a fundamental level it is necessary a quantum field theory to describe this force. QED is the most suited theory so far. It is described by

the  $U(1)_{\text{EM}}$  gauge group. The interaction between two charged fermions is treated as the emission of a photon by one of them, followed by the absorption by the other one. See Figure 1.2a for an example of a possible EM interaction [4]. Since QED is an abelian

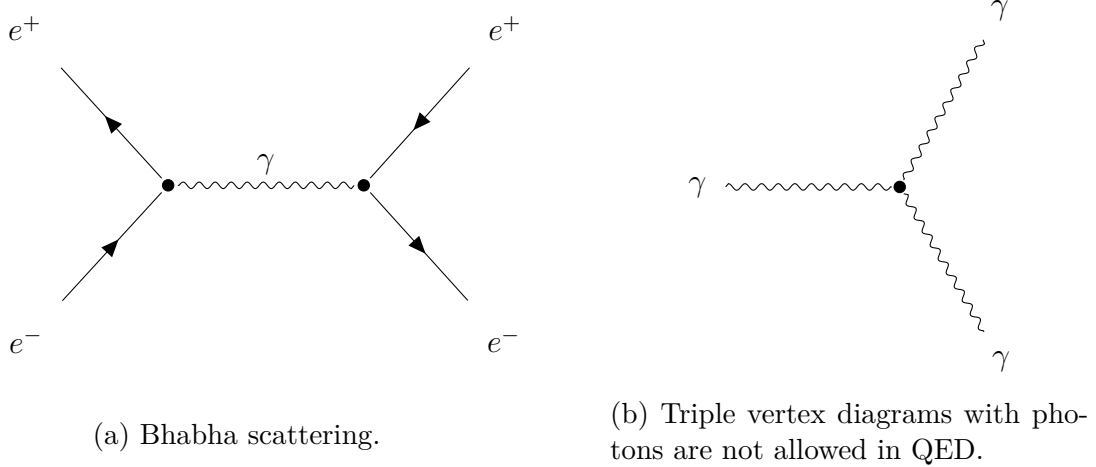


Figure 1.2: In (a): example of an EM interaction between an electron and a positron through the exchange of a photon. In (b): Triple vertex diagram with photons are not allowed in QED.

gauge theory, it is not possible to have vertices in absence of fermionic sources, neither with bosons self-interactions, as shown in Figure 1.2b. The two forces responsible to the EM interaction are the ones related to the **electric** and **magnetic fields**, defined in this way:

$$\vec{E} = -\vec{\nabla}\phi - \frac{\partial \vec{A}}{\partial t} \quad (1.5)$$

$$\vec{B} = \vec{\nabla} \times \vec{A} \quad (1.6)$$

where  $\phi$  is the scalar potential,  $\vec{A}$  is the vector potential and  $\vec{\nabla}$  is the *nabla* operator. In general, the electromagnetic four-potential is defined as:

$$A^\mu = (\phi, \vec{A}). \quad (1.7)$$

Each interaction is now represented by a **density lagrangian**, that in this case is:

$$\mathcal{L}_{EM} = -\frac{1}{4}F_{\mu\nu}F^{\mu\nu} - J_\mu A^\mu + \frac{1}{2}m^2 A^\mu A_\mu \quad (1.8)$$

where  $F_{\mu\nu}$  is the EM tensor and  $J_\mu$  is the current-density. The first term of the Eq. 1.8 is called *kinetic term*, the second one is called *interaction term* ( $\mathcal{L}_{int}$ ). If the field was massive, with mass  $m$ , the third term would represent the *mass term*.

The total QED lagrangian is obtained requiring its invariance under local gauge transformations. In fact, free fermions are described by the *Dirac lagrangian*:

$$\mathcal{L}_{free} = \bar{\psi}(x)(i\gamma^\mu\partial_\mu - m)\psi(x) \quad (1.9)$$

where  $\psi$  is a 4-component *Dirac spinor*,  $\gamma^\mu$  are the *Dirac matrices* (see Appendix A.1),  $\bar{\psi} = \psi^\dagger(x)\gamma^0$ . If now one introduces the covariant derivative:

$$\mathcal{D}_\mu = \partial_\mu + iqA_\mu(x) \quad (1.10)$$

Eq. 1.9 results invariant under local gauge transformations, and the new lagriangian becomes:

$$\mathcal{L} = \mathcal{L}_{free} - qA_\mu\bar{\psi}\gamma^\mu\psi \quad (1.11)$$

with  $J^\mu = \bar{\psi}\gamma^\mu\psi$ . This is invariant under local gauge transformations:

$$\psi(x) \rightarrow e^{iq\alpha(x)}\psi(x) \quad (1.12)$$

$$A_\mu(x) \rightarrow A_\mu(x) - \partial_\mu\alpha(x) \quad (1.13)$$

where  $\alpha(x)$  is a generic function, parameter of the transformation. To obtain the final QED lagrangian it is necessary to also include the kinetic term of the Eq. 1.8 that describes the propagation of the photon associated to the field:

$$\mathcal{L}_{QED} = \mathcal{L}_{free} - qA_\mu\bar{\psi}\gamma^\mu\psi - \frac{1}{4}F_{\mu\nu}F^{\mu\nu} \quad (1.14)$$

where mass term of the Eq. 1.8 has been omitted since it would violate the local gauge invariance and the lagrangian correctly describes a non-massive photon [5].

From the vertex of an EM interaction it is possible to extract an adimensional coupling, called **fine structure constant** which its common value is:

$$\alpha_{EM} \simeq \frac{1}{137.1} \quad (1.15)$$

even if it is not properly a constant, because it is a running coupling and varies with the energy scale.

### 1.1.3 Quantum Flavordynamics (QFD)

The QFD, or simply **weak interaction**, is different with respect to QED. The interaction is mediated by three charged bosons:  $W^\pm$  for charged current interaction (CC), and  $Z$  for neutral current interaction (NC).

A very particular property of this kind of force is its relation with the **parity** quantum number: the weak interaction is the only one that violates simultaneously parity and  $C$ -parity (CP)<sup>2</sup>. Parity is represented as the  $\gamma^0$  Dirac matrix operator:

$$\hat{P} = \gamma^0 = \begin{bmatrix} 1 & 0 & 0 & 0 \\ 0 & 1 & 0 & 0 \\ 0 & 0 & -1 & 0 \\ 0 & 0 & 0 & -1 \end{bmatrix} \quad (1.16)$$

Parity violation was discovered by Madame Wu in 1957, studying the nuclear  $\beta$ -decay of  $^{60}\text{Co}$ . From this observation, the weak interaction vertex required to have a different form with respect to the other interactions such as QED or QCD. The requirement of Lorentz invariance of the matrix element severely restricts the possible forms of the interaction.

It was demonstrated that the most general form for the interaction came only from the linear combination of 2 *bilinear covariants* giving rise to the **Axial-Vector (V-A)** current.

The most representative Hamiltonian of the QFD is the one associated with the  $\beta$ -decay of the neutron:

$$H_{V-A} = \frac{G_F}{\sqrt{2}} [\bar{\psi}_p \gamma^\mu (1 - \gamma^5) \psi_n] [\bar{\psi}_e \gamma^\mu (1 - \gamma^5) \psi_\nu] \quad (1.17)$$

where  $\gamma^\mu$  is the vector operator and  $\gamma^\mu \gamma^5$  is the axial-vector one. See Figure 1.3 for a graphical representation of the Feynman diagram of the neutron  $\beta$ -decay.  $G_F$  is the

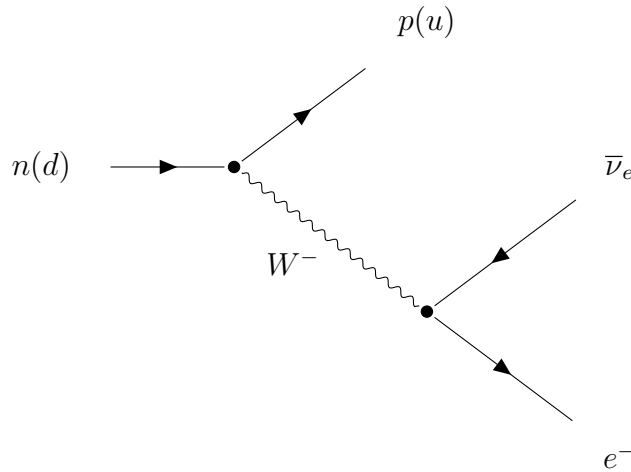


Figure 1.3: Feynman representation of the  $\beta$ -decay of the neutron:  $n \rightarrow p + e^- + \bar{\nu}_e$ .

---

<sup>2</sup>C is the charge conjugation operator.

*Fermi constant*, embedding the “strength” of the weak interaction:

$$\frac{G_F}{\sqrt{2}} = \frac{g_W^2}{8m_W^2} \quad (1.18)$$

This interaction is called “weak” because of the large mass ( $m_W \simeq 80$  GeV) at the denominator of the Eq. 1.18. The  $g_W$  represents the coupling constant and is useful to determine the fine structure constant of the QFD:

$$\alpha_W = \frac{g_W^2}{4\pi} \approx \frac{1}{30} > \alpha_{EM} \quad (1.19)$$

and also in this case the constant varies with the energy. Each vertex is expressed as:

$$-\frac{ig_W}{\sqrt{2}} \frac{1}{2} \gamma^\mu (1 - \gamma^5) \quad (1.20)$$

Since QFD is a non-Abelian gauge theory, vertices like the ones shown in Figure 1.4 are allowed.

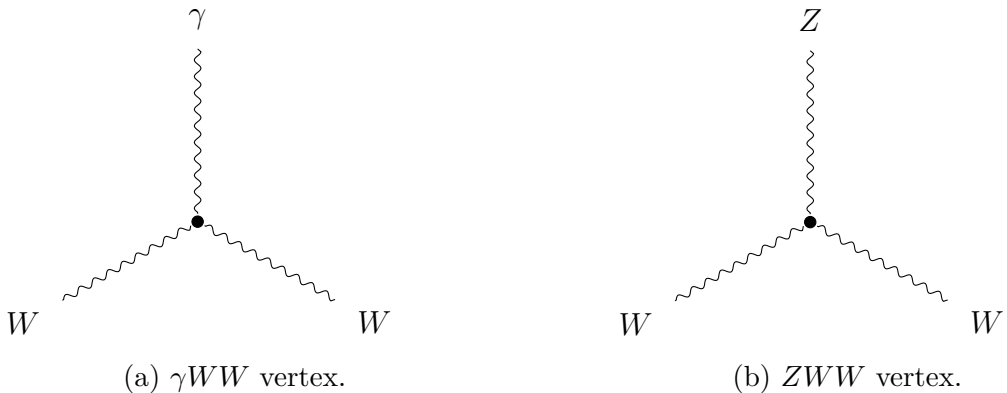


Figure 1.4: Allowed vertices in QFD theory.

#### 1.1.4 Quantum Chromodynamics (QCD)

QCD, also called **strong interaction**, is the last of the three fundamental interactions mentioned in the introduction. This interaction involves only quarks and is related to the  $SU(3)_C$  gauge group, where the label C stands for *color*. The energy scale of this force varies with the energy and the number of considered quark flavors, but usually is used the value 250 MeV that is the necessary energy to confine two quarks in a pion.

The property that distinguishes quarks from leptons is the **color** quantum number, so it is natural to construct a theory of the strong interactions among quarks based upon a local color gauge symmetry.

Interactions among quarks are mediated by **gluons**, that are massless vector bosons and are 8 in total.

The six quarks presented in Section 1.1.1 (see figure 1.1) are color triplets.

To construct a theory (and a lagrangian) of the strong interactions we have to start from the description of a free quark lagrangian. It can be described by the Eq. 1.9. The dirac spinor is composed by three different components associated to the three colors:

$$\psi(x) = (\psi_{red}, \psi_{green}, \psi_{blue}). \quad (1.21)$$

Let's now consider the covariant derivative, defined in Eq. 1.10, with a new field  $B_\mu$ , and the strong coupling constant  $g_s$ :

$$\mathcal{D}_\mu = \partial_\mu + ig_s B_\mu \quad (1.22)$$

where  $B_\mu$  is a  $3 \times 3$  matrix in color space, that depends on the eight color gauge fields  $b_\mu^l$  and the generators  $\lambda^l/2$  of the  $SU(3)_C$  gauge group:

$$B_\mu = \frac{1}{2} \vec{\lambda} \cdot \vec{b}_\mu = \frac{1}{2} \lambda^l b_\mu^l \quad (1.23)$$

where  $\lambda$  are the Gell-Mann  $\lambda$ -matrices. Adding also a kinetic term to the lagrangian, determined by the  $G_{\mu\nu}$  gluon field-strength tensor, the new lagrangian becomes:

$$\mathcal{L}_{QCD} = \bar{\psi}(x)(i\gamma^\mu \mathcal{D}_\mu - m)\psi(x) - \frac{1}{2}\text{tr}(G_{\mu\nu}G^{\mu\nu}) \quad (1.24)$$

As for the QFD, QCD is a non-Abelian gauge theory and 3 or 4 gluon vertices are allowed in the theory (see Figure 1.5). The strong coupling constant  $\alpha_s$  varies with

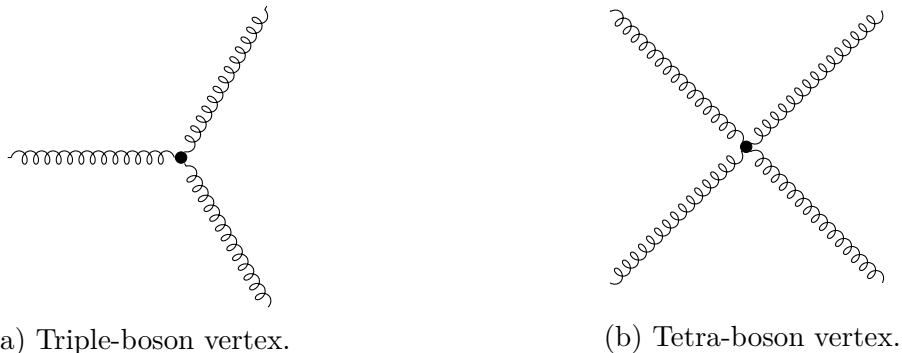


Figure 1.5: Allowed vertices in the QCD theory.

the energy scale (it's a running coupling): for energies of  $\approx 100$  GeV,  $\alpha_s \approx 0.1$ , this is called *asymptotic freedom* regime in which perturbative approach is possible; instead, for smaller energies ( $\approx 1$  GeV),  $\alpha_s \approx 1$  and this is called *confinement* regime. An example of a possible strong interaction is the one shown in Figure 1.6.

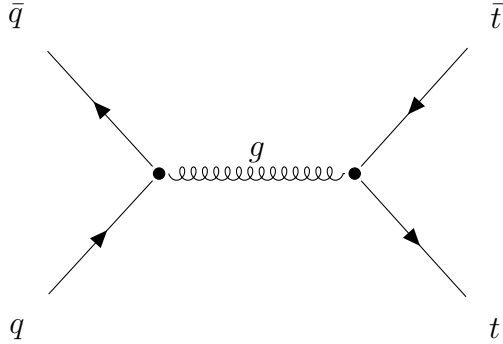


Figure 1.6: Production of  $t\bar{t}$  via  $q\bar{q}$  annihilation.

### 1.1.5 Electroweak theory

In the SM all fermions are decomposed into *left-handed* and *right-handed chiral* states. In general each fermion family can be written as:

$$\begin{bmatrix} \nu_l & q_u \\ l^- & q_d \end{bmatrix} = \begin{pmatrix} \nu_l \\ l^- \end{pmatrix}_L, \begin{pmatrix} q_u \\ q_d \end{pmatrix}_L, l_R^-, q_{uR}, q_{dR} \quad (1.25)$$

where  $\nu_l$  is the generic neutrino associated to the charged lepton  $l^-$  and  $q_u$  and  $q_d$  are the up-type and down-type quarks. The left-handed fields are  $SU(2)_L$  doublets, while their right-handed partners transform as  $SU(2)$  singlets [6].

To describe a unified theory of electromagnetic and weak interactions (this forces are unified at  $\simeq 246$  GeV) we would like to have massive gauge bosons  $W^\pm$  and  $Z$  and massless QED boson  $\gamma$ . The simplest group to describe this interaction is:

$$G = SU(2)_L \otimes U(1)_Y \quad (1.26)$$

where  $Y$  is the *hypercharge*, defined as:

$$Q = I_3 + \frac{Y}{2} \quad (1.27)$$

with  $Q$  electromagnetic charge and  $I_3$  third component of the weak isospin.

Let's start by considering a lagrangian as in QED and QCD:

$$\mathcal{L}_0 = \sum_{j=1}^3 i\bar{\psi}_j(x)\gamma^\mu\partial_\mu\psi_j(x) \quad (1.28)$$

where  $\psi_1(x)$  is the up-down spinor doublet of the quark or lepton sector,  $\psi_2(x)$  is the right-handed spinor singlet of the up-component and  $\psi_3(x)$  is the right-handed spinor

singlet of the down-component. This lagrangian is invariant under global gauge transformations in flavor space. If we replace fermion derivatives with covariant derivatives we get local gauge invariance. So, the new lagrangian with  $\partial_\mu \rightarrow \mathcal{D}_\mu$  has the useful properties to start the description of the theory. First, it's necessary to build a kinetic term, starting with the introduction of two field strength tensors:

$$B_{\mu\nu} = \partial_\mu B_\nu - \partial_\nu B_\mu \quad (1.29)$$

$$\widetilde{W}_{\mu\nu} = \partial_\mu W_\nu^i - \partial_\nu W_\mu^i - g\epsilon^{ijk}W_\mu^j W_\nu^k \quad (1.30)$$

where  $B_\mu$  is the gauge field of QED,  $\widetilde{W}_\mu$  are the gauge fields of QFD,  $g$  is the coupling constant of the  $SU(2)_L$  group and  $\epsilon^{ijk}$  is the Levi-Cita tensor. Both fields of Eq. 1.29 and 1.30 are invariant under gauge transformations. Therefore, the kinetic term becomes:

$$\mathcal{L}_{kin} = -\frac{1}{4}B_{\mu\nu}B^{\mu\nu} - \frac{1}{2}tr\left[\widetilde{W}_{\mu\nu}\widetilde{W}^{\mu\nu}\right] = -\frac{1}{4}B_{\mu\nu}B^{\mu\nu} - \frac{1}{4}W_{\mu\nu}^i W_i^{\mu\nu} \quad (1.31)$$

The gauge symmetry forbids a mass term for the gauge bosons and also fermionic masses are not allowed since they would link the left- and right-handed fields, which have different transformation properties and therefore would provide an explicit breaking of the symmetry. Now this lagrangian contains only massless fields and generates also cubic and quadratic terms that have to be taken into account.

The lagrangian of Eq. 1.28 contains interactions of fermion fields with gauge bosons, so they describe possible charged-current (CC) interactions with the boson fields  $W_\mu$  and its complex-conjugate  $W_\mu^\dagger$  for a single family of quarks and leptons:

$$\mathcal{L}_{CC} = -\frac{g}{2\sqrt{2}}\{W_{mu}^\dagger[\bar{u}\gamma^\mu(1-\gamma_5)d + \bar{\nu}_e\gamma^\mu(1-\gamma_5)e] + h.c.\} \quad (1.32)$$

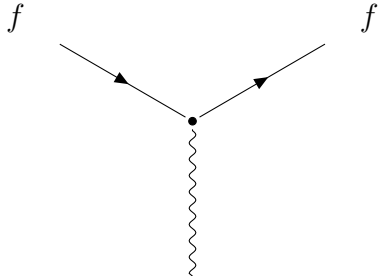
where *h.c.* are hermitian conjugates terms. However also neutral current (NC) interactions based on the  $W_\mu^3$  and  $B_\mu$  fields are allowed, and a NC term of the lagrangian is necessary:

$$\mathcal{L}_{NC} = \mathcal{L}_{QED} - \frac{e}{2\sin\theta_W\cos\theta_W}J_Z^\mu Z_\mu \quad (1.33)$$

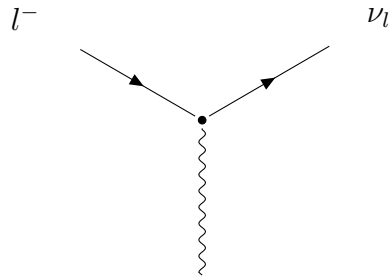
where  $\mathcal{L}_{QED}$  is the lagrangian of QED,  $e = g\sin\theta_W$ ,  $\theta_W$  is the *Weinberg angle* that mixes  $W_\mu^3$  and  $B_\mu$  with the physical fields  $Z_\mu$  and  $A_\mu$  and  $J_Z^\mu$  is the neutral fermionic current. See Figure 1.7 for some examples of CC and NC electroweak processes.

The problem of this lagrangian is that it does not contain mass terms for the fermions nor for the vector bosons. The issue of fermions and bosons masses can be solved with the introduction of the **spontaneous symmetry breaking (SSB)** and the BEH mechanism (mentioned in Section 1.1.1) in the case of a lagrangian with local gauge symmetry. After the application of this theory, the gauge bosons of the weak interaction and the fermions became massive and a new massive scalar field called *Higgs boson* is introduced. Therefore, the new final masses of the weak bosons are now:

$$M_Z \simeq 91 \text{ GeV}, M_W \simeq 80 \text{ GeV} \quad (1.34)$$



(a) NC interaction vertex.



(b) CC interaction vertex.

Figure 1.7: Examples of CC and NC allowed electroweak processes. In (a): NC vertex of a generic fermion  $f$ . In (b): CC vertex of a generic lepton  $l^-$  and the corresponding neutrino  $\nu_l$ .

## 1.2 Top quark physics

The top quark is one of the most particular elementary particle observed so far. As mentioned in the introduction of Section 1, it has very singular properties that let him to behave in a completely different manner in respect to the lightest elementary components. In this section will be introduced a brief overview on the top quark physics at the LHC, explaining its properties and its importance in current studies.

### 1.2.1 The top particle

Let us firstly contextualize the most significant dates for the discovery of the top quark  $t$ :

- 1964: quark model proposed by Gell-Mann and Zweig.
- 1970: *GIM Mechanism*  $\Rightarrow$  introduction of the fourth quark, the *charm*.
- 1975: discovery of the  $\tau$   $\Rightarrow$  3 generations of leptons.
- 1977: discovery of the  $\Upsilon$  and the introduction of the fifth quark, the *bottom*.
- 1984:  $t$  not observed at  $SppS$  accelerator  $\Rightarrow$  limit on the  $t$  mass:  $m_t > 44 \text{ GeV}$ .
- 1990:  $t$  not observed at LEP collider.

The discovery was announced at Fermilab on March 3, 1995, with a luminosity  $L \simeq 60 \text{ fb}^{-1}$ , yielding very few events, but with  $5\sigma$  discovery significance<sup>3</sup>.

---

<sup>3</sup>Corresponding to a probability of  $10^{-6}$ .

From the studies and further measurements followed along the years, at present we know that:

- It is a point-like particle.
- It is massive.
- It has spin  $\frac{1}{2}$ .
- It is produced both strongly and weakly.
- It decays immediately before hadronizing.
- It is the particle more intensively coupled with the Higgs boson, through the *Yukawa coupling*.

With a mass of  $\simeq 173$  GeV, above the  $Wb$  threshold, the decay width of the  $t$  is expected to be dominated by the two-body decay channel:

$$t \rightarrow Wb \quad (1.35)$$

Neglecting terms of order  $m_b^2/m_t^2$ ,  $\alpha_s^2$  and those of the order  $(\alpha_s/\pi)m_W^2/m_t^2$  in the decay amplitude, the width predicted through the SM theory is [7]:

$$\Gamma_t = \frac{G_F m_t^2}{8\pi\sqrt{2}} \left(1 - \frac{m_W^2}{m_t^2}\right)^2 \left(1 + 2\frac{m_W^2}{m_t^2}\right) \left[1 - \frac{2\alpha_s}{3\pi} \left(\frac{2\pi^2}{3} - \frac{5}{2}\right)\right]. \quad (1.36)$$

We can see that: the  $G_F$  constant contains the largest part of the one-loop electroweak radiative corrections, providing an expression accurate to better than 2% and this width increase with the mass of the top. From the 1.36 it is possible to calculate the top lifetime, that is:

$$\tau_t \simeq 0.5 \times 10^{-24} \text{s} \quad (1.37)$$

and due to this very short lifetime, it's expected to decay before top-flavoured hadrons or  $t\bar{t}$ -quarkonium bound states can form. Also other QCD corrections can be applied to the 1.36, reducing the theoretical accuracy to 1%. Other  $Ws$  or  $Wd$  decays are suppressed because of the values of the *CKM matrix*.

The  $W$  boson decays as well and its possible decay channels are:

$$W \rightarrow l\nu_l, \quad W \rightarrow qq' \rightarrow jj \quad (1.38)$$

where  $l$  is a lepton,  $\nu_l$  is the corresponding neutrino,  $q$  and  $q'$  are two different quarks and  $j$  are jets. See Figure 1.8 for a schematic view of an example of a top-quark decay Feynman diagram.

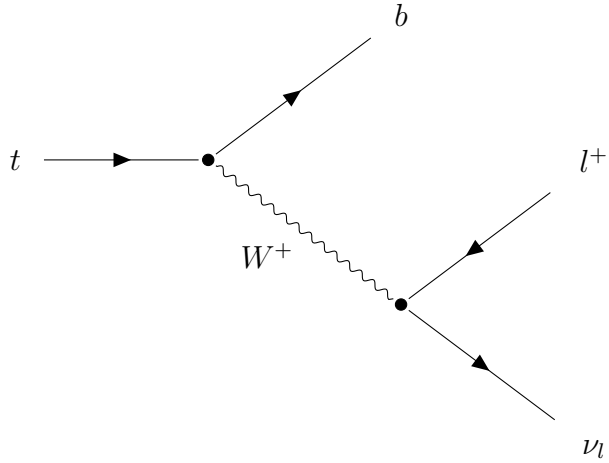


Figure 1.8: Example of decay channel of  $t$  quark into  $W^+$  and  $b$  with subsequent decay:  $W^+ \rightarrow l^+ \nu_l$ .

### 1.2.2 Fundamental properties of top quark

Some of the most fundamental Top quark properties are:

- **Mass:** the mass of the top quark is larger than that of any other existing quark. Its value is known with a relative precision (1.7%) better than any other quark (see Figure 1.9). According to the adopted experimental technique, the mass value should be taken as representing the Top *pole-mass*, that is defined as the real part of the pole in the top quark propagator:

$$\sqrt{p^2} = m_t^{pole} - \frac{i}{2}\Gamma \quad (1.39)$$

where  $p$  is the 4-momentum and  $\Gamma$  is the decay rate [8]. This pole-mass is defined up to an intrinsic ambiguity of the order of  $\Lambda_{QCD} \approx 200$  MeV. Masses of top,  $W$  and  $H$  particles are linked by a relation (see radiative correction formula 1.46 later), therefore, better precision in the estimation of the top mass is given also by better precision in the measurement of  $W$  and  $H$  masses (see Figure 1.10). World combination of ATLAS, CMS, CDF and D0 mass measurements is [10]:

$$m_t = 173.34 \pm 0.98 \text{ GeV} \quad (1.40)$$

- **Electric charge:** the electric charge of the top quark is easily accessible in  $e^+e^-$  collisions, by the measurement of:

$$R = \frac{\sigma(e^+e^- \rightarrow \text{hadrons})}{\sigma(e^+e^- \rightarrow \mu^+\mu^-)} \quad (1.41)$$

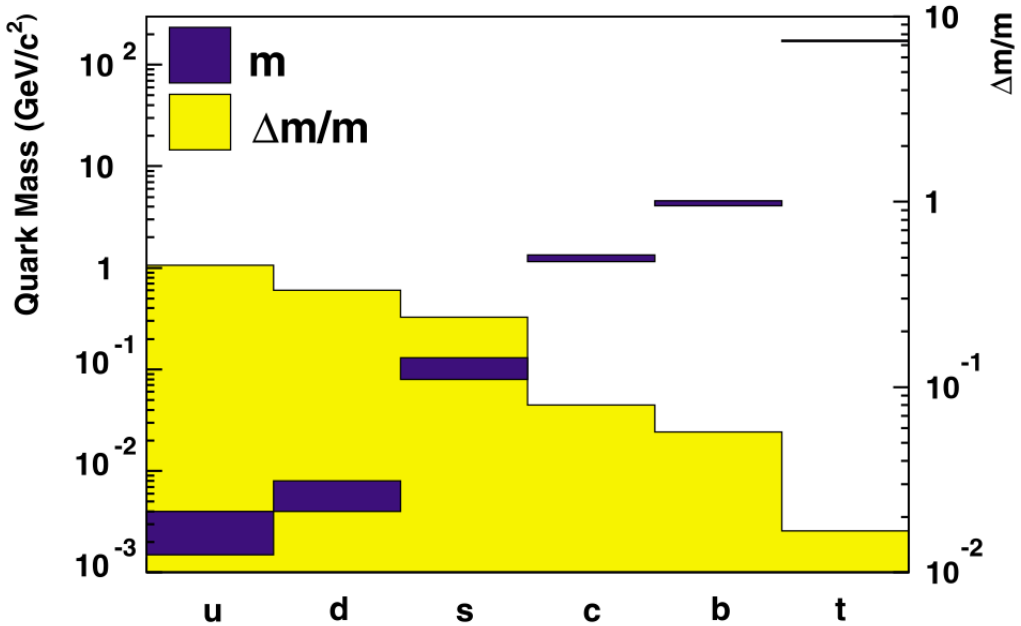


Figure 1.9: Quark masses  $m$  and their absolute and relative uncertainties  $\Delta m/m$ , indicated by vertical size of the error bands.

through the top quark production threshold. At the LHC, gluon fusion dominates and the  $t\bar{t}\gamma$  cross-section scales approximately with  $q_{top}^2$ . Due to the fact that it is an up-type quark, the electric charge of the top quark is  $+2/3$ .

- **Helicity of the  $W$  boson in top quark decay:** the SM implies that the Top quark has the same V-A charged-current weak interaction as all the other fermions (see Section 1.1.3):

$$-i \frac{g}{\sqrt{2}} V_{tb} \gamma^\mu \frac{1}{2} (1 - \gamma_5) \quad (1.42)$$

where  $V_{tb}$  is the element of the CKM matrix. This implies that the  $W$  boson of the  $t$  decay cannot have right-handed (RH) positive helicity (see Figure 1.11). If the  $W$  boson were RH, then the component of total angular momentum along the decay axis would be  $+3/2$ , but the initial  $t$  quark has spin angular momentum  $\pm 1/2$  along this axis, so this decay is forbidden by conservation of angular momentum. However some searches are trying to find a RH  $W$  in the top quark decay. The  $t$  prefers to decay into left-handed (LH)  $W$  boson with a branching ratio of  $B(t \rightarrow Wb) \simeq 0.7$ .

- **Spin correlation in strong  $t\bar{t}$  production:** on average, the top quark decays before there is time for its spin to be depolarized in the strong interaction. The top quark polarization is directly observable via the angular distribution of its

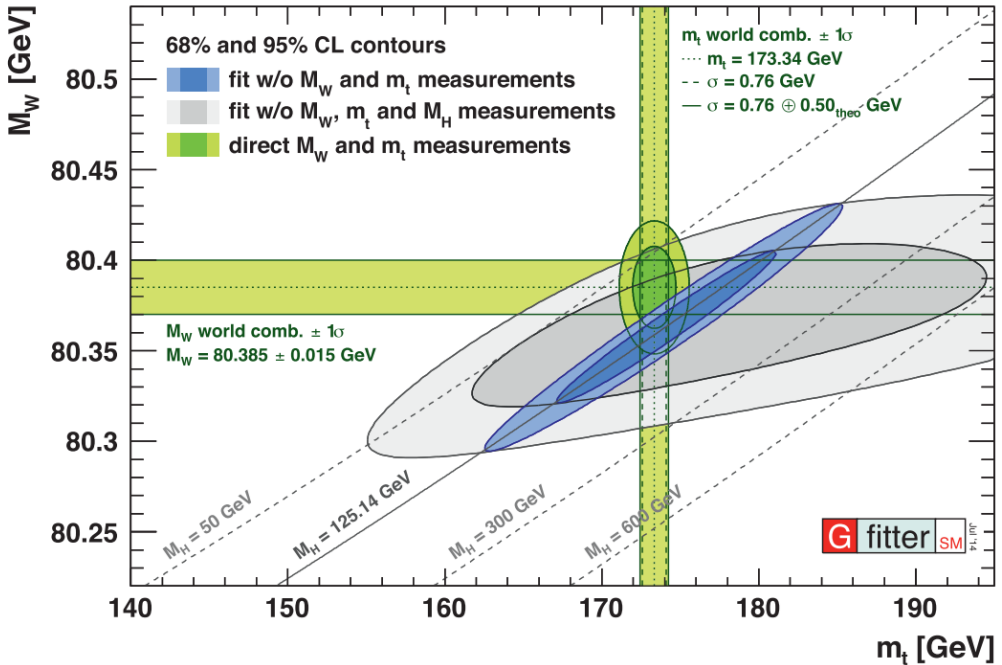


Figure 1.10: Plot of  $m_W$  vs  $m_t$ . In figure the 68% and 95% CL contours for the indirect determination of  $m_t$  and  $m_W$  from global SM fits to EW precision data are shown [9].

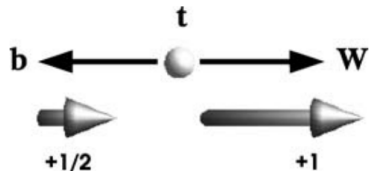


Figure 1.11: Illustration of the impossibility of the  $W$  boson from the decay of the  $t$  to be right-handed (referred to helicity).

decay products. So, it is possible to measure observables that are sensitive to the top quark spin. Spin of the  $t$  and  $\bar{t}$  are correlated in  $t\bar{t}$  production processes. Another interesting motivation for the study of this property is, for example, the detection of the entanglement between the spins of top-antitop quark pairs, that represents the first proposal of entanglement detection in a pair of quarks, and also the entanglement observation at the highest energy scale so far. This entanglement can be observed by direct measurement of the angular separation between the leptons arising from the decay of the top-antitop pair.

- **Asymmetry in strong  $t\bar{t}$  production:** it is an interesting aspect of the strong

production of top quark pairs, for which there is an asymmetry in the rapidity distribution of the  $t$  and  $\bar{t}$  quarks. This effect is evident at NLO.

- **Rare decays:** the top quark can also undergo some very rare decays that could be interesting to study. For example, some of them are the CKM-suppressed decays:

$$B(t \rightarrow W s) \approx 0.1\% \quad (1.43)$$

$$B(t \rightarrow W d) \approx 0.01\% \quad (1.44)$$

they are difficult to identify in the decay processes.

- **Yukawa coupling:** Yukawa coupling of the Higgs boson with the top quark is defined as:

$$y_t = \frac{\sqrt{2}m_t}{v} \quad (1.45)$$

where  $v \approx 246$  GeV is the vacuum expectation energy. The value of this coupling is very close to unity. This value leads to numerous speculations related to new physics that can be accessed with the study of the top quark. At LHC it's measured in  $t\bar{t}H$  processes.

### 1.2.3 Impacts of top quark in SM and BSM physics

Precise measurements of top quark parameters are fundamental to constrain SM physics and BSM processes. First of all, the **mass**  $m_t$  is one of the most interesting parameters. The  $m_t$  plays a central role in the SM. Indeed, the top quark participate to radiative corrections of higher order of the bosonic propagator and for example it modifies the mass of the  $W$  (see Figure 1.12). Theoretical calculations of the  $m_W$  are:

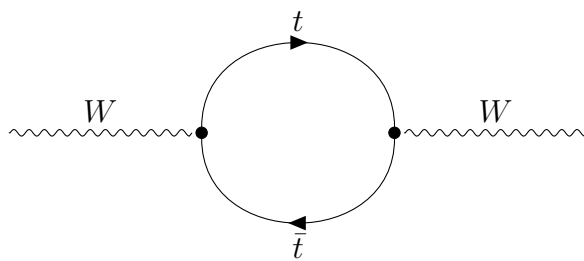


Figure 1.12: Radiative corrections from the top quark of higher order of the bosonic propagator of  $W$ .

$$m_W^2 = \frac{\pi \alpha_{EM}}{\sqrt{2}G_F \sin^2 \theta_W} \frac{1}{1 - \Delta r} \quad (1.46)$$

where  $\alpha_{EM}$ ,  $G_F$  and  $\theta_W$  have been already defined in previous sections and  $\Delta r$  is defined as:

$$\Delta r \simeq \Delta\rho_0 - \frac{\Delta\rho}{\tan^2\theta_W} \approx 3\% \quad (1.47)$$

where the first term is the running of the strong coupling constant  $\alpha_s$  and the second one represents the one-loop corrections [11]. Then:

$$\Delta\rho = \frac{3G_F m_t^2}{8\sqrt{2}\pi^2} \quad (1.48)$$

As mentioned in Section 1.2.2 (Figure 1.10), the top quark mass depends on the coupling to the Higgs boson through loops with  $H$ , therefore, a combined measurement of  $m_W$  and  $m_t$  can constrain the possible values of  $m_H$ :

$$\Delta m_W \propto \Delta m_t^2 \quad (1.49)$$

$$\Delta m_W \propto \log \Delta m_H^2 \quad (1.50)$$

or, having discovered the Higgs boson, test the global consistency of the SM. Finally, measuring accurately  $m_H$  vs  $m_t$  provides a test of the stability of the vacuum state of the SM and the ultimate fate of our universe. Present estimates suggest that we're in a region of meta-stability, with important cosmological limitations, but in a time far larger than the present age of the universe. See Figure 1.13 for a graphical representation of this problem [12]. Another fundamental quantity to measure is the **cross-section**  $\sigma$

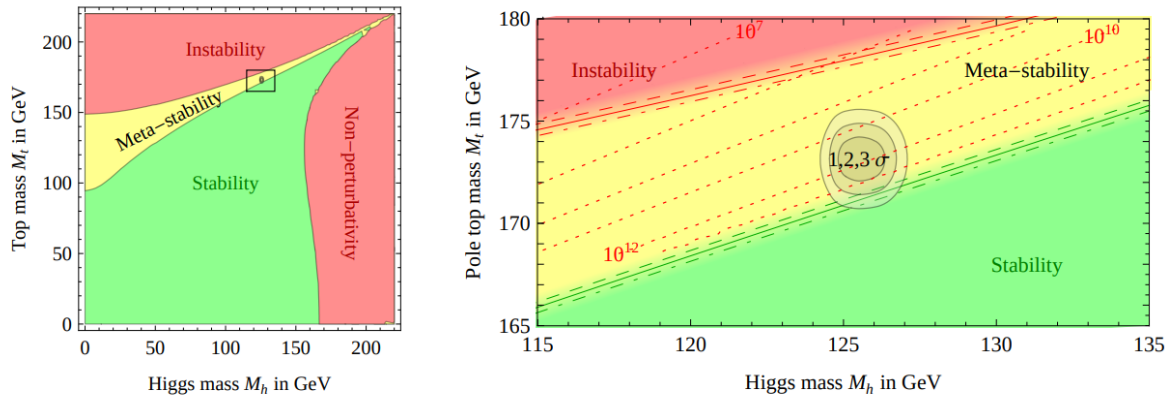


Figure 1.13: Regions of absolute stability, meta-stability and instability of the SM vacuum in the  $m_t$  vs  $m_h$  (Higgs boson mass) plane. The gray areas denote the allowed region at 1, 2, and 3  $\sigma$ .

of the production processes of the top quark or of its decays. For example, the cross

section of  $t\bar{t}$  production process at the LHC, that will be discussed in Section 1.3.1 and Appendix A.2, is given by:

$$\sigma(pp \rightarrow t\bar{t}) = \sum_{i,j} \int d\vec{x}_i f_i(\vec{x}_i, \mu^2) \int d\vec{x}_j f_j(\vec{x}_j, \mu^2) \hat{\sigma}_{ij}(\hat{s}, \mu^2, m_t) \quad (1.51)$$

where the sum is extended over partons  $i$  and  $j$ ,  $f$  are the parton density functions (PDFs) of light quarks and gluons,  $\vec{x}$  is the momentum fractions,  $\hat{s}$  is the center-of-mass energy of partons and  $\hat{\sigma}$  is the partonic cross-section (see Figure 1.14). The cross-section

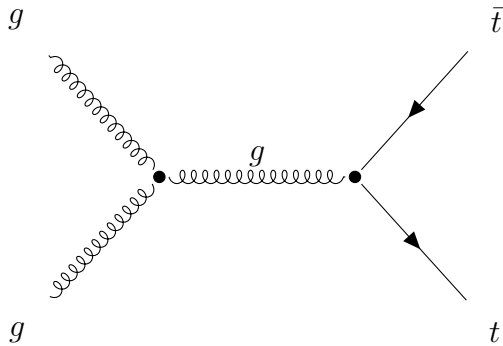


Figure 1.14: Production of  $t\bar{t}$  pair at the LHC, through gluon-gluon fusion.

depends on the mass of the top and on the factorization scale  $\mu$ , because calculations are carried at some finite order. Measurements of a cross-section are fundamental to extract useful constraints to some parameters. For example, in this case, a constraint on the PDFs is provided and also a determination of  $\alpha_s$  and  $m_t$ ; but also a characterization of the soft radiation, in production and decay, and a constrain on parton shower and hadronization models is provided [13].

To better compare with theoretical models, it is important to measure also **differential cross-sections**. Conventions used are:

- **Particle level:** in which one refers to quantities measurable directly in the detector.
- **Parton level:** which refers to the true kinematics quantities of the produced top quarks, which must be extrapolated to the full phase space.

These cross sections are usually measured as a function of one or more variables. Deviation from the model prediction could signal the presence of BSM physics.

The top quark processes are also fundamental to measure three parameters of the CKM matrix, namely  $|V_{td}|$ ,  $|V_{ts}|$  and  $|V_{tb}|$ .

## 1.3 The quantum interference between $t\bar{t}$ and $tW$ production processes

An interesting process involving the top quark is the quantum interference between singly and doubly resonant top quark production. At the LHC, the top quark is produced mainly through gluon-gluon fusion, giving  $t\bar{t}$  pair (see Figure 1.14); but there is also the possibility to be produced singly, with an associated  $W$  boson and a  $b$  quark. The latter is a rarer process than the previous one. It happens that at NLO QCD corrections the two previous mentioned processes interfere and this interference may provide important contributes to other SM and BSM physics processes. In particular, several BSM searches have developed selections that are enriched in  $Wt$  events in the interference region (see Section 1.3.4). So, the spread in model prediction for this process is large and this results in large systematic uncertainties [14].

Better knowledge on the interference would be also useful to discriminate triple Higgs boson vertices like  $t\bar{t}H$  and  $WtH$  or  $t\bar{t}\gamma$  and  $tW\gamma$ . The latter is important because  $t\bar{t}\gamma$  probes  $t\gamma$  coupling and is sensitive to anomalous dipole-moment and *Effective Field Theory (EFT)* operators.

To take into account this interference process and avoid double counting when simulating  $t\bar{t}$  and  $Wt$  samples, there are in general two ways: the first one consists of the study of  $Wt$  at NLO and  $t\bar{t}$  at LO with *removal* techniques (DR, DR2 and DS, Section 1.3.3), the second one consists in the direct study/measurement of the  $WbWb$  final state.

### 1.3.1 Top pair production process: $t\bar{t}$

The Top quark is currently studied at CERN by the two experiments ATLAS and CMS. At LHC, the dominant mechanism for the production of a top quark through a pair of  $t\bar{t}$  is the gluon-gluon fusion. The relative contributions for the top production at LHC are:

$$B(q\bar{q} \rightarrow t\bar{t}) < 20\% \quad (1.52)$$

$$B(gg \rightarrow t\bar{t}) > 80\% \quad (1.53)$$

The first process was dominant at Tevatron. At LO the diagram for the pair-production is the one shown in Figure 1.14, but also other diagrams (see Figure 1.15) can contribute. If we consider the ratio between the mass of the top  $m_t$  and the energy of the proton  $E_p$  in the collision:

$$x_{min} = \frac{m_t}{E_p} \simeq 0.043 \quad (1.54)$$

with  $E_p \approx 6500$  GeV,  $x_{min}$  is quite small and therefore gluon PDF dominates (see Figure 1.16). The production rate for  $\sqrt{s} = 13$  TeV and  $\mathcal{L} \simeq 1 \times 10^{33} \text{ cm}^{-2}\text{s}^{-1}$  is about

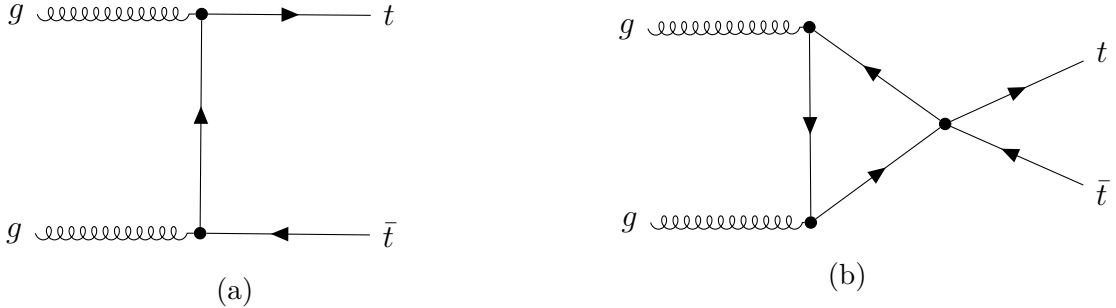


Figure 1.15: Alternative diagrams for the  $t\bar{t}$  production process through gluon-gluon fusion at the LHC.

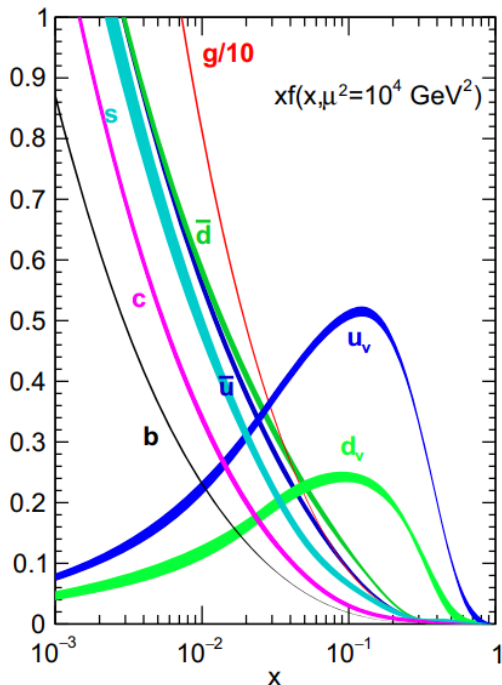


Figure 1.16: The NNPDF3.1 NNLO PDFs, evaluated at  $\mu^2 = 10^4 \text{ GeV}^2$  [15].

1 Hz, giving a production cross-section of  $\sigma_{tt}^{13 \text{ TeV}} \simeq 8 \times 10^{-34} \text{ cm}^2$ . All this means the production of 2 million  $t\bar{t}$  events per month, when LHC is on.

The  $t\bar{t}$  production is described by perturbative QCD; in this approach, a hard scattering process between two hadrons is the result of an interaction between the quarks and the gluons which are the constituents of the incoming hadrons. The incoming proton provides broad band beams of partons carrying fractions  $x$  of the momentum of the parent hadron. Perturbative expansions of the calculations related to the partonic cross

section (see Eq. 1.51) are shown in Appendix A.2 and are fundamental to get more sensitivity on important parameters, when comparing data with theoretical models. In higher order calculations, infinities such as ultraviolet divergences appear. They are removed by renormalization procedure.

To produce a top-quark pair at rest, it is required a minimum amount of center-of-mass energy:

$$\hat{s} \geq 4m_t^2 \quad (1.55)$$

and therefore:

$$x_i x_j = \frac{\hat{s}}{s} > \frac{4m_t^2}{s} \quad (1.56)$$

Setting  $x_i = x_j = x$  one gets the result shown in Eq. 1.54.

An accurate calculation of this cross-section is a necessary ingredient for the measurement of the  $|V_{tb}|$  matrix element of the CKM matrix since  $t\bar{t}$  production is an important background for the EW single-top production. More important, this cross-section is sensitive to new physics in top quark production and decay.

Given that the top quark decays almost 100% of the times into a  $W$  boson and a  $b$ -quark, typical final states for the pair-production process can be divided into three classes:

$$t\bar{t} \rightarrow W^+ b W^- \bar{b} \rightarrow q\bar{q}' b q'' \bar{q}''' \bar{b} \quad (1.57)$$

$$t\bar{t} \rightarrow W^+ b W^- \bar{b} \rightarrow q\bar{q}' b l \bar{\nu}_l \bar{b} + \bar{l} \nu_l b q \bar{q}' \bar{b} \quad (1.58)$$

$$t\bar{t} \rightarrow W^+ b W^- \bar{b} \rightarrow \bar{l} \nu_l b l' \bar{\nu}_{l'} \bar{b} \quad (1.59)$$

where the branching ratios are respectively: 46.2%, 43.5% and 10.3%. The three processes are referred to as the all hadronic, semileptonic and di-leptonic channels, respectively. The  $l$  refers to  $e$ ,  $\mu$  or  $\tau$ , but most of the results to date rely on  $e$  and  $\mu$  channels. The initial and final states can also radiate gluons that can be detected as additional jets.

A recent summary plot for  $t\bar{t}$  production cross-section measurements done at LHC and Tevatron is shown in Figure 1.17.

### 1.3.2 Single top production process: $tW$

The best way to study the properties of the  $Wtb$  vertex and to directly measure the  $|V_{tb}|$  matrix element at the LHC is via the measurement of the EW single-top quark production (see Figure 1.18 for the Feynman diagram for this process at LO). Measurements of the process cross-section are proportional to  $|V_{tb}|^2 g_W^2(tb)$ . The large production rate, at the LHC, allows a measurement of the matrix element with negligible statistical uncertainty (differently from what happens in other channels).

There are two approaches to treat the single-top production at the NLO. In the **5 flavor scheme (5F)** a massless  $b$ -quark contributes to the proton PDF and therefore

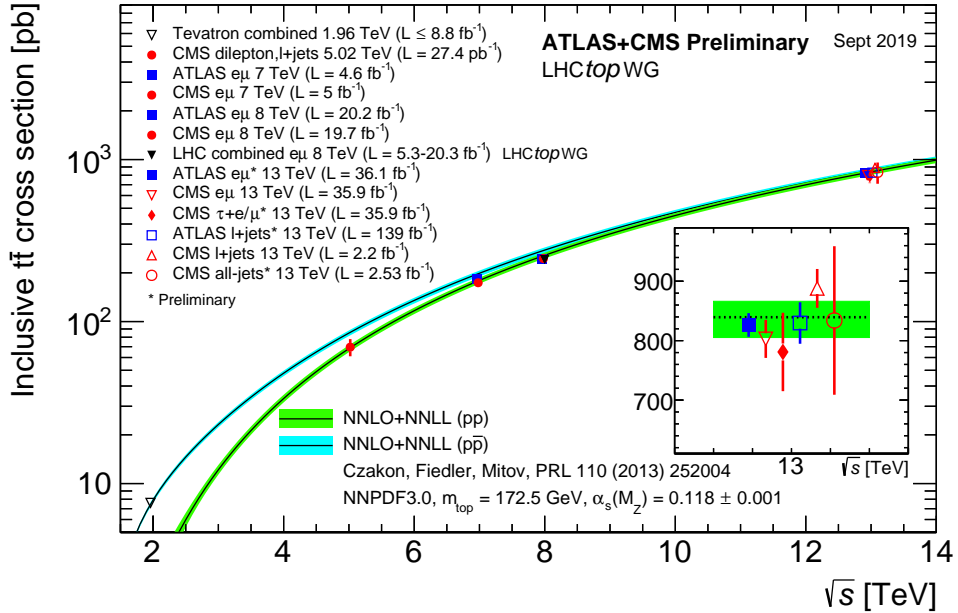


Figure 1.17: Summary of LHC and Tevatron measurements for the  $t\bar{t}$  production cross-section as a function of the centre-of-mass energy compared to the NNLO QCD calculation complemented with NNLL resummation (2019) [16].

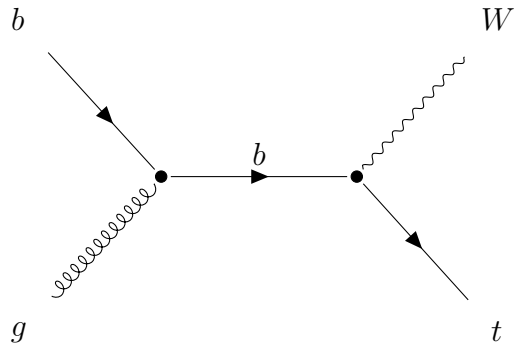


Figure 1.18:  $Wt$  channel single-top production process at the LHC at LO.

$b$ -initiated diagrams contribute at the lowest order in the calculation (see Eq. 1.60 and Figure 1.19b). In the **4 flavor scheme (4F)** initial-state  $b$ -quarks result from gluons via explicit  $g \rightarrow b\bar{b}$  splittings (see Eq. 1.61 and Figure 1.19a) [17]. The two processes are represented by the following equations:

$$gb \rightarrow W^- W^+ b \quad (1.60)$$

$$gg \rightarrow W^- W^+ b\bar{b} \quad (1.61)$$

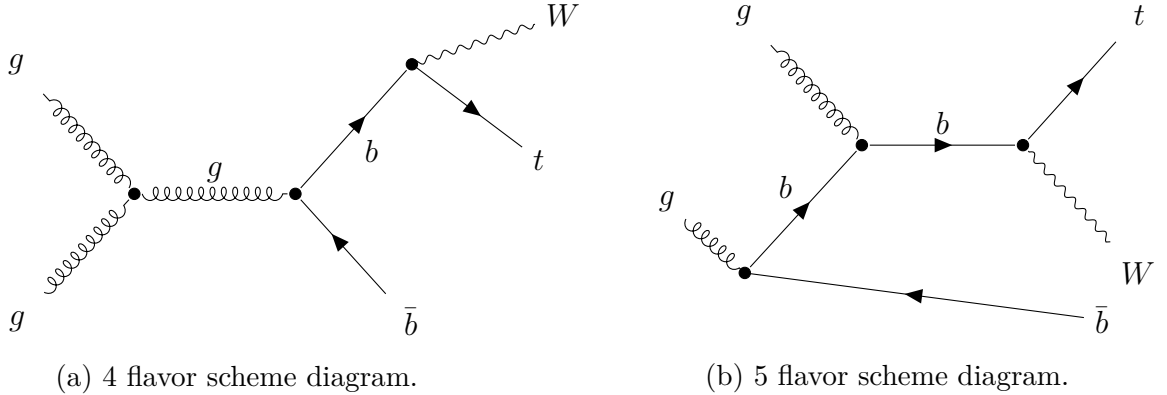


Figure 1.19: Example of NLO diagram contributions to the  $tWb$  single-top production.

The presence of a single  $b$ -jet at LO represents a clearly distinctive feature with respect to the  $t\bar{t}$  decay. But this separation ceases to exist beyond the LO, since the  $t\bar{t}$  process enters also the NLO corrections to  $Wt$  production. This will be deeply explained later in Section 1.3.3.

Let's start from the *Born Level* computation of the cross-section at LO. In this treatment all the quarks are taken as massless, including the  $b$  quark. The  $\sigma$  can be written as:

$$d\sigma^{(0)} = \mathcal{M}^{(0)} d\phi_2 \quad (1.62)$$

where  $d\phi_2$  is the two-body final state phase space and  $\mathcal{M}^{(0)}$  is the Born-level matrix element, defined as:

$$\mathcal{M}^{(0)} = \frac{1}{2s} \frac{1}{4} \frac{1}{N(N^2 - 1)} g_s^2 \frac{g_W^2}{8} |\mathcal{A}^{(0)}|^2 \quad (1.63)$$

with:  $g_s$  and  $g_W$  respectively the strong and weak coupling constants,  $s$  squared center-of-mass energy,  $N$  number of colours and  $\mathcal{A}^{(0)}$  spin-number Born-level matrix element [18].

To get a NLO description of the process, it is necessary to introduce two kind of corrections:

- **Virtual corrections:** in this case one-loop virtual diagrams in  $d = 4 - 2\epsilon$  dimensions are calculated. Virtual corrections are Laurent series in the parameter  $\epsilon$  with different poles and singularities. To solve the problem, some quantities as the strong coupling  $g_s$  and the top mass  $m_t$  are renormalized providing a contribution to the amplitude from the expansion of the renormalized top quark propagator, where there are terms proportional to the Born amplitude  $\mathcal{A}^{(0)}$  and the modified amplitude  $\mathcal{A}'^{(1)}$  involving the "squared" top quark propagator. Therefore, in terms of the *finite remainder* the cross-section receives the contribution:

$$d\sigma_{\delta m_t}^{1,V} = (\delta m_t)_{finite} d\sigma^{(0)} (\mathcal{A}^{(0)} \mathcal{A}'^{\dagger(1)} + \mathcal{A}'^{(1)} \mathcal{M}^{\dagger(0)}). \quad (1.64)$$

- **Real corrections:** for this correction, the matrix elements are computed by the fictitious  $W$  boson decays:

$$W(q) \rightarrow Q(p) + \bar{b}_3(q_3) + g_4(q_4) + g_5(q_5) \quad (1.65)$$

$$W(q) \rightarrow Q(p) + \bar{b}_3(q_3) + b_4(q_4) + \bar{b}_5(q_5) \quad (1.66)$$

where  $Q$  denotes generally the only quark with mass different from zero. These corrections come from gluon-radiation and initial-gluon diagrams. In particular, for gluon radiation:

$$\sigma^{gr} = \sigma_s^{gr} + \sigma_c^{gr} + \sigma_{fin}^{gr} \quad (1.67)$$

where the three terms are respectively contributions from: soft, collinear and non-collinear regions [19].

For the initial gluon process:

$$\sigma^{ig} = \sigma_c^{ig} + \sigma_{fin}^{ig} \quad (1.68)$$

the two terms represent the contributions in the collinear and non-collinear regions.

Finally, it's necessary to construct a Monte Carlo (MC) subtraction term for the matching of the NLO computation with event generators. MC subtraction terms can be written as:

$$d\sigma|_{MC} = \sum_i \sum_L \sum_l d\sigma_i^{(L,l)}|_{MC} \quad (1.69)$$

where  $i$  indicates the different partonic subprocesses,  $L$  labels the parton leg from which the parton is emitted and  $l$  runs over different colour structures. There are also short-distance contributions that have to be taken into account for the subtraction term. See Figure 1.20 for a summary of the ATLAS and CMS collaboration measurements of the single-top production cross-section in the  $t$ -channel at 13 TeV center-of-mass energy.

### 1.3.3 Quantum interference between $t\bar{t}$ and $tWb$ processes

At LO, the  $Wt$  process is represented by the reaction:

$$bg \rightarrow tW. \quad (1.70)$$

This process has a smaller cross-section than top-pair production by a factor of about 15. Beyond the LO, some other Feynman diagrams contribute and they can be interpreted as the production of a  $t\bar{t}$  pair at LO, with subsequent decay of the  $\bar{t}$  into a  $\bar{b}W$  pair (see Figure 1.14 for an example of this kind of diagrams)<sup>4</sup>.

---

<sup>4</sup>From now on, only the case of top quarks produced through gluon-gluon fusion will be considered.

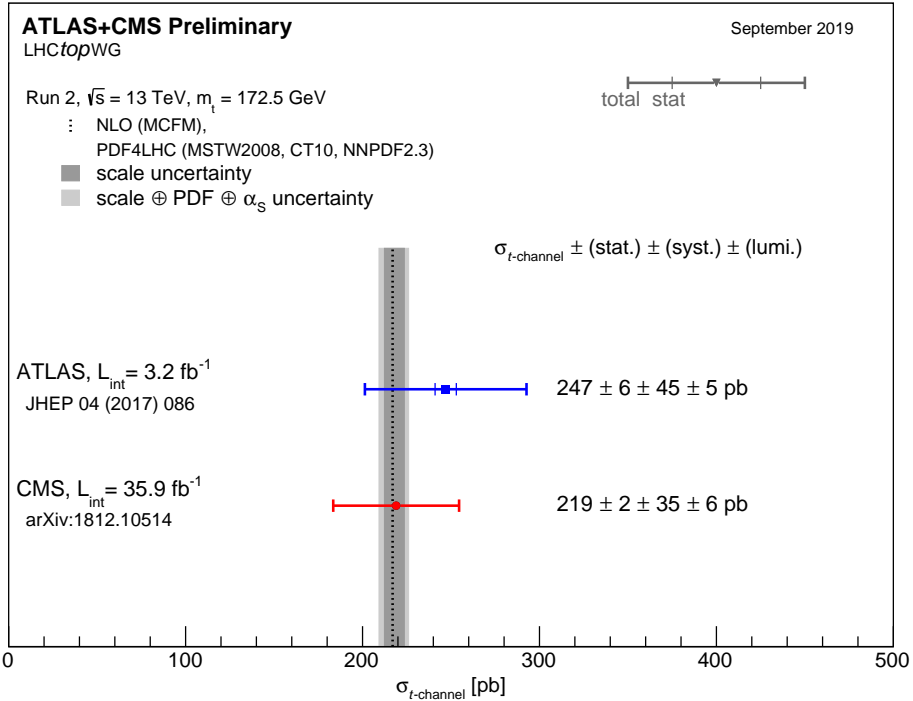


Figure 1.20: Summary of the ATLAS and CMS Collaborations measurements of the single top production cross-sections in the  $t$ -channel at 13 TeV center-of-mass energy. The measurements are compared with a theoretical calculation based on NLO QCD, computed assuming a top mass of 172.5 GeV [16].

Therefore, from this observations, the set of diagrams contributing to the 1.70 can be divided into two subsets denoted as **doubly resonant** (see Figure 1.14) and **singly resonant** (see Figure 1.19). The interference, briefly mentioned before, can happens between these two subsets of diagrams and can be physically interpreted as the interference between  $Wt$  and  $t\bar{t}$  productions [20]. It would not cause any problem if the contribution from doubly-resonant diagrams are small: it enters only at NLO contributions. A large increase of the cross-section occurs when the  $\bar{t}$  propagator becomes resonant.

It is important to find a way to separate out the  $Wt$  and  $t\bar{t}$  production and recover a workable definition of the  $Wt$  channel beyond the LO<sup>5</sup>.

When treating this kind of phenomena, one of the most important problems to deal with is the one of defining the  $Wt$  channel in a way that it is applicable in an event generator context, where both initial- and final-state parton showers are present.

The simplest solution (called Diagram Removal (DR)) is to remove from the compu-

<sup>5</sup>at LO the definition is not problematic.

tations the contributions of those processes which contain doubly-resonant diagrams.

There are more precise methods, designed in such a way that, by comparing them, one can directly assess the impact of the interference with  $t\bar{t}$ . Therefore, if the two results from the two definitions agree, we can be confident of having isolated the  $Wt$  channel. Some of the most used methods are:

- **Diagram Removal (DR):** where all the doubly resonant diagrams in the NLO  $Wt$  process amplitude are removed. This technique is different from the removal of the  $gg$  initiated process mentioned before, because diagrams with this initial state are kept if they aren't doubly-resonant.
- **Diagram Subtraction (DS):** where NLO  $Wt$  cross-sections are modified by implementing a subtraction term designed to cancel only locally the  $t\bar{t}$  contribution.

To describe this two methods, we introduce the notation  $\mathcal{A}_{\alpha\beta}$  as the  $\mathcal{O}(g_W \alpha_s)$  amplitude of the process:

$$\alpha + \beta \rightarrow t + W + \delta \quad (1.71)$$

where  $\delta$  is the parton (identified as the  $b$ -quark), that can be omitted in the notation. The total amplitude is therefore:

$$\mathcal{A}_{\alpha\beta} = \mathcal{A}_{\alpha\beta}^{(Wt)} + \mathcal{A}_{\alpha\beta}^{(t\bar{t})} \quad (1.72)$$

where the two terms are respectively the singly and doubly resonant contributions diagrams to the  $Wt$  cross-section. At NLO, in the computation of the cross-section, appears this term:

$$|\mathcal{A}_{\alpha\beta}|^2 = \left| \mathcal{A}_{\alpha\beta}^{(Wt)} \right|^2 + 2 \operatorname{Re} \{ \mathcal{A}_{\alpha\beta}^{(Wt)} \mathcal{A}_{\alpha\beta}^{(t\bar{t})} \} + \left| \mathcal{A}_{\alpha\beta}^{(t\bar{t})} \right|^2 \equiv \mathcal{S}_{\alpha\beta} + \mathcal{I}_{\alpha\beta} + \mathcal{D}_{\alpha\beta} \quad (1.73)$$

where the first term is associated to the singly resonant diagrams, the second term is the quantum interference and the third term is the doubly resonant contribution.

The NLO real-emission contribution to the subtracted short-distance partonic cross-section including the flux factor and phase space is:

$$d\hat{\sigma}_{\alpha\beta} = \frac{1}{2s} (\mathcal{S}_{\alpha\beta} + \mathcal{I}_{\alpha\beta} + \mathcal{D}_{\alpha\beta}) d\phi_3 \quad (1.74)$$

where  $d\phi_3$  is the three-body final state phase-space and the hat denotes that the infra-red singularities have been subtracted. The hadroproduction cross-section resulting from the 1.74 is:

$$d\sigma = d\sigma^{(2)} + \sum_{\alpha\beta} \int dx_1 dx_2 \mathcal{L}_{\alpha\beta} d\hat{\sigma}_{\alpha\beta} \quad (1.75)$$

with  $d\sigma^{(2)}$  that indicates the contribution to the cross-sections that are not already included (Born, soft-virtual etc...) and  $\mathcal{L}_{\alpha\beta}$  parton-level luminosity. But, when NLO is

matched to parton showers, the equation needs to be modified by the subtraction of MC counterterms. It's possible to choose to absorb this terms in  $\hat{\mathcal{S}}_{\alpha\beta}$ , because is the only piece that contains particular singularities. So the DR and DS cross sections become:

$$d\sigma^{(DR)} = d\sigma^{(2)} + \sum_{\alpha\beta} \int \frac{dx_1 dx_2}{2x_1 x_2 s} \mathcal{L}_{\alpha\beta} (\hat{\mathcal{S}}_{\alpha\beta} + \mathcal{I}_{\alpha\beta} + \mathcal{D}_{\alpha\beta} - \tilde{\mathcal{D}}_{\alpha\beta}) d\phi_3 \quad (1.76)$$

$$d\sigma^{(DS)} = d\sigma - d\sigma^{subt} \quad (1.77)$$

where  $d\sigma^{subt}$  is designed to remove numerically the doubly-resonant contribution and  $\tilde{\mathcal{D}}_{\alpha\beta}$  is defined such that  $\mathcal{D}_{\alpha\beta} - \tilde{\mathcal{D}}_{\alpha\beta}$  will vanish when  $m_{bW}^2 \rightarrow m_t^2$ . The DR cross-section has the problem to be not gauge invariant, but this isn't a problem in practice, by repeating the DR calculation in a number of alternative gauges. Then, the difference between the two Eqs. 1.77 and 1.76 is:

$$d\sigma^{(DS)} - d\sigma^{(DR)} = \sum_{\alpha\beta} \int \frac{dx_1 dx_2}{2x_1 x_2 s} \mathcal{L}_{\alpha\beta} (\mathcal{I}_{\alpha\beta} + \mathcal{D}_{\alpha\beta} - \tilde{\mathcal{D}}_{\alpha\beta}) d\phi_3 \quad (1.78)$$

that depends on the interference term and the  $\mathcal{D}_{\alpha\beta} - \tilde{\mathcal{D}}_{\alpha\beta}$  difference.

A gauge invariant subtraction term can be found by choosing an appropriate value of the  $\tilde{\mathcal{D}}_{\alpha\beta}$ .

Writing all this calculations in amplitudes notation we get:

$$|\mathcal{A}_{\alpha\beta}|_{DR}^2 = |\mathcal{A}_{\alpha\beta}^{Wt}|^2 \quad (1.79)$$

$$|\mathcal{A}_{\alpha\beta}|_{DS}^2 = |\mathcal{A}_{\alpha\beta}^{Wt}|^2 - \left[ \left| \mathcal{A}_{\alpha\beta}^{Wt} + \mathcal{A}_{\alpha\beta}^{t\bar{t}} \right|^2 - C^{SUB} \right] \quad (1.80)$$

with  $C^{SUB}$  cross-section level subtraction term. From this equations we get:

$$|\mathcal{A}_{\alpha\beta}|_{DR}^2 - |\mathcal{A}_{\alpha\beta}|_{DS}^2 = 2 \operatorname{Re} \{ \mathcal{A}_{\alpha\beta}^{(Wt)} \mathcal{A}_{\alpha\beta}^{t\bar{t}} \} \quad (1.81)$$

It exists also another approach, called **Diagram Removal 2 (DR2)** in which doubly resonant amplitudes are only included in the interference term, but it is less used with respect to the previous ones [14].

### 1.3.4 Interference term in BSM context

As mentioned at the beginning of Section 1.3, the study of the quantum interference between  $t\bar{t}$  and  $Wt$  is important also for BSM studies. An example is the search for top squarks performed by ATLAS in 2016 [21]. Beside the definition of the **signal region** (*SR*), the so-called **control regions** (*CRs*) for the constraining of the main background processes, are also taken into account. Two of the most important background processes

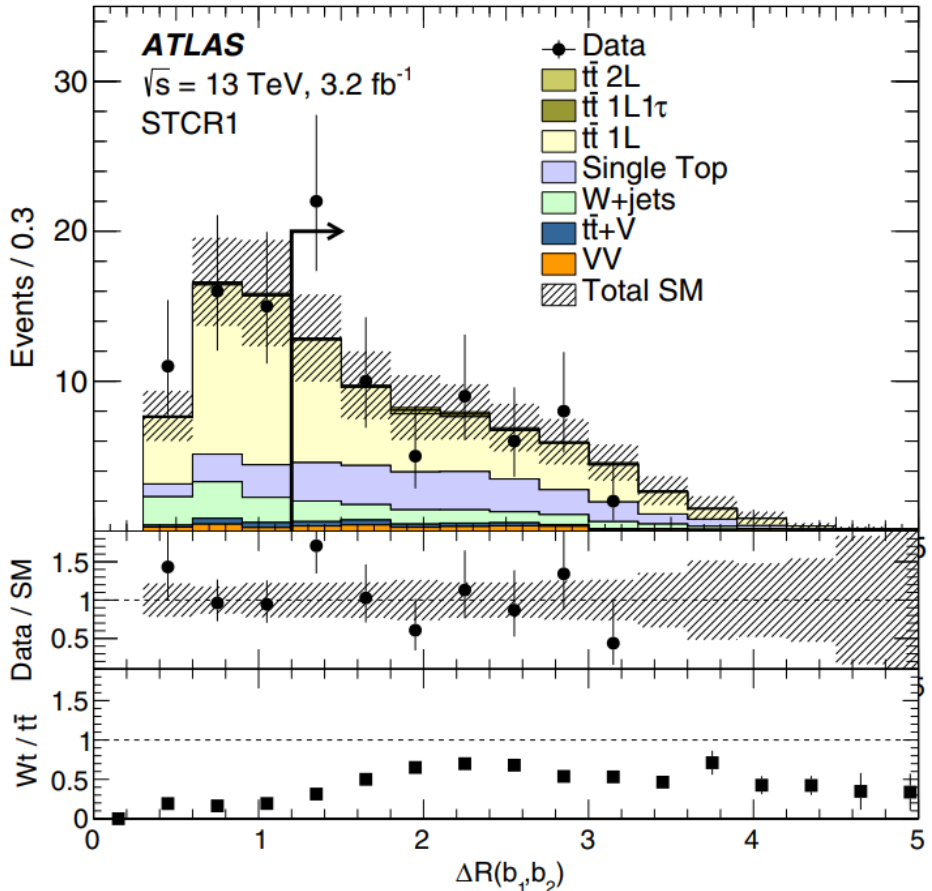


Figure 1.21: Single-top control region (STCR1). Data are compared to the background after the simultaneous fit on the  $\Delta R(b_1, b_2)$  distribution. To increase the purity of  $Wt$  events, a cut is applied, in order to take events only for  $\Delta R(b_1, b_2) > 1.2$ . Label  $L$  stands for *lepton*,  $\tau$  for *hadronic decay*,  $1L\ 1\tau$  for *semileptonic decay* and  $V$  for *vector boson*.

are the  $t\bar{t}$  and the  $Wt$  productions, because most of the  $t\bar{t}$  and  $Wt$  events in the signal region are from the dileptonic decay mode. Let's take a look to the single-top CR (see Figure 1.21). It is really difficult to separate double- and single-top events, because of the quantum interference they are subject to. To increase the purity of  $Wt$  events, some cuts on the used variable are performed. Events are measured as a function of the angular distance between the two final  $b$ -jets  $\Delta R(b_1, b_2)$ .

An improvement in the study of this interference would give better sensitivity in the measurement of this kind of background regions and consequently better discrimination between signal and background for SUSY particle searches.

### 1.3.5 State-of-the-art of the measurements

The  $WbWb$  final-state differential cross-section is usually measured as a function of variables that are sensitive to the interference term in particular regions of the phase-space. At present, the only complete measurement of this region has been performed by ATLAS in 2018 [14]. One of the most suited parameters used is the invariant mass of a

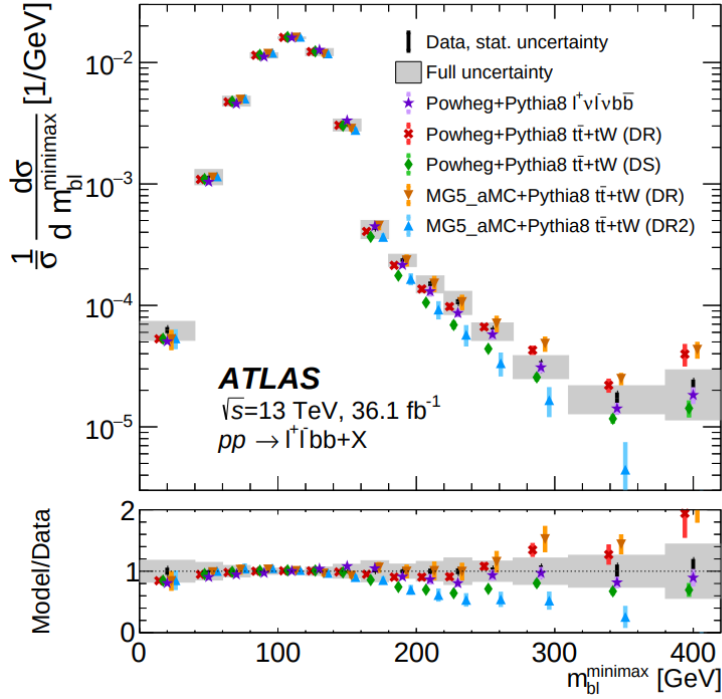


Figure 1.22: Normalized differential cross-section as a function of the  $m_{bl}^{\text{minimax}}$ , compared with different theoretical models of the  $t\bar{t} + tWb$  signal with various interference effects. Uncertainties of each data point include all statistical and systematic sources, while uncertainties for each of the MC predictions corresponds to theoretical ones.

$b$ -jet and a lepton. Since there is ambiguity in forming this pair, a different observable, called  $m_{bl}^{\text{minimax}}$ , is used in order to separate the relatively small single-top contribution from the dominant fraction of  $t\bar{t}$  events. It is defined as:

$$m_{bl}^{\text{minimax}} \equiv \min\{\max(m_{b_1 l_1}, m_{b_2 l_2}), \max(m_{b_1 l_2}, m_{b_2 l_1})\} \quad (1.82)$$

where  $b_i$  and  $l_i$  represent the two  $b$ -jets and leptons, respectively.

For doubly resonant top-quark events, at parton level, it holds:  $m_{bl}^{\text{minimax}} < \sqrt{m_t^2 - m_W^2}$ , therefore the differential cross-section above this kinematic endpoint has increased sensitivity to interference effects: the interference region starts to be significant for  $m_{bl}^{\text{minimax}} >$

155 GeV and in particular, above the 200 GeV threshold, the contribution of two on-shell top final state is suppressed and interference effects become large. Results are shown in Figure 1.22. Some other theoretical studies and tests have been performed in order to understand this phenomena. One of them is reported in [18], where the cross-sections as a function of the transverse momentum of the lepton-pair  $p_T^{ll}$  and the minimum transverse momentum  $p_T^{\min}$  are reported (see Figure 1.23). From this study it is possible to

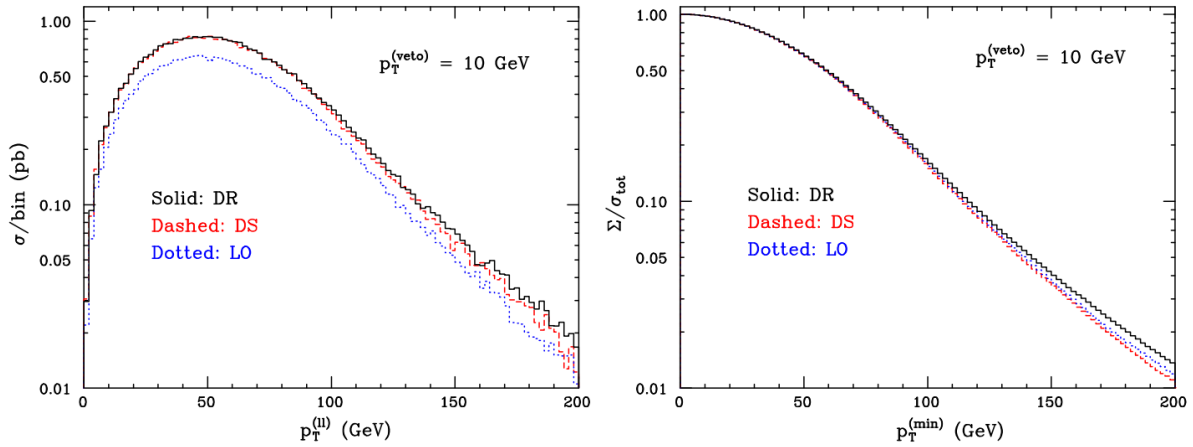


Figure 1.23: On the left the differential DR, LS and LO distributions as a function of  $p_T^{ll}$  are reported. On the right, the integrals of the same distributions, divided by the respective total rates are shown. Results are relevant for  $p_T^{\text{veto}} = 10 \text{ GeV}$ .

see that the impact of interference can be large for large values of  $p_T^{ll}$  and  $p_T^{\min}$ . But at so large values the cross-section is small. This results show that for the majority of events, the impact of interference is moderate, but, on the other hand, they imply that the cross-section of the  $Wt + t\bar{t}$  interference is observable dependent.

# Chapter 2

## The ATLAS detector

In December 1951, in Paris, after an intergovernmental meeting of UNESCO, was taken the first decision about the establishment of a European Council for Nuclear Research. Two months later, an agreement was signed, establishing the provisional council: the acronym **CERN** (*Conseil Européen pour la Recherche Nucléaire* in French) was born. After 18 months, the Council produced the first formal Convention. During the years, the main research topics of CERN moved from Nuclear Physics to High Energy Physics (Particle Physics). Due to this, its laboratory is often referred to as the European Laboratory for Particle Physics [22].

It hosts the largest proton accelerator of the world: the **LHC** (*Large Hadron Collider*) (described in Section 2.1). The latter contains four experiments, among which one of them is the **ATLAS** (*A Toroidal LHC ApparatuS*) experiment (described in Section 2.2) (see Figure 2.1).

### 2.1 The LHC collider

The LHC is situated in a 27 km tunnel that was constructed between 1984 and 1989 for the LEP (*Large Electron-Position*) collider at CERN, in Geneva. It is a two-ring-superconducting-hadron accelerator and collider. This tunnel has 8 straight sections and 8 arcs and lies between 45 m and 170 m below the surface of the *Léman lake*. There is a pair of tunnels that links the LHC to the CERN complex, each of them of approximately 2.5 km.

In December 1994, the CERN Council approved the LHC project. After exactly 2 years, in 1996, the Council approved the construction of the 14 TeV accelerator.

The previous accelerator (LEP) needed almost 344 superconducting RF cavities, due to the high energy loss for radiation, caused by the small mass of the electron-positron

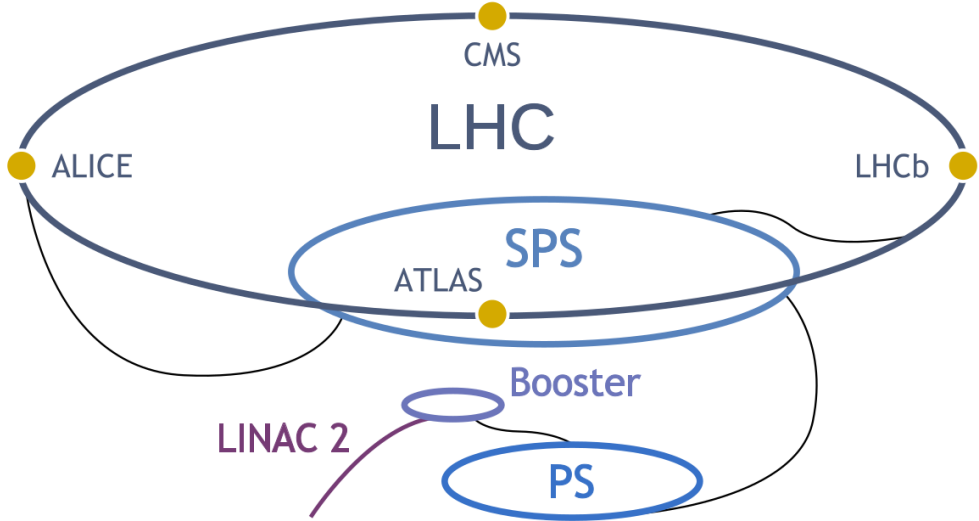


Figure 2.1: A diagram showing the complete structure of the LHC facility at CERN. There are the 4 main experiments (ATLAS, CMS, LHCb and ALICE) and the small accelerators that feed protons into the collider (PS, SPS, LINAC 2 and Booster) [23].

(almost 500 keV) used as beam component:

$$E_{\text{loss}} \propto \frac{1}{m^4}. \quad (2.1)$$

LHC collides protons that have masses of almost  $10^3$  times larger than the one of the electrons, so it needs only 8 superconducting RF cavities [24].

The collider contains two adjacent parallel beam pipes, separated by 194 mm, where beams circulate in opposite directions. The two pipes intersect only at four interaction points, where four experiments have been placed to detect particles produced in the collisions (see Figure 2.2). These experiments are:

- ATLAS (*A Toroidal LHC ApparatuS*): it is designed for “general purposes” in particle physics.
- CMS (*Compact Muon Solenoid*): designed for purposes similar to ATLAS.
- LHCb (*Large Hadron Collider beauty*): dedicated to bottom quark physics and CP violation studies.
- ALICE (*A Large Ion Collider Experiment*): it involves heavy ions (Pb-Pb collisions) or protons at 5.5 TeV/nucleon and is dedicated to quark-gluon plasma studies.

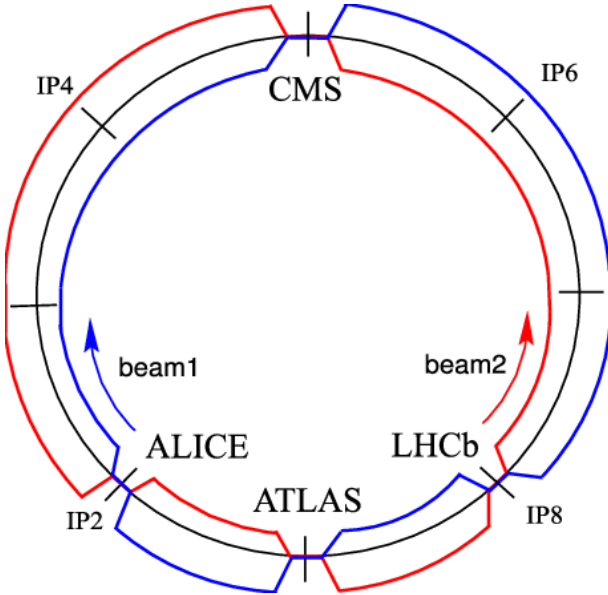


Figure 2.2: Minimal layout of the LHC structure: there are 8 interaction points (IPs) in total, which only 4 of them host the detectors (ATLAS, CMS, ALICE and LHCb). Beam 1 and beam 2 are circulating in opposite direction to encourage collisions [25].

Proton beams circulate along the LHC ring inside vacuum tubes, “driven” by magnets. The vertical magnetic field in the dipoles curves the beams by the Lorentz force and keeps them on a circular trajectory. To maintain in orbit these high energy beams, superconducting magnets are used, cooled by a huge cryogenic system.

### 2.1.1 Luminosity

The LHC was developed to reach up to 14 TeV center-of-mass collision energies (CM). A very important quantity in colliders is the **luminosity**. The **instantaneous luminosity**  $\mathcal{L}$  is defined as the ratio between the rate of produced events  $R$  and the cross-section of the considered process,  $\sigma$ :

$$\mathcal{L} = \frac{R}{\sigma} \quad (2.2)$$

Units of measurement are  $\text{cm}^{-2}\text{s}^{-1}$ . The instantaneous luminosity depends on beam properties:

$$\mathcal{L} = \frac{N_p^2 n_b f \gamma}{4\pi \epsilon_n \beta^*} F \quad (2.3)$$

where  $N_p$  is the number of protons,  $n_b$  is the number of bunches per beam,  $f$  is the revolution frequency,  $\gamma = E/m$  is the relativistic factor ( $E$  is the energy),  $\epsilon_n$  is the normalized beam emittance,  $\beta^*$  is the beam beta function or focal length at the collision

point and  $F$  is the luminosity reduction factor due to the crossing angle at the interaction point (IP). The latter is defined as:

$$F = \left( 1 + \frac{\theta_c \sigma_z}{2\sigma_{xy}} \right) \quad (2.4)$$

where  $\theta_c$  is the beam crossing angle and  $\sigma_z$  and  $\sigma_{xy}$  are the longitudinal and transverse RMS beam sizes at the interaction point.

ATLAS is one of the highest luminosity experiments at the LHC and aims at a peak luminosity of:

$$\mathcal{L} = 1 \times 10^{34} \text{ cm}^{-2}\text{s}^{-1} \quad (2.5)$$

The high beam intensity required for such a high luminosity excludes the use of anti-proton beams, and hence exclude the particle-antiparticle collision in this case. So, the LHC is designed as a proton-proton (or ion) collider, with separate magnetic fields and vacuum chambers in the main arcs and with common sections only in the regions in which the detector lies. The two beams share a 130 m long common beam pipe along the interaction points.

The number of circulating protons ( $N_p$ ) is usually of the order of  $O(10^{11})$ . Together with the large number of bunches ( $n_b$ ), that is almost 2808 for each proton beam, and a nominal bunch spacing of 25 ns, other nominal parameter values are:  $N_b = 1.1 \times 10^{11}$  (particles per bunch),  $f = 11.2 \text{ kHz}$ ,  $\epsilon_n = 3.75 \mu\text{m}$ ,  $\beta^* = 0.55 \text{ m}$ ,  $\theta_c = 285 \mu\text{rad}$ ,  $\sigma_{xy} = 16.7 \mu\text{m}$  and  $\sigma_z = 7.55 \text{ cm}$ .

The peak beam energy depends on the integrated dipole field around the storage ring, which implies a peak dipole field of 8.33 T for the 7 TeV in the LHC and the use of superconducting magnet technology.

Another very important parameter is the **luminosity integrated in time** ( $T$ ), defined as the ratio of the number of events  $N$  produced at a rate  $R$  with a certain cross section  $\sigma$ :

$$L = \int_0^T \mathcal{L} dt = \frac{N}{R} \quad (2.6)$$

that is measured in  $\text{fb}^{-1}$  (b are barns). LHC delivered an integrated luminosity of  $5.6 \text{ fb}^{-1}$  of proton-proton collision data at the center-of-mass energy of 7 TeV in 2010 and 2011. In 2012 the energy was increased to 8 TeV and the LHC luminosity was upgraded significantly and ATLAS recorded an amount around  $14.3 \text{ fb}^{-1}$  [26]. During the Run-2 period, from 2015 to 2018, at a CM energy of 13 TeV, it collected a total integrated luminosity of  $139 \text{ fb}^{-1}$ . In Figure 2.3 the total integrated luminosities collected by ATLAS and the recorded luminosities in function of the number of interactions per crossing of each year of Run-2 are shown.

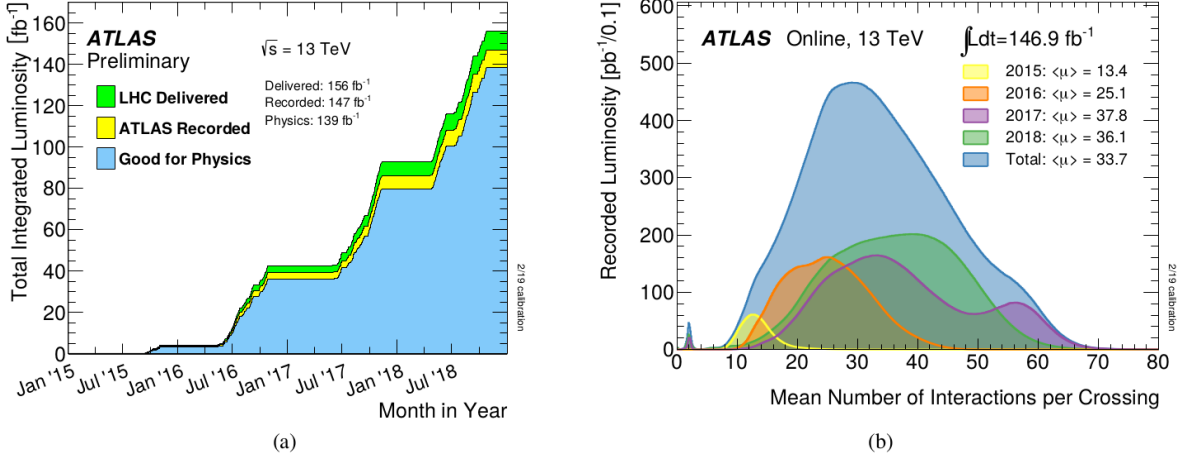


Figure 2.3: Figure (a): total integrated luminosity collected by ATLAS in Run-2. Figure (b): recorded luminosity as a function of the number of interactions per crossing in each year of Run-2 [27].

### 2.1.2 Magnets

The LHC relies on **superconducting magnets**, that are at the edge of the present technology. It makes use of the well-proven technology based on NbTi Rutherford cables and cools the magnets to a temperature below 2 K, with superfluid He operating at magnetic fields above 8 T. Such a reduced temperature leads to a significant reduction of the heat capacity of the cable by almost an order of magnitude, therefore the energy deposit that can trigger a quench<sup>1</sup> is substantially reduced. This means that the temperature margin must be larger and is needed a tight control of movements and heat dissipation inside cables. Due to the increasing of the electromagnetic forces (that increase with the square of the magnetic field), the structure retaining the conductor motion must be stronger than the previous designs.

The major part of the LHC magnets adopt the so called “two-in-one” structure: the windings for the two beam channels lie in a common cold mass and cryostat, with magnetic flux circulating in the opposite sense through the two channels. A cross-section of one of the LHC magnet with its components is shown in Figure 2.4.

In this configuration there are  $O(1000)$  dipoles to guide the beam and  $O(400)$  quadrupoles to focus it. Dipole magnets are done by copper-clad steel (CCS) with cables of NbTi, as mentioned above. For a 8 T field is required a  $O(1200)$  Ampère current and a 2 in 1 magnet design.

<sup>1</sup>A quench is an abnormal termination of magnet operation that occurs when part of the superconducting coil enters the normal resistive state.

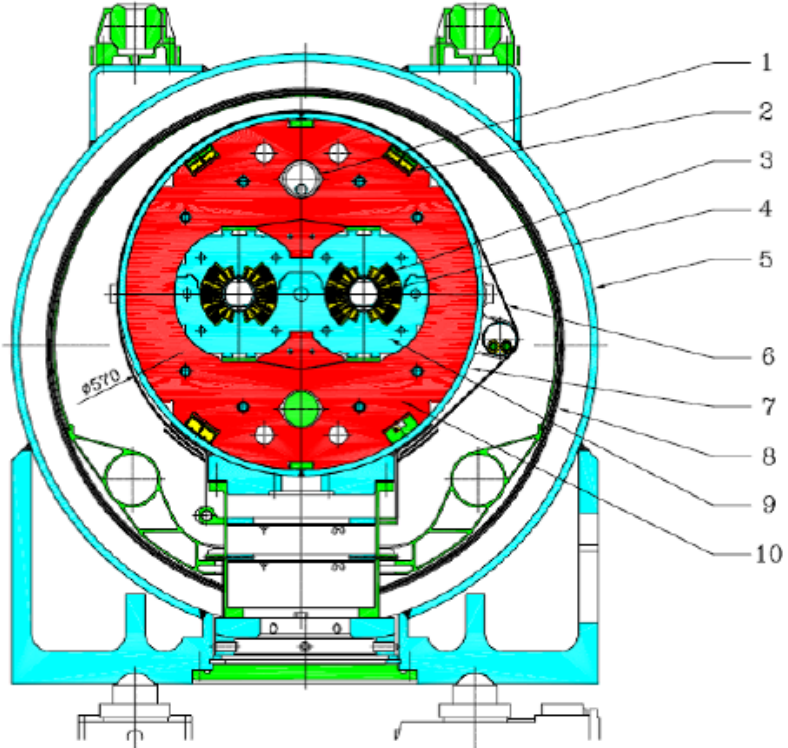


Figure 2.4: Cross-section of an LHC magnet. It consists of the following parts: (1) heat exchanger pipe, (2) superconducting busbars, (3) superconducting coils, (4) beam screen, (5) vacuum vessel, (6) radiation screen, (7) shrinking cylinder, (8) thermal shield, (9) non magnetic collars and (10) iron yoke [28].

### 2.1.3 Beam injection and acceleration

The injection of particle beams into the LHC is performed in the **injection insertions**, that are the IP2 and IP8 (see Figure 2.2). In both the insertions, the beam approaches the LHC from outside and below the machine plane. Then, a series of dipoles direct the beam in the injection line towards a series of five magnets, which deflect the beam horizontally by 12 mrad under the outer ring. A series of four kicker magnets deflects the beam vertically by 0.85 mrad onto the closed orbit. It is also used an injection beam stopper (TDI) placed 15 m upstream of the superconducting recombination dipole, supplemented by an additional shielding element, in a way to facilitate the procedure and to protect the collider in case of problems related to kickers. To complete the protection, also two collimators are used. The geometrical layout is very similar for both the IP regions, however, optics vary between them, due to displaced interaction point in IP8. The precision of the injected beam position with respect to the LHC closed orbit is

specified to be less than  $\pm 1.5\sigma$ .

Protons at the LHC are provided from the following injectors: **Linac2**, **PSB** (*Proton Synchrotron Booster* or simply *Booster*), **PS** (*Proton Synchrotron*) and **SPS** (*Super Proton Synchrotron*) (see Figure 2.1 for their representation in the LHC structure). This accelerators have been upgraded to satisfy all the LHC requirements (see Section 2.1.1). There are many conditions that have to be satisfied for the beam, the most important are:

- The beam emittance<sup>2</sup> has to fit the small aperture of the LHC superconducting magnets.
- The beam intensity has to be limited by the synchrotron radiation, that is absorbed by the cryogenic system.
- The spread in betatron tunes caused by the beam-beam effect when there is the collision between beams has to be kept under control.
- The space-charge limits in the injector have to be respected.

The intensity that the SPS is able to accelerate (almost  $4 \times 10^{13}$  protons per cycle) limits the number of PS pulses per SPS cycle to a maximum of 4. The momentum spread acceptace of the PS-SPS line is about  $\pm 0.2\%$  in  $\Delta p/p$  and the total bunch lenght has to be below 4 ns to fit the SPS accelerating system. This last requirement implies a longitudinal emittance of 0.35 eV per PS bunch. During the SPS acceleration, the longitudinal emittance is increased up to 1 eV.

PSB is composed by 4 rings, all them are normally ejected and sequentially transferred to fill the PS in one go, for example, for the SPS beam with two bunches per ring [30].

## 2.2 The ATLAS detector at the LHC

As mentioned in Section 2.1, the LHC hosts 4 big experiments among which one of them is the ATLAS experiment. ATLAS is a multipurpose detector, built for probing proton-proton collisions at very high energies [31]. It is substantially forward-backward symmetric with respect to the interaction point. Its main **sub-detectors** are:

- Tracking system (pixels, strips and transition radiation detectors).
- Electromagnetic and hadronic calorimeters.
- Muon spectrometer.

---

<sup>2</sup>Beam emittance is defined as the area covered by the beam. There is horizontal and vertical beam emittance [29].

- Magnetic System.

It contains also an inner solenoid, an outer toroidal magnetic field and trigger, readout, DAQ and control Systems. The dimensions of the detector are 25 m in height and 44 m in length. The weight of the whole detector is almost 7000 t (see Figure 2.5). It is located

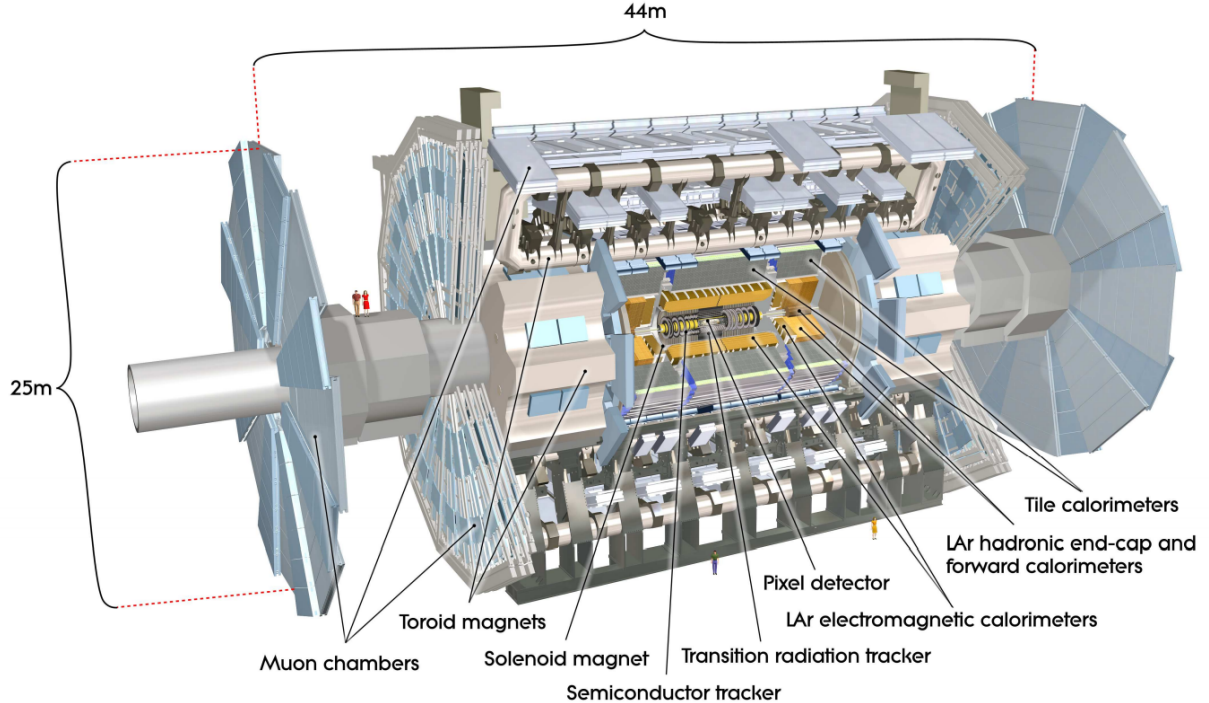


Figure 2.5: View of the main components of the ATLAS detector. The dimensions are 25 m in height  $\times$  44 m in length. It is composed by: muon chambers, toroid magnets, solenoid magnet, tracker system (pixel detector, semiconductor tracker and transition radiation tracker), liquid Argon electromagnetic and hadronic calorimeters and tile calorimeters.

at almost 100 m underground at IP1 of the LHC ring (see Figure 2.2). In addition to the main just mentioned components, there are also three smaller sets of detectors with the purpose to provide a good coverage in the forward region; from here, the name **Forward Detectors**. They will be only mentioned in this section, and are:

- **LUCID** (*L*uminosity *meas*urement using *C*herenkov *I*ntegrating *D*etector): it is a Cherenkov detector.
- **ZDC** (*Z*ero *D*egree *C*alorimeter): located at  $\pm 140$  m from the IP. It detects forward neutrons in heavy-ion collisions.

- **ALFA** (*Absolute Luminosity For ATLAS*): it consists of scintillating-fibre trackers located at a distance of  $\pm 240$  m from the IP. It is dedicated to total cross-section measurement.

Also additional proton-tagging detector are considered at an even greater distance from the IP of about  $\pm 420$  m. They, together with new radiation-hard detectors, are part of a possible future upgrade program.

### 2.2.1 Detector reference frame and requirements

In ATLAS a **right-handed Cartesian reference frame** is used. Collisions are produced in the origin, centered in the interaction point:

- The horizontal x-axis is pointing towards the center of the LHC ring.
- The vertical y-axis is pointing upwards.
- The z-axis is tangent to the beam line.

The x-y plane, orthogonal to the beam pipe, is called the **transverse plane**, while the z-axis direction is called **longitudinal plane**. Due to the cylindrical symmetry, polar coordinates can be used (see Figure 2.6 for a graphical representation):

- $\vec{r}$  is the distance from the interaction point, in the transverse plane x-y:

$$\vec{r} = \sqrt{x^2 + y^2} \quad (2.7)$$

- $\phi$  is the azimuthal angle, measured from the x-axis in the transverse plane and takes value from  $-\pi$  to  $+\pi$ .
- $\theta$  is the polar angle, measured from the z-axis in the longitudinal plane z-y and takes values from 0 to  $+\pi$ .

Most used variables are:

- The **transverse momentum**  $p_T = \vec{p} \sin \theta$ . “Invisible” particles that escape along the beam pipe have  $p_T \approx 0$ , so they are out of acceptance. The “visible”  $p_T$  is conserved:  $\sum_i p_{T,i} \approx 0$ . However,  $\vec{p}$  and  $\theta$  are not Lorentz invariant along z.
- The **rapidity** y:

$$\vec{y} = \frac{1}{2} \ln \frac{E + p_z}{E - p_z} = \frac{1}{2} \ln \frac{1 + \beta \cos \theta}{1 - \beta \cos \theta} \quad (2.8)$$

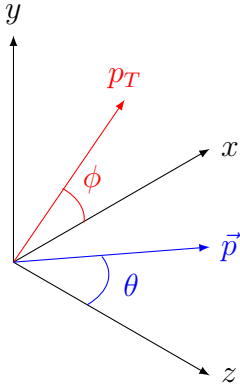


Figure 2.6: Graphical representation of the right-handed Cartesian reference frame: the x-axis is pointing towards the center of the LHC, the y-axis is pointing upwards and the z-axis is tangent to the beam line. The angles  $\phi$  and  $\theta$  are respectively the azimuthal angle from the x-axis in the transverse plane and the polar angle measured from the z-axis in the x-y longitudinal plane. Furthermore,  $\vec{p}$  is the momentum and  $p_T$  its transverse component.

- The **pseudo-rapidity**  $\eta$ , defined for  $\beta \rightarrow 1(m \ll p_t)$ :

$$\eta = -\ln \left( \tan \frac{\theta}{2} \right) \quad (2.9)$$

It is commonly used to describe the relative angle between a particle and the beam axis. Forward direction refers to the region which is close to the beam axis, corresponding to high values of  $|\eta|$  (see Figure 2.7).

The  $\Delta y$  and  $\Delta\phi$  are invariant for Lorentz boosts along z-axis. The pseudo-rapidity is useful also to describe the **angular distance** between 2 particles:

$$\Delta R = \sqrt{\Delta\eta^2 + \Delta\phi^2} \quad (2.10)$$

Global **requirements** that ATLAS has to satisfy for the LHC collider are:

- Fast, radiation-hard electronics and sensor elements. High detector granularity<sup>3</sup> is needed to handle the particle fluxes and to reduce the overlapping of events.
- Large acceptance in pseudo-rapidity with almost full azimuthal angle coverage.
- Good resolution for charged-particle momentum and efficiency in the tracking system.

---

<sup>3</sup>The granularity is defined as how much is sensitive the detector for unit cell (related to the tracker).

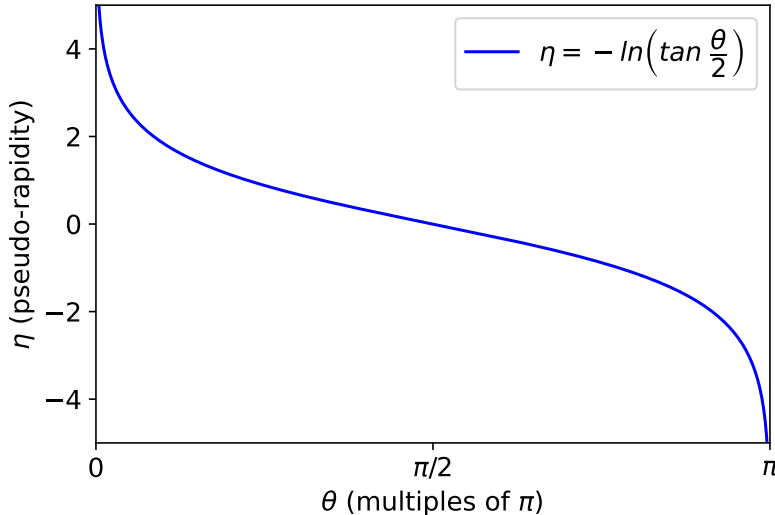


Figure 2.7: Pseudo-rapidity in function of the polar angle  $\theta$ .

- Very good electromagnetic calorimetry for electron and photon identification, complemented by an hadronic calorimetry for jets and missing transverse energy measurements.
- Good muon identification and momentum resolution and the ability to determine unambiguously the charge of high  $p_T$  muons.
- Excellent trigger system for low transverse momentum objects with a good background rejection.

Electromagnetic calorimeters cover the pseudo-rapidity range  $|\eta| < 3.2$ . The hadronic calorimetry covers the range  $|\eta| < 1.7$  and  $|\eta| > 1.5$ , matching the outer limits of end-cap electromagnetic calorimeters. The forward calorimeters provide both electromagnetic and hadronic energy measurements and extend the pseudo-rapidity to  $|\eta| = 4.9$ . General performance goals of the ATLAS detector are shown in Table 2.1.

### 2.2.2 Magnet system

The ATLAS unique hybrid magnet system is composed by 4 **superconducting magnets**. The dimensions of the system are 22 m in diameter for 26 m in length, with a stored energy of 1.6 GJ. Superconducting magnets provide a magnetic field over a total volume of almost 12 000 m<sup>3</sup>. This is defined as the region in which the field exceeds, with an intensity of 50 mT. The system is composed mainly by:

Detector Component	Required Resolution	$\eta$ coverage	
		Measurement	Trigger
Tracking	$\sigma_{p_T}/p_T = 0.05\% p_T \oplus 1\%$	$\pm 2.5$	
EM Calorimetry	$\sigma_E/E = 10\%/\sqrt{E} \oplus 0.7\%$	$\pm 3.2$	$\pm 2.5$
Hadronic Calorimetry (jets) barrel and end-cap forward	$\sigma_E/E = 50\%/\sqrt{E} \oplus 3\%$ $\sigma_E/E = 100\%/\sqrt{E} \oplus 10\%$	$\pm 3.2$ $3.1 <  \eta  < 4.9$	$\pm 3.2$ $3.1 <  \eta  < 4.9$
Muon Spectrometer	$\sigma_{\vec{p}_T}/\vec{p}_T = 10\% \text{ at } \vec{p}_T = 1 \text{ TeV}$	$\pm 2.7$	$\pm 2.4$

Table 2.1: General performance goals of the ATLAS detector: the required resolution and the  $\eta$  coverage (for measurement and trigger) of each main component of the ATLAS experiment are shown.

- A **solenoid**: it is aligned on the beam axis and provides an axial magnetic field of 2 T for the inner tracker and minimize the radiative thickness in front of the barrel electromagnetic calorimeter.
- A **barrel toroid** and **two end-cap toroids**: they provide a total toroidal magnetic field of 0.5 T and 1 T for the muon detector, respectively in the central and end-cap regions. Each end cap toroid contains eight racetrack coils, mounted as a single cold mass in a cryostat vessel of approximately 10 m diameter [32].

A brief representation of the position of the magnets in the detector is shown in Figure 2.5. A more representative geometry of the magnet system is shown in Figure 2.8.

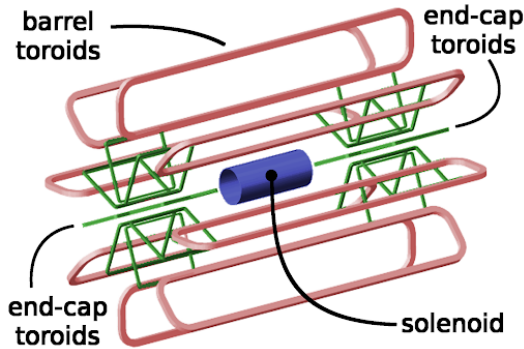


Figure 2.8: Geometrical representation of the magnet system. It is formed by: barrel toroids, solenoid and two end-cap toroids. The eight barrel toroid coils, with the end-cap coils interleaved are visible. The solenoid winding lies inside the calorimeter volume [33].

### 2.2.3 Tracking system

The **Inner Detector (ID)** consists of an important part of the tracking system of ATLAS. Its purpose is to reconstruct charged particles tracks and vertices (its tracking measurements are in a range matched by precision measurements of the electromagnetic calorimeter) and to measure their momentum, that has to lie above a given value of the transverse momentum and within the pseudo-rapidity range  $|\eta| < 2.5$ . Its dimensions are 2.1 m in height and 6.2 m in length. It consists of three types of sub-detectors: **Pixel Detector**, **Semiconductor Tracker (SCT)** and **Transition Radiation Tracker (TRT)** (see Figure 2.9). All the sub-detectors are contained within a cylindrical envelope of

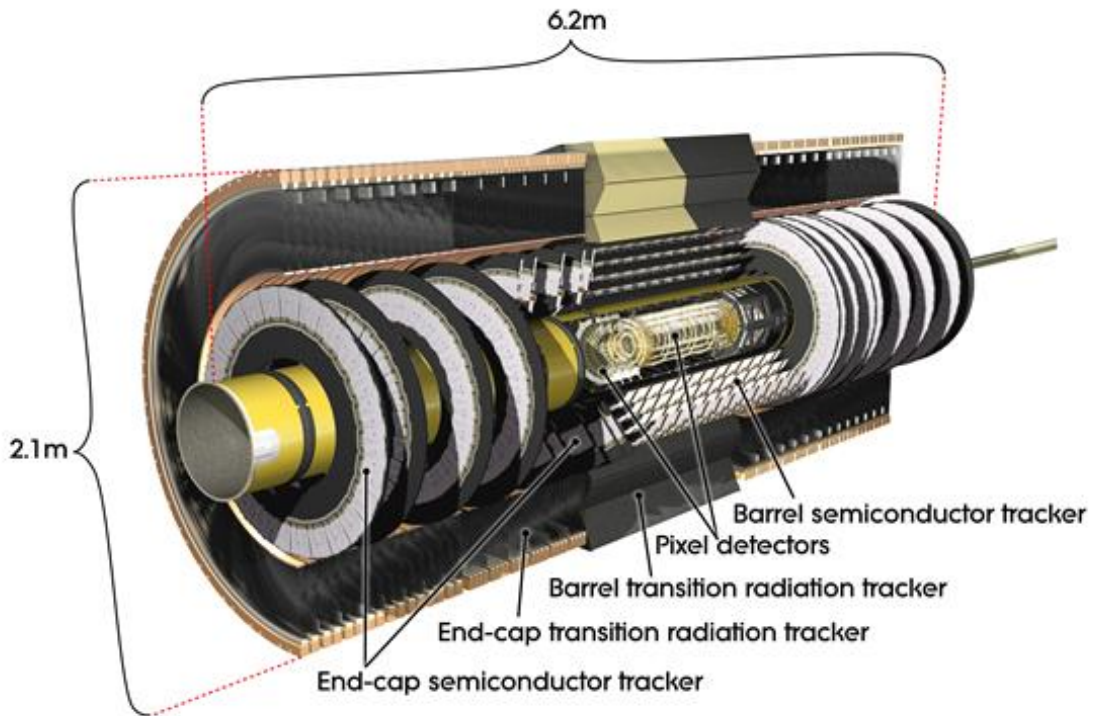


Figure 2.9: Layout of the ATLAS Inner Detector. It is formed by: semiconductor tracker, transition radiation tracker and pixel detectors.

length 3512 mm and radius 1150 mm in the barrel region. While, in the end-cap regions, they're located on disks perpendicular to the beam axis. This setup is surrounded by a magnetic field of 2 T.

The Pixel Detector is the one with the highest granularity and is situated very close to the interaction point. It has 1744 modules, that are arranged in three barrel layers and two end-caps each with three disk layers. Its intrinsic spatial resolution<sup>4</sup> is 10  $\mu\text{m}$  in

<sup>4</sup>Pixel layers are segmented in  $R - \phi$  and  $z$  with typically three pixel layers crossed by each track.

$R - \phi$  and  $115\text{ }\mu\text{m}$  in  $z$ . All pixel sensors are identical and have a minimum pixel size in  $R - \phi \times z$  of  $50 \times 400\text{ }\mu\text{m}$ .

The Semiconductor Tracker is a silicon detector with microstrips which surrounds the Pixel Detector layers. It provides 8 measurements per track with resolution of  $16\text{ }\mu\text{m}$  in  $R - \phi$  and  $580\text{ }\mu\text{m}$  in  $z$ . It consists of 4088 modules tiling four coaxial cylindrical layers in the barrel region and two end-caps each containing nine disk layers.

The TRD is the outermost and provides typically more than 30 hits per track. It has a very good pattern recognition and contributes also to particle identification. It is composed by gaseous counter, filled with Xe, CO<sub>2</sub> and O<sub>2</sub> mixtures. It contains up to 73 layers of tubes interleaved with fibres and 160 straw planes interleaved with foils (end-cap), which provide transition radiation for electron identification.

In 2019 there was an excellent data taking performance between all the 3 sub-detectors, this was possible thanks to reliable Data Acquisition System (DAQ) and Detector Control System (DCS).

Tracks above a given  $p_T$  threshold are reconstructed offline within the full acceptance range  $|\eta| < 2.5$  of the whole Inner Detector, using multi-stage track identification algorithms.

Also detector alignment is very important for the parameter resolution: it is performed at 3 different levels of granularity, corresponding to the mechanical layout of the detector.

## 2.2.4 Calorimetry

ATLAS has an **electromagnetic (EM)** and an **hadronic (HAD) LAr calorimeters**. EM calorimeter is divided into a **barrel part** and two **end-cap** components; instead HAD calorimeter is composed by **tile**, **end-cap** and **forward** calorimeter regions (see Figure 2.10). All them cover the range  $|\eta| < 4.9$  using different techniques, related to the physics processes. Over the  $\eta$  region matched to the inner detector, the EM calorimeter fits ideally for the measurements of electrons and photons. The rest of the calorimeter is useful for the reconstruction of the jets topology and the measurement of the missing transverse energy  $E_T^{\text{miss}}$ .

The main purpose of the calorimeters is to contain electromagnetic and hadronic showers; therefore the depth is a very important parameter. The total thickness of the EM calorimeter is more than  $22\text{ }X_0$  (radiation lengths) in the barrel with  $9.7\text{ }\lambda$  interaction lengths and more than  $24\text{ }X_0$  in the end-caps, with 10 interaction lengths. The total thickness is  $11\text{ }\lambda$  at  $\eta = 0$ .

As mentioned before, the EM calorimeter has a barrel part, that covers the region  $|\eta| < 1.475$  and two end-cap components, that cover the region  $1.375 < |\eta| < 3.2$ . The central solenoid is in front of the EM calorimeter; as a consequence, the latter and the calorimeter share a common vacuum vessel. The barrel EM calorimeter is composed by two coaxial wheels: an outer wheel that covers the region  $1.375 < |\eta| < 2.5$  and an

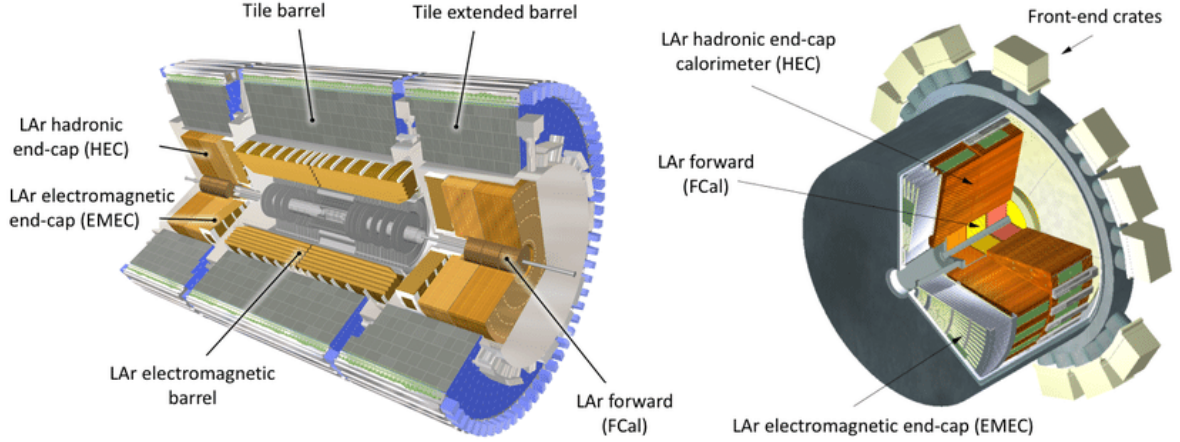


Figure 2.10: Cut-away view of the ATLAS calorimetry. EM calorimeter is divided into a barrel part and two end-caps components. HAD calorimeter is composed by tile, end-cap and forward calorimeter regions [34].

inner one in the region  $2.5 < |\eta| < 3.2$ . Over the region devoted to precision physics ( $|\eta| < 2.5$ ), the whole calorimeter is segmented into three sections in depth. For what regard the end-cap inner wheel, the calorimeter is segmented in two sections in depth. In the region  $|\eta| < 1.8$  is used a presampler detector, that consists of an active layer of LAr, that is used to absorb the energy lost by electrons and photons upstream the calorimeter.

HAD calorimeter is composed by:

- **Tile calorimeter:** it is placed directly outside the EM calorimeter envelope. It has a barrel that covers the region  $|\eta| < 1.0$  and two extended barrels in the range  $0.8 < |\eta| < 1.7$ . It is basically a sampling calorimeter that uses steel as absorber and scintillating tiles as active material. The tile calorimeter extends radially from an inner radius of 2.28 m to an outer one of 4.25 m. It is segmented into three layers of approximately 1.5, 4.1 and 1.8  $\lambda$  for the barrel and 1.5, 2.6 and 9.7  $\lambda$  at  $\eta = 0$ .
- **LAr hadronic end-cap calorimeter:** it consists of two wheels per end-cap, that are located behind the EM calorimeter. It extends out to  $|\eta| = 3.2$ , to reduce the transition between the end-cap and the forward calorimeter, that is at  $|\eta| = 3.1$ . It overlaps also the tile calorimeter ( $|\eta| < 1.7$ ) by extending to  $|\eta| = 1.5$ . The wheels closest to the interaction point are built from 25 mm parallel copper plates, each of them with an outer radius of 2.03 m; while those further away use 50 mm copper plates, with an inner radius of 0.475 m.
- **LAr forward calorimeter:** it provides coverage in the region  $3.1 < |\eta| < 4.9$  [35].It

is integrated into the end-cap cryostats and provides benefits in terms of the calorimetric coverage, reducing radiation background levels in the muon spectrometer. It has approximately  $10 \lambda$  depth and consists of three modules in each end-cap: one, in copper, is for electromagnetic measurements, while the other two, in tungsten, are for the measurement of the hadronic interaction energy.

### 2.2.5 Muon spectrometer

The muon spectrometer of the ATLAS detector is composed by the following sub-detectors: **monitored drift tubes (MDTs)**, **cathode strip chambers (CSC)**, **resistive plate chambers (RPCs)** and **thin gap chambers (TGCs)**. See Figure 2.11 for a cut-away view. It is based on the magnetic deflection of muon tracks in the large

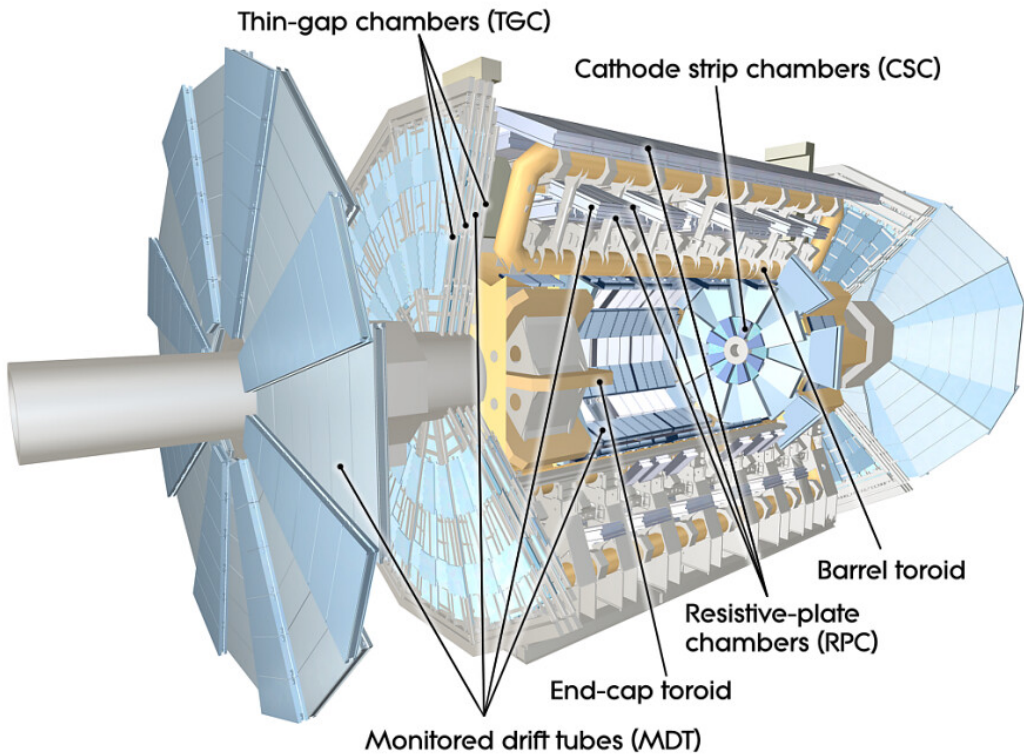


Figure 2.11: Cut-away view of the ATLAS muon spectrometer. It is composed by: monitored drift tubes (MDTs), cathode strip chambers (CSC), resistive plate chambers (RPCs) and thin gap chambers (TGCs). It has also a barrel and an end-cap toroid. Its dimensions are: 24 m in diameter by 44 m in length.

superconducting air-core toroid magnets, instrumented with separate trigger and high-precision tracking chambers, in which ensures a three-point measurement of tracks [36].

Its momentum resolution is  $2 - 3\%$  at  $10 - 100 \text{ GeV}/c$  and  $10\%$  at  $1 \text{ TeV}$ . The latter quantity is estimated by taking into account also the high-level background environment, the inhomogeneous magnetic field and the large size of the apparatus, that is  $24 \text{ m}$  in diameter by  $44 \text{ m}$  in length.

The barrel toroid provides a magnetic bending in the range  $|\eta| < 1.4$ . In the region  $1.6 < |\eta| < 2.7$ , muon tracks are bent by two smaller end-cap magnets, inserted into both ends of the barrel toroid, mentioned before. Finally, in the transition region  $1.4 < |\eta| < 1.6$ , magnetic deflection is provided with the barrel and end-cap fields together. Thanks to this magnet configuration, the field is orthogonal to the muon trajectories and minimizes the degradation of resolution due to multiple scattering. The toroids provide almost  $3 \text{ T} \times \text{m}$  bending power<sup>5</sup> in the barrel region and  $6 \text{ T} \times \text{m}$  in the end-cap one.

The choice of some performance parameters, like the rate capability, the granularity, the ageing properties and the radiation hardness, is affected by the high level of particle flux.

In the barrel region, all the tracks are measured in chambers arranged in three cylindrical layers around the beam axis, instead, in the transition and end-cap regions, the chambers are situated in planes perpendicular to the beam, always in three layers.

Also in this region, precision measurement of the muon tracks in the main bending direction of the magnetic field are performed by the MDTs. The three stations of the RPCs provide the trigger function, the bunch-crossing identification and the second coordinate measurements in the end-cap regions. Chambers in the barrel are placed at three different radii with respect to the beam line.

For what regard the muon chambers, each sense wire of the drift tubes is isolated in a way to guarantee a reliable operation. The higher granularity CSCs in the innermost plane are used, in the region  $2 < |\eta| < 2.7$ , to front the demanding rate and background conditions. Here, the trigger system covers the pseudorapidity range  $|\eta| < 2.4$ .

The overall performance over the large areas, in particular at highest momenta, depends on the alignment of the muon chambers with respect to each other and with respect to the overall detector. The singular muon momentum measurement needs a precision of  $30 \mu\text{m}$  on the alignment, both within each projective tower and between consecutive layers in immediately adjacent towers. Relative positions of the MDT chambers are monitored by 12000 sensors. The accuracy needed for the relative positioning of non adjacent towers to obtain a good mass resolution for multi-muon final states lies in the range of few mm.

---

<sup>5</sup>The bending power is defined as the integral of the magnetic field component normal to the muon direction, computed along an infinite-momentum muon trajectory between the innermost and the outermost muon-chamber planes:  $\int \vec{B} \cdot d\vec{l}$ .

## 2.2.6 Trigger and data acquisition system

The ATLAS TDAQ (*Trigger and Data Acquisition*) system is responsible for *online processing*, selecting and storing events of interest of the *offline analysis*. Events are selected using a two-stage trigger system, composed by: **Level-1 (L1)** and **High-Level Trigger (HLT)** steps [37]. A diagram of the whole TDAQ system is shown in Figure 2.12. The L1 trigger is an hardware-based system that uses custom electronics to trigger

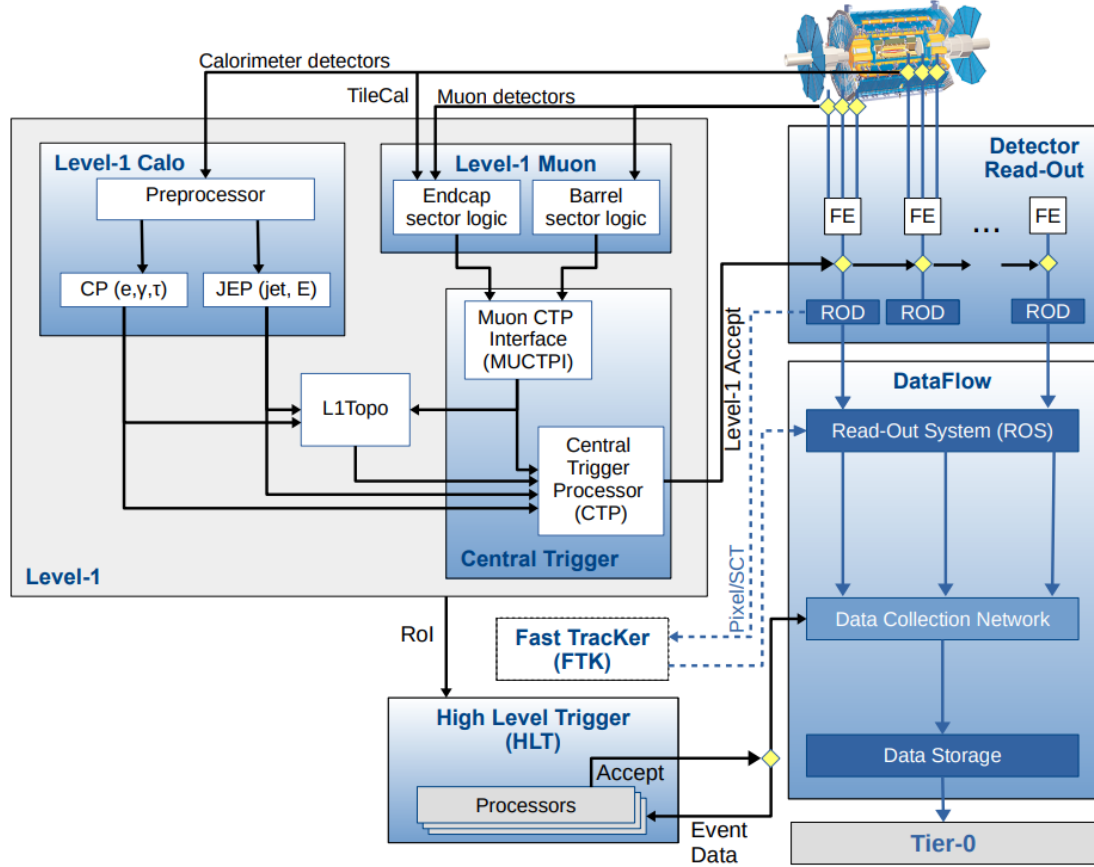


Figure 2.12: Block diagram of the ATLAS TDAQ system. It is possible to see the two-stage trigger system (L1 and HLT) and the detector read-out with data flow.

on reduced-granularity information from the calorimeter and muon detectors. The **L1 calorimeter (L1Calo)** trigger takes signal from the calorimeter detectors as input. The analogue detector signals are digitised and calibrated by the preprocessor and sent in parallel to the *Cluster Processor (CP)* and *Jet/Energy-sum Processor (JEP)*. This CP system identifies electrons, photons and  $\tau$ -leptons candidates above a certain threshold, while the JEP identifies jets candidates and produces global sums of total and missing

transverse energy (MET). Some objects with narrow clusters, such as electronics, aren't too much affected by small energy shifts, but the missing transverse momentum is very sensitive to small systematic shifts in energy over the entire LAr calorimeter. These effects are treated in the L1Calo trigger with a dedicated correction algorithm.

The **L1 muon trigger** (*L1Muon*) uses hits from the RPCs in the barrel and TGCs in the endcaps, in order to determine the deviation of the hit pattern from that of a muon with infinite momentum.

The **L1 trigger decision** is composed by: the *Central Trigger Processor* (*CPT*), which receives inputs from the L1Calo trigger, the *L1Muon Central Trigger Processor Interface* (*MUCTPI*) and the *L1 topological trigger* (*L1Topo*) [38]. In this decision also trigger signals from detector subsystems (LUCID Cherenkov for example) are considered. The CPT is responsible for applying the *dead time*, which is a mechanism used to limit the number of L1 accepts to be within constraints on the detector read-out latency.

The L1 trigger can also select events by considering event-level quantities (such as the total energy in the calorimeter), the multiplicity of objects above thresholds (such as the  $p_T$  of a muon) and the topological requirements (invariant masses for example). The L1 trigger accept events up to a rate of 100 MHz, down from the bunch crossing rate of 40 MHz, within a latency of 2.5  $\mu$ s.

For each L1-accepted event, the **Front-End** (*FE*) detector electronics reads out the event data for all detectors. Events are sent first to the *ReadOut Drivers* (*RODs*), for the preprocessing and than to the *ReadOut System* (*ROS*), for the data buffering. The L1 trigger defines also the so called **Regions of Interest** (*RoI's*), in which it selects the interesting events, identifying them with the  $\eta$  and  $\phi$  coordinates.

After passing the first stage, selected events enter the second stage of the triggering, that is the HLT trigger and is software-based (in particular on the offline software *Athena* [39]). For this reconstruction sequence dedicated fast trigger algorithms are used. These algorithms are executed on a computing farm, composed by 40000 selection applications, called *Processing Units* (*PUs*). In this selection part, in some cases, informations from the full detector are requested in order to reconstruct physics objects. The physics output rate of the HLT during an ATLAS data-taking run is on average 1.2 kHz with an average physics throughput to permanent storage of 1.2 GB/s.

Once the event passes the L1 and HLT, the *Sub-Farm Output* (*SFO*) sends the data to permanent storage for offline reconstruction and exports the data to the *Tier-0* facility at CERN computing center.

# Chapter 3

## Objects reconstruction

The **object reconstruction** is a fundamental step and needs to be performed at the beginning of the analysis procedure. It consists on the reconstruction and identification of particles produced after the  $pp$  collision in the detector. For our analysis, the most important objects we have to take into account are *electrons* (described in Section 3.1), *muons* (described in Section 3.2) and *tau leptons* (described in Section 3.3). Other objects are: *jets* (described in Section 3.4) and *missing transverse energy  $E_T$*  (described in Section 3.5). Finally in Section 3.6 the *overlap removal* problem is treated.

The total efficiency for the charged lepton reconstruction is:

$$\epsilon_{\text{total}} = \epsilon_{\text{reco}} \cdot \epsilon_{\text{id}} \cdot \epsilon_{\text{iso}} \cdot \epsilon_{\text{trig}} \quad (3.1)$$

that depends on: the *reconstruction efficiency*  $\epsilon_{\text{reco}}$ , the *identification efficiency*  $\epsilon_{\text{id}}$ , the *isolation efficiency*  $\epsilon_{\text{iso}}$  and the *trigger efficiency*  $\epsilon_{\text{trigger}}$ . Each efficiency depends on the selected step.

A **scale factor**, defined as the ratio between data and MC predictions, is used to correct the efficiencies in the MC simulation, to match those observed in data<sup>1</sup> [40].

### 3.1 Electron reconstruction

As mentioned in Section 1.3.3, electrons are fundamental ingredients for the study of the  $WbWb$  final states, in the  $ee$  and  $e\mu$  channels for example. The total efficiency for the electron reconstruction is given by the Eq. 3.1 by adding a factor  $\epsilon_{\text{EMclus}}$  that indicates the efficiency to reconstruct, in the EM calorimeter, by the EM-cluster candidates (that are localised energy deposits) associated with all produced electrons.

Isolated electrons are difficult to discriminate from other large backgrounds as: misidentified hadrons, electrons from photon conversion and non-isolated electrons originating

---

<sup>1</sup>It is a multiplicative scale factor for the simulation.

from heavy-flavor decays. The fraction of each background event is reduced with each of efficiency computation.

Electrons can lose a significant amount of their energy due to bremsstrahlung when they interact with nuclei of the material they cross. Photons radiated through the process may convert into an electron-positron pair that can interact with the detector material. All these objects (positrons, electrons and photons) are usually emitted in a collimated beam and are reconstructed as part of the same EM cluster. This interaction can occur inside the inner tracker volume or even in the beam pipe, generating tracks in the inner detector, or can occur downstream of the inner tracker, impacting the shower only in the EMCAL. So, it is possible to produce and match multiple tracks to the same EM cluster, all them originating from the same primary electron.

The electron reconstruction in the ATLAS  $|\eta| < 2.47$  precision region is given by the EMCAL and the inner tracker. It is based on three components, characterising the signature of electrons: localised clusters of energy deposits found within the EMCAL, charged-particle tracks identified in the inner tracker and close matching in  $\eta \times \phi$  space of the tracks to the clusters to form the final electron candidates. See Figure 3.1 for a schematic view of the path of an electron through the detector.

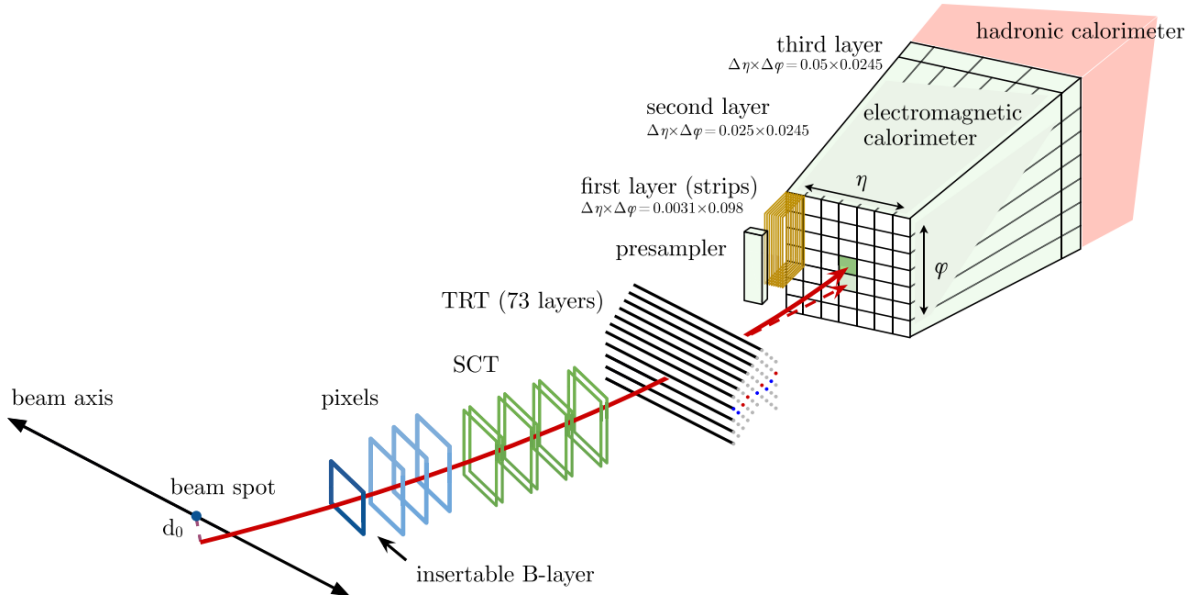


Figure 3.1: Schematic view of the path of an electron through the detector. The red line is the hypothetical trajectory of an electron, traversing first the tracking system and then entering the EMCAL. The dashed line indicates the path of a photon produced via bremsstrahlung in the tracking system [41].

### 3.1.1 Electron identification

To select electrons entering the  $|\eta| < 2.47$  region a **likelihood-based identification (LH)** is used. All the inputs to the LH include measurements from the tracking system, the calorimeter system and quantities that combine both their informations. Also probability density function (pdf) based on simulated events are constructed.

The LH is based on the products for signal  $L_S$  and for background  $L_B$  of  $n$  pdfs and is given by:

$$L_{S(B)}(\vec{x}) = \prod_{i=1}^n P_{S(B),i}(x_i) \quad (3.2)$$

where  $\vec{x}$  are  $n$ -component input vectors,  $P_{S,i}(x_i)$  is the value of the signal pdf for quantity  $i$  at value  $x_i$  and  $P_{B,i}(x_i)$  is the corresponding value of the background pdf. The signal is given by prompt electrons, while the background comes from the combination of jets that have a similar signature of prompt electrons, electrons from photon conversion in the detector material and non-prompt electrons given from the decay of hadrons containing heavy flavours.

For each electron candidate a discriminant  $d_L$  is formed, in order to combine  $L_S$  and  $L_B$ :

$$d_L = \frac{L_S}{L_S + L_B}. \quad (3.3)$$

This discriminant presents a sharp peak at unity for signal electrons and at zero for background.

In order to derive the pdfs for the electron LH, each one of them is determined for each identification quantity in separate bins of electron-candidate  $E_T$  and  $\eta$ . This pdfs are created from finely binned histograms of the individual identification quantities. Pdfs histograms are smoothed using an adaptive *kernel density estimators (KDE)* to avoid non-physical fluctuations. The pdfs for the missing transverse energy  $E_T$  range from 4.5 GeV to 15 GeV and are determined using  $J/\psi \rightarrow ee$  MC simulations while the others for  $E_T > 15$  GeV are determined using  $Z \rightarrow ee$  MC simulation.

In order to cover all the required prompt-electron signal efficiencies and background rejection factors (needed by the considered physics analyses), four fixed values of the LH discriminant are used, in order to define four **operating points**, that are: *Very-Loose*, *Loose*, *Medium* and *Tight*. These correspond to increasing thresholds for the LH discriminant. The efficiencies for identifying a prompt electron with  $E_T > 40$  GeV are 93%, 88% and 80% for the *Loose*, *Medium* and *Tight* operating points, respectively. The identification is optimized in bins of cluster  $\eta$  and bins of  $E_T$ <sup>2</sup>. All this points need some tracking criteria requirements: *Loose*, *Medium* and *Tight* points require at least two hits in the pixel detector and seven hits total in the pixel and silicon strip detectors

---

<sup>2</sup>Bins are selected by taking into account detector characteristics.

combined; while for Medium and Tight points one of these pixel hits must be in the innermost pixel layer. VeryLoose operating point doesn't include an explicit requirement on the innermost pixel layer and requires only one hit in the pixel detector. The latter point provides identification requirements for background studies.

Efficiencies for the LH-based electron identification for the Loose, Medium and Tight operating points for data and data-to-simulation ratios are shown in Figure 3.2 and 3.3. The measurement of efficiencies of the electron identification and isolation cuts are performed with the data using tag and probe techniques with large statistical sample of  $Z \rightarrow ee$  and  $J/\psi \rightarrow ee$  decays [42].

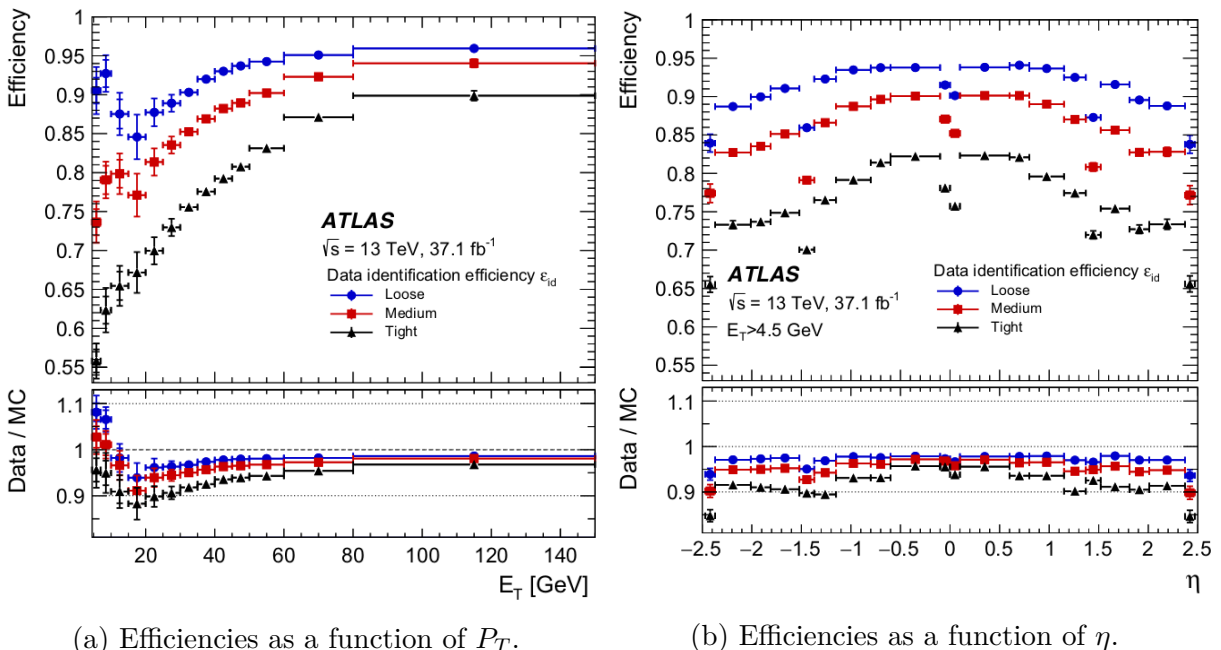


Figure 3.2: Measured LH electron-identification efficiencies in  $Z \rightarrow ee$  events for the Loose, Medium and Tight operating points, as a function of  $E_T$  and  $\eta$ . Vertical bars represent the statistical and total uncertainties. Bottom panel shows the data-to-simulation ratios.

### 3.1.2 Electron isolation

One of the most challenging steps in the electron reconstruction is the differentiation of the reconstructed object (electron in this case) in signal processes, from background processes. An hint of such a signal is represented by a small activity, both in the calorimeter and in the inner detector, in a region of  $\Delta\eta \times \Delta\phi$  surrounding the candidate object. However, the production of boosted particles decaying, for example, into collimated

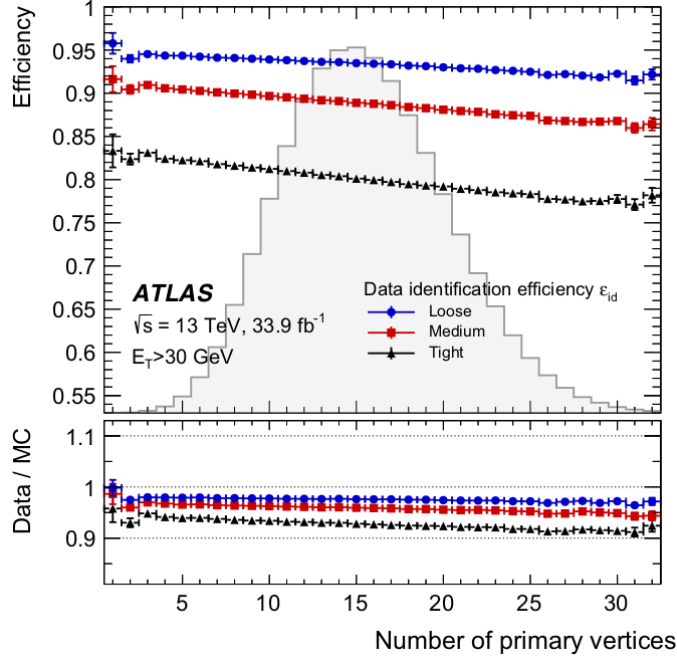


Figure 3.3: LH electron-identification efficiencies for electron candidates with  $E_T > 30 \text{ GeV}$  for the Loose, Medium and Tight operating points, as a function of primary vertices in the 2016 data taking, using the  $Z \rightarrow ee$  process. The histogram shows the distribution of the number of primary vertices for the data. Inner uncertainties are statistical, while the total ones include both statistical and systematics components. Bottom panel shows the data-to-simulation ratios.

electron-positron pairs or the production of prompt electrons, muons and photons such as  $t\bar{t}$  production can obscure the picture. Some variables are constructed in order to quantify the amount of activity close to the candidate object. They are built summing up transverse energies of clusters in the calorimeter or transverse momenta of tracks in a cone of radius  $\Delta R = \sqrt{(\Delta\eta)^2 + (\Delta\phi)^2}$  around the direction of the electron candidate, excluding the candidate itself.

Some of the fundamental steps entering the structure of this isolation variables are: identify the candidate object itself, its direction and its contribution to the activity within the cone and summing, in a pile-up and underlying event robust way, the other activity found within the cone. Isolation variables can be divided in two classes:

- **Calorimeter-based isolation:** the computation of calorimeter-based isolation in the early running period of ATLAS simply summed the  $E_T$  of the calorimeter cells (from EMCAL and HADCAL) within a cone aligned with the electron direction, excluding the candidate's contribution. A good improvement is obtained by using  $E_T$  of topological clusters instead of cells, applying a significant noise-suppression

algorithm to the collection cells. In Figure 3.4 a sketch of the calorimeter isolation method is shown. This method is simple and robust thanks to the stable sub-

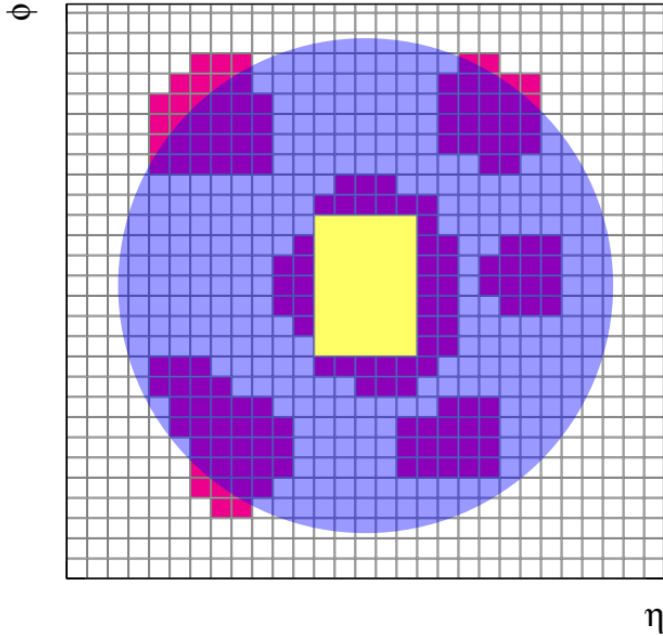


Figure 3.4: Sketch of the calorimeter isolation method: the grid represents the second-layer calorimeter cells in the  $\eta$  and  $\phi$  directions. The electron candidate is located in the center of the purple circle representing the isolation cone. All topological clusters are represented in red. The yellow-rectangled cells correspond to the subtracted cells in the core subtraction method (subtraction of the core energy around the candidate).

traction scheme for both the signal and background candidates. A disavantage of this method is that the candidate object may deposit energy outside of this fixed rectangular area which may be incorrectly assigned as additional activity.

- **Track-based isolation:** to compute track-based isolation variables, tracks with  $p_T > 1 \text{ GeV}$ , reconstructed with a fiducial region of the inner detector  $|\eta| < 2.5$ , that satisfy basic track-quality requirements, are used. This track selection includes a minimum number of hits identified in the silicon detectors and a maximum number of inoperable detector regions crossed by the track. To reduce the contribution of pile-up, a cut  $|z_0 \sin \theta| < 3 \text{ mm}$  is required, where  $z_0$  is the *longitudinal impact parameter*. This requirement aims to select tracks that originate from the vertex. Some track-based isolation variables are constructed by summing the transverse momenta of the tracks found within a cone of radius  $\Delta R$  aligned with the electron track, excluding the candidate's own contribution. Then the track- $p_T$  contribution

of the candidate electron to the track-isolation variable must be subtracted from the cone. The resulting track-isolation variable is called  $p_T^{\text{isol}}$ .

### 3.1.3 Electron triggers

ATLAS trigger system has been introduced in Section 2.2.6. The electron (and photon) reconstruction at the HLT stage is performed on each EM RoI, provided by L1, which satisfies  $E_T$  and isolation requirements as specified by the trigger menu [43]. To run precision algorithms at a reduced rate, later in the trigger sequence, the HLT fast algorithms are executed first. They operate by using calorimeter and ID (Inner Detector) information within the RoI to perform the initial selection and identification of the electron candidates (and achieve early background rejection).

If a particle passes the fast selection criteria, the precision algorithms in the HLT are executed, if it is possible to access detector informations outside the RoI. Therefore, the two main trigger selections are:

- **The L1 trigger** for electrons uses calorimeter information in the central region  $|\eta| < 2.5$  to build an EM RoI. Within the window, the algorithm uses the maximum  $E_T$  from the four possible pairs of nearest-neighbour EM towers in a  $2 \times 2$  central region<sup>3</sup>. Also a nominal  $E_T$  threshold and optionally a selection to reject hadronic activity below 50 GeV can be applied. Final step is an EM isolation requirement, in which candidate electrons are rejected if the sum of  $E_T$  in the 12 towers surrounding the  $2 \times 2$  central region in the EM layer is at least 2 GeV and exceeds the value  $E_T/8.0 - 1.8$  GeV.
- Also the **HLT electron reconstruction** has fast and precision steps. The fast calorimeter reconstruction and selection steps for electrons have two implementations: a cut-based algorithm and a neural network based *Ringer* algorithm<sup>4</sup>. The former is used for electron triggers with  $E_T < 15$  GeV, the latter is used for triggering electrons with  $E_T \geq 15$  GeV. Electron candidates are required to have tracks from the fast track reconstruction step, performed inside the RoI only, matching the corresponding cluster. In the precision calorimeter reconstruction step, precision tracks within the RoI are extrapolated to the second layer of the EM calorimeter and are required to match the clusters within  $|\Delta\eta(\text{track, cluster})| < 0.05$  and  $|\Delta\phi(\text{track, cluster})| < 0.05$  rad. Here, the electron selection relies on a multivariate technique using a LH discriminant with four operating points, similar to the ones of Section 3.1.1.

---

<sup>3</sup>This is used for EM  $E_T$  reconstruction.

<sup>4</sup>This algorithm exploits the property of EM showers to develop in the lateral direction in an approximately conical structure around the initial particle.

## 3.2 Muon reconstruction

As well as electrons, also muons are fundamental objects in our analysis because they form both the  $e\mu$  and  $\mu\mu$  final states of the decay. The muon reconstruction is performed independently in ID and MS (Muon Spectrometer). The information is then combined to form muon tracks, used for physics analyses. In the ID, muons are reconstructed as the other charged particles [44].

For the **MS reconstruction**, the algorithm starts with a search for hit patterns inside each muon chamber, to form segments. The MDT segments are reconstructed by performing a straight-line fit with the hits found in each layer. The RPC or TGC measure the coordinate orthogonal to the bending plane. The segments in the CSC detectors are built using a separate combinatorial search in the  $\eta$  and  $\phi$  detector planes. Muon track candidates are built by fitting together hits from segments in different layers. At least two matching segments are required to build a track, except in the barrel-endcap transition region where a single high-quality segment with  $\eta$  and  $\phi$  information can be used. The hits associated with each track candidate are fitted using global  $\chi^2$  fit.

Information from ID and MS tracks are then joint to perform a **ID-MS combined reconstruction**. It is performed according to various algorithms, based on the information provided by ID, MS and calorimeters. Depending on the subdetector used in the reconstruction, there are four muon types:

- **Combined (*CB*) muons:** here the track reconstruction is performed independently in the ID and MS, and a combined track is formed with a global refit that uses the hits from both ID and MS subdetectors.
- **Segment-tagged (*ST*) muons:** in this case a track in the ID is classified as a muon if, once extrapolated to the MS, it is associated with at least one local track segment in the MDT or CSC chambers.
- **Calorimeter-tagged (*CT*) muons:** here a track in the ID is identified as a muon if it can be matched to an energy deposit in the calorimeter, compatible with a minimum-ionizing particle. The criteria for the identification of this muons are optimised for the region  $|\eta| < 0.1$  in the momentum range  $1.5 < p_T < 100 \text{ GeV}$ .
- **Extrapolated (*ME*) muons:** for this muons the trajectory is reconstructed based only on the MS track and on a loose requirement on compatibility originating from the interaction point. This muons are mainly used to extend the acceptance for muon reconstruction into the region  $2.5 < |\eta| < 2.7$  (not covered by the ID).

The overlaps between different kind of muons are resolved before producing the final muons for the analysis. A scheme of all the reconstructed muon candidates is shown in Figure 3.5.

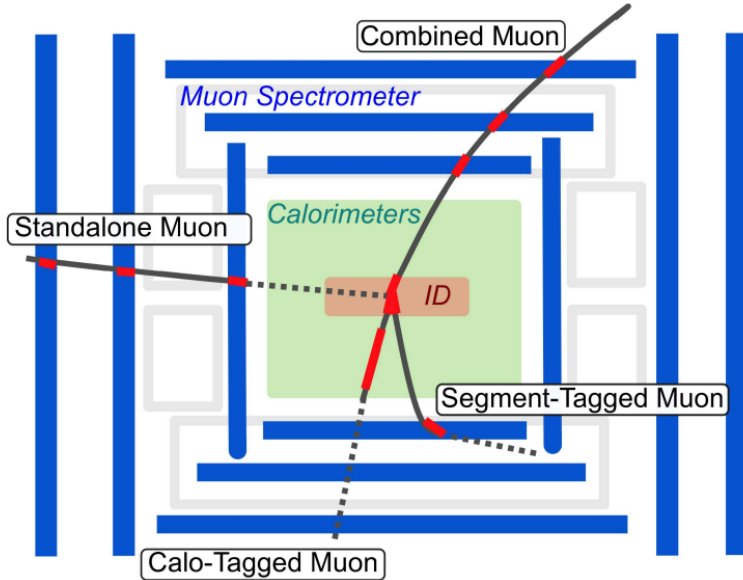


Figure 3.5: Scheme of all the reconstructed muon candidates [45].

### 3.2.1 Muon identification

Muon identification is performed by applying quality requirements that suppress background. To guarantee a robust momentum measurement, specific requirements on the number of hits in the ID and MS are used. Four muon identification selections, namely *Medium*, *Loose*, *Tight* and *High- $p_T$* , are provided to address the specific needs of different physics analyses:

- **Medium muons**: the Medium identification criteria is the default selection for muons in ATLAS. In this case only CB and ME tracks are used. The first ones are required to have at least 3 hits in at least two MDT layers, except for tracks in the  $|\eta| < 0.1$  region, where tracks with at least one MDT layer, but no more than one MDT hole layer, are allowed. Instead, the latter are required to have at least three MDT/CSC layers, and are employed only in the  $2.5 < |\eta| < 2.7$  region, to extend the acceptance outside the ID geometrical coverage.
- **Loose muons**: this criteria are designed to maximise the reconstruction efficiency while providing good-quality muon tracks. In this case all muon types are used. All CB and ME muons satisfying the Medium requirements are included in the Loose selection. CT and ST muons are restricted to the  $|\eta| < 0.1$  region. In the  $|\eta| < 2.5$  region almost all muons are CB.
- **Tight muons**: this muons are selected to maximise the purity of muons at the cost

of some efficiency. Here, only CB muons with hits in at least two stations of the MS and satisfying the Medium selection criteria are considered. In the  $2.5 < |\eta| < 2.7$  region muons are reconstructed using only the MS detector.

- **High- $p_T$  muons:** this selection aims to maximise the momentum resolution of tracks with  $p_T > 100 \text{ GeV}$ . CM muons that have passed the Medium selection and have at least three hits in three MS stations are selected.

### 3.2.2 Muon isolation

Muons originating from heavy particles are usually produced isolated from other particles and are well separated from them in the event. Therefore, the muon isolation is a powerful tool for background rejection in physics analyses. To define muon isolation, two variables are defined: a **track isolation variable** and a **calorimeter-based isolation variable**. The former is called  $p_T^{\text{varcone}30}$  and is defined as the scalar sum of the  $p_T$  of the tracks with  $p_T > 1 \text{ GeV}$  in a cone with size:

$$\Delta R = \min(10 \text{ GeV}/p_T^\mu, 0.3) \quad (3.4)$$

around the muon transverse momentum  $p_T^\mu$ , excluding the muon track itself.

The calorimeter-based variable  $E_T^{\text{topcone}20}$ , is defined as the sum of the  $E_T$  of topological clusters in a cone of size  $\Delta R = 0.2$  around the muon, after subtracting the contribution from the energy deposit of the muon itself and correcting for pile-up effects.

The real isolation criteria are constructed using the so-called *relative isolation variables*: they are defined as the ratio of track or calorimeter based isolation variables to the  $p_T$  of the muon. The distribution of this variables for muons coming from  $Z \rightarrow \mu\mu$  events are shown in Figure 3.6. Some isolation criteria, called *isolation working points*, are defined; each of them is optimised for different physics analyses. The efficiencies of this points are measured in data and simulation in  $Z \rightarrow \mu\mu$  decays, by using the *tag-and-probe* method<sup>5</sup>.

### 3.2.3 Muon triggers

The L1 muon trigger uses TGCs and RPCs hardware in order to select events by means of coarse  $p_T$  information. The L1 trigger also defines the RoIs<sup>6</sup>. The HLT muon trigger employs dedicated softwares to reconstruct muons in the RoIs defined by the L1, using informations from precision trackers, MDTs, CSCs and ID [46]. In addition to precise  $p_T$

---

<sup>5</sup>This method is employed to measure the efficiency of the muon identification selections within the acceptance of the ID ( $|\eta| < 2.5$ ). Are used  $Z \rightarrow \mu\mu$  events, with one of the two muons considered as a tag by requiring to match the single-muon trigger, and the other acting as a probe, to measure trigger efficiency.

<sup>6</sup>They are defined in terms of the pseudorapidity  $\eta$  and the azimuthal angle  $\phi$ .

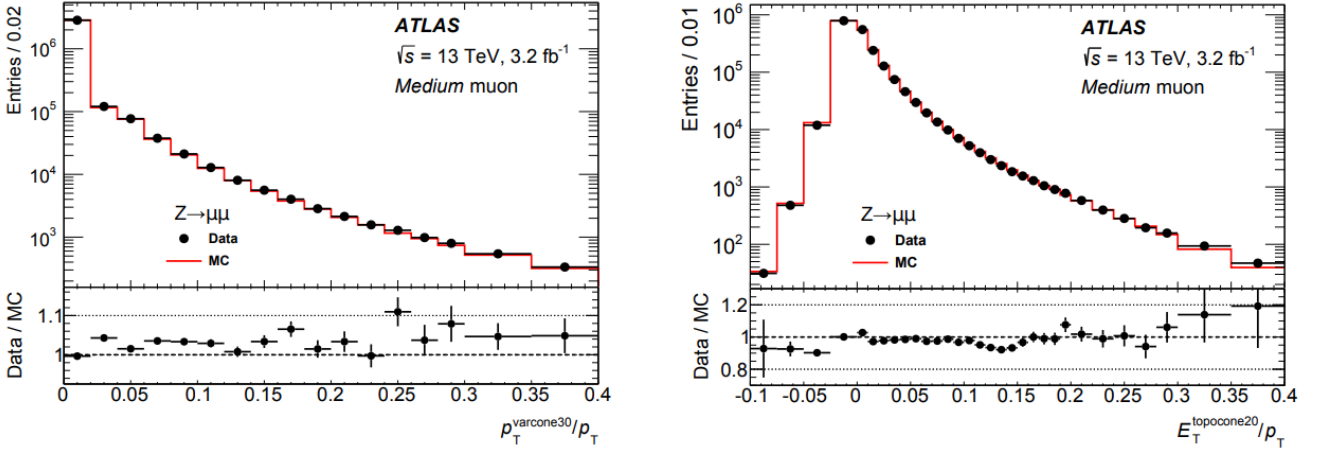


Figure 3.6: Left: distribution of the track based relative isolation variable. Right: distribution of the calorimeter-based relative isolation variable. Variables are measured in  $Z \rightarrow \mu\mu$  events. Muons included in the plots satisfy Medium identification criteria and are well separated from the other muon from the  $Z$  boson, that have  $\Delta R_{\mu\mu} > 0.3$ . Bottom panel shows the ratio to data to simulation. Dots show the distribution of data, while histograms show distribution from simulation.

measurements, for some triggers, isolation criteria are also applied to reject non-prompt muons. Muon trigger performances are studied by means of a tag-and-probe method. In Figure 3.7 the absolute efficiencies for muons with respect to the offline muon  $p_T$  in the barrel ( $|\eta| < 1.05$ ) and endcap ( $1.05 < |\eta| < 2.4$ ) regions are shown. Relative efficiency of the HLT with respect to L1 is superimposed in the plots with blue line. Values of efficiency in endcap are lower than in the barrel: this loss is due to uncovered detector regions.

The ATLAS muon trigger performance has been stable during Run 2. The L1 trigger decision in the barrel region is based on the coincidence of hits from three concentric RPC stations for the three high- $p_T$  thresholds. To reach optimal performance for the ATLAS trigger, an effective rejection of fake muon triggers in region  $1.05 < |\phi| < 1.3$  has been possible by exploiting a coincidence between the TGC chambers and the tile HADCAL. To verify the performance of the muon trigger in different pile-up conditions, the efficiency has been tested as a function of the number of reconstructed vertices (see Figure 3.8).

### 3.3 $\tau$ -lepton reconstruction

Tau leptons can produce electrons or muons in the final state (that have to be distinguished from electrons and muons originating from prompt W boson decays). These

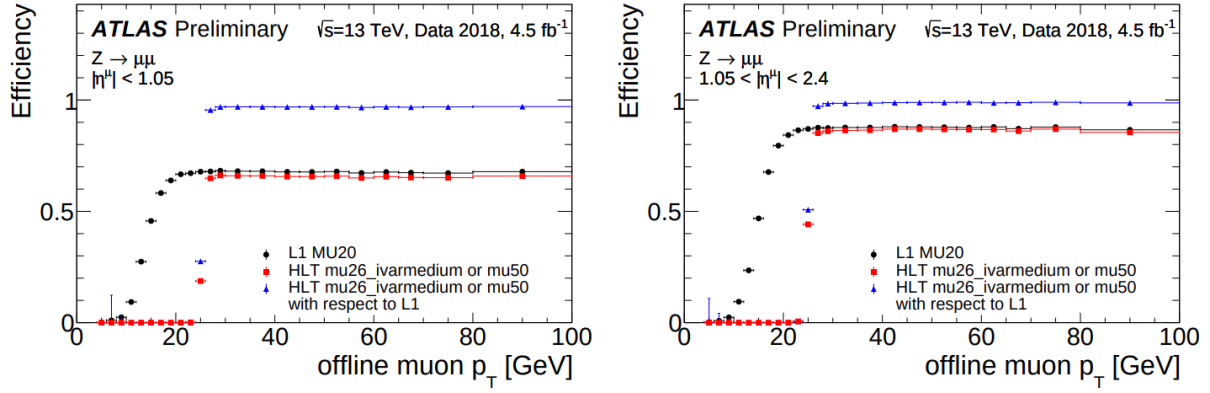


Figure 3.7: Absolute efficiencies for muons with respect to the offline muon  $p_T$  in the barrel ( $|\eta| < 1.05$ , left panel) and endcap ( $1.05 < |\eta| < 2.4$ , right panel) regions. Relative efficiency of the HLT with respect to L1 is superimposed in the plots with blue line.

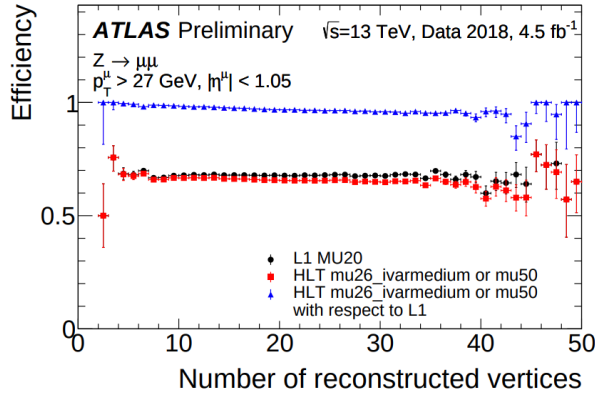


Figure 3.8: Muon trigger efficiency in the barrel region as a function of the number of reconstructed vertices. Efficiencies of L1, HLT and the total efficiency are shown for offline muons reconstructed in the barrel region with  $p_T > 27 \text{ GeV}$ .

leptons decay either leptonically:

$$\tau_{\text{lep}} \rightarrow l \nu_l \nu_\tau \quad (3.5)$$

with  $l = e, \mu$ , or hadronically:

$$\tau_{\text{had}} \rightarrow \text{had} \nu_\tau \quad (3.6)$$

The hadronic tau lepton decays represent 65% of all possible decay modes, therefore they are dominant.

The main background to hadronic tau lepton decays comes from jets of energetic hadrons, produced via the fragmentation of quarks and gluons. Both them are present

at trigger level (online level) as well as during the event reconstruction (offline level). Electrons also form an important background. The performance of online and offline tau identifications within the tau energy scale calibration are measured using a tag-and-probe method (see Section 3.2.2), applied to events enriched in the  $Z \rightarrow \tau\tau$  process, with one tau decaying into muon (tag) and the other one decaying into hadrons (probe). In order to extend the range of the  $p_T$  spectrum of tau candidates, the performance of the online tau identification algorithm is also measured using events enriched in the  $t\bar{t}$  process. Also this measurement uses a tag-and-probe method with a muon as a tag and an hadronic tau lepton decay as probe. At the end, the performance of the electron rejection algorithm is measured [47]. For what regard specific final-state objects:

- **Muons** are reconstructed by combining an inner detector track with a track from the MS and must lie within  $|\eta| < 2.5$ , with  $p_T > 10 \text{ GeV}$  for the  $Z \rightarrow ee$  analysis and  $p_T > 7 \text{ GeV}$  for all other analyses. Muon candidates have to pass the Loose muon identification requirement, which corresponds to 90% efficiency.
- **Electrons** are reconstructed by matching clustered energy deposits in the EMCAL to tracks reconstructed in the inner detector and are required to satisfy this constraints:  $p_T > 15 \text{ GeV}$  and  $|\eta| < 2.47$ . The electrons are identified using the signal and background probability density functions for several discriminating variables.
- **Jets** are reconstructed using and anti- $k_t$  algorithm, with a distance parameter  $R = 0.4$ .
- The **missing transverse momentum** is calculated from the vector sum of the transverse momenta of all reconstructed electrons, muons, tau and jets in the event, as well as a term for the remaining tracks.

For both muons and electrons, the scalar sum of the transverse momenta of tracks within a cone of  $p_T$ -dependent size  $\Delta R < \min(10 \text{ GeV}/p_T, 0.3)$  (centered on the lepton candidate track and excluding the lepton track) is required to be less than a  $p_T$ -dependent fraction of the lepton  $p_T$ . Other small sub-criteria are needed.

### 3.3.1 $\tau$ -identification and triggers

The **tau identification** uses *Boosted Decision Trees (BDTs)* methods. Three working points *Loose*, *Medium* and *Tight* are provided; they correspond to different tau identification efficiency values<sup>7</sup>. Efficiency for each working point is ensured to be not strongly dependent on pile-up conditions.

Tau triggers are defined at L1 in the EM and HADCAL, with a granularity of  $\Delta\eta \times \Delta\phi = 0.1 \times 0.1$ . A core region is made up of a set of  $2 \times 2$  trigger towers and a

---

<sup>7</sup>Efficiency is designed to be independent of  $p_T$ .

requirement is placed on the  $E_T$  sum of the two most energetic adjacent EM calorimeter towers. At HLT level, the energy is recalculated using clusters of calorimeter cells contained in a  $\Delta R = 0.2$  cone around the L1 tau direction. Also a minimum transverse energy requirement on the online tau candidate is placed. The HLT precision track and calorimeter information is used to calculate a number of pile-up corrected variables which are then input into an online tau BDT. Values of L1 and HLT online tau identification efficiencies for tau candidates identified by the offline Medium tau identification are shown in Figure 3.9.

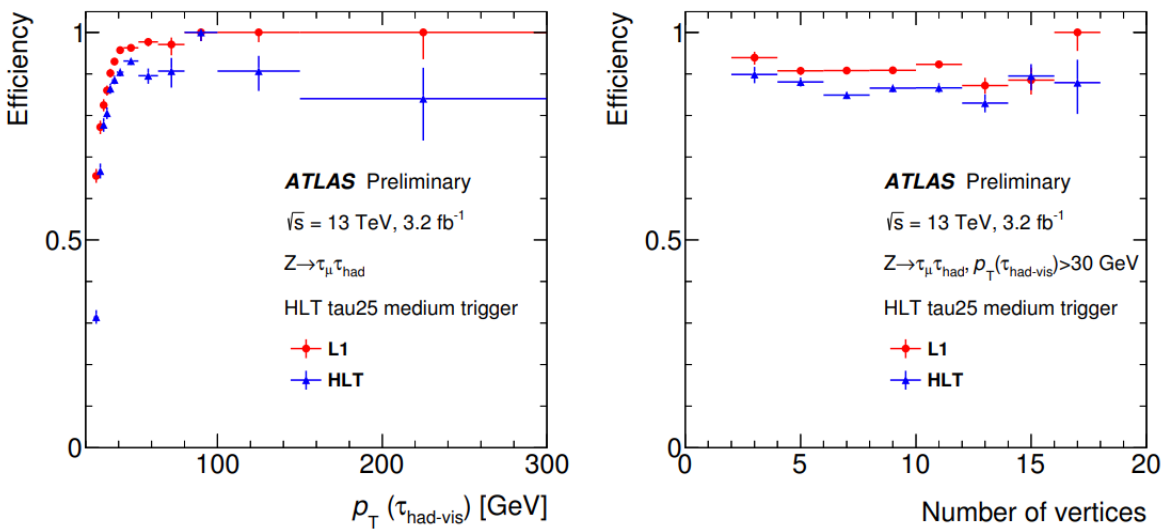


Figure 3.9: L1 (red dots) and HLT (blue triangles) online tau identification efficiency for tau candidates identified by the offline Medium tau identification, as a function of the offline  $p_T$  (left) and the number of primary vertices (right). Error bars correspond to statistical uncertainties.

### 3.4 Jet reconstruction and calibration

In ATLAS, different jets definitions are used, in particular for the study of QCD jets and jets containing the hadronic decay of boosted massive particles. These different kind of jets are calibrated through some sequential steps. Jets are only a representation of the underlying physical process: the use of different jet definitions is adopted regarding the considered phenomena [48]. ATLAS usually considers mostly small- $R$  jets for physics results with quarks and gluons. The resulting jet is calibrated, in order to provide an accurate representation of the event.

The jet reconstruction is mainly divided into three parts:

- **Jet inputs:** in ATLAS *topo-clusters* as the inputs to the jet reconstruction are primarily used. They are topologically-grouped noise-suppressed clusters of calorimeter cells. These clusters are formed from seed cells with more than  $4\sigma$  of energy<sup>8</sup>. Currently, the pile-up noise dominates. All cells adjacent to the seed cells, in three dimensions, are then grouped together, in a way to have at least  $2\sigma$  of energy. The latter process repeats until there are no such adjacent cells. Final step is the addition of all calorimeter cells adjacent to the topo-clusters, irrespective of their energy.
- **Jet algorithms:** ATLAS uses the *anti- $k_t$*  algorithm for jet reconstruction. Two different distance parameters  $R$  are typically used, corresponding to different intended uses. Jets representing quarks and gluons are called small- $R$  jets and are reconstructed with  $R = 0.4$ . Instead, jets representing hadronically decaying massive particles are typically called large- $R$  jets and are reconstructed with  $R = 1.0$ .
- **Jet grooming:** the usage of large- $R$  jets is necessary to fully contain the hadronic massive particle decays, but it comes with a substantially increased sensitivity to pile-up effects due to the larger fraction of the calorimeter enclosed within the jet volume. While pile-up may be low energy and thus not charge, the total jet kinematics by a large amount is randomly distributed and can thus unknown the angular structure within the jet that is the key to identifying massive particle decays. In order to solve this limitations, large- $R$  jets are typically groomed<sup>9</sup>.

The jet **calibration** procedure is divided into three steps: first, pile-up contributions are suppressed at the jet level, for small- $R$  jets, then the jet is calibrated to the MC truth scale and finally the differences between MC and data are considered.

### 3.4.1 *b*-tagging algorithms

The purpose of *b*-tagging algorithms is to identify jets containing *b*-flavored hadrons. For each selected jet, this algorithms provide *b*-weights, reflecting the probability that this jet originates from a *b*-quark.

The discrimination of *b*-quark jets from light quark jets is possible mainly thanks to the relatively long lifetime of *b*-flavored hadrons, resulting in a significant flight path length  $L$  of the order of some millimeter. This leads to measurable secondary vertices and impact parameters of the decay products. The transverse impact parameter  $d_0$  and the longitudinal component  $z_0$  are defined in Appendix C.1. Various *b*-tagging algorithms

---

<sup>8</sup> $\sigma$  is the average amount of noise expected in the cell in question. It is defined as the sum of the expected electronic and pile-up noise.

<sup>9</sup>*Grooming* is a class of algorithms that take a jet and throw away constituents following a defined strategy, rebuilding the final jet from the remaining constituents.

are used in ATLAS, based on these discriminating variables ( $L$ ,  $d_0$  and  $z_0$ ), on secondary vertex properties and on the presence of leptons within  $b$ -jets.

Each tagging algorithm defines a discriminant  $w$ , associated to the probability for a given jet to have been originated from a  $b$ -quark. For each tagging algorithm, different “working points”, corresponding to different threshold on the  $w$  variable, can be used.

The choice of the working point sets the tagging efficiencies for  $b$ -,  $c$ - and light quark jets [49]. For our analysis the *DL1 algorithm* with a working point of 60% efficiency with veto on 3rd  $b$ -tagged jets at 85% efficiency is used.

The DL1 algorithm is based on a *deep feed-forward neural network (NN)*. The DL1 NN has a multidimensional output corresponding to the probabilities for a jet to be a  $b$ -jet, a  $c$ -jet or a light-flavour jet.

Training with multiple output nodes offers additional flexibility when constructing the final output discriminant by combining the  $b$ -jet,  $c$ -jet and light-flavour jet probabilities. Since all flavours are treated equally during training, the trained network can be used for both  $b$ -jet and  $c$ -jet tagging. The final DL1  $b$ -tagging discriminant is defined as:

$$D_{\text{DL1}} = \ln \left( \frac{p_b}{f_c \cdot p_c + (1 - f_c) \cdot p_{\text{light}}} \right) \quad (3.7)$$

where  $p_b$ ,  $p_c$ ,  $p_{\text{light}}$  and  $f_c$  represent respectively the  $b$ -jet,  $c$ -jet and light-flavour jet probabilities, and the effective  $c$ -jet fraction in the background training sample. Using this approach, the  $c$ -jet fraction in the background can be chosen “a posteriori” in order to optimise the performance of the algorithm.

### 3.4.2 Jet triggers

The jet trigger menu consists of:

- **Single-jet triggers:** which require at least one jet above a given transverse energy threshold.
- **Multi-jet triggers:** which require at least  $N$  jets above a given transverse energy threshold.
- **$H_T$  triggers:** which require the scalar sum of the transverse energy of all jets in the event  $H_T$ , above a given threshold.
- **Analysis-specific triggers:** used for specific topologies of interest.

The jet triggers use at L1 either a random trigger or an L1 jet algorithm. The random trigger is used for triggers that select events with offline jet  $p_T < 45 \text{ GeV}$  to avoid bias due to inefficiencies of the L1 jet algorithm for low- $p_T$  jets.

*Jet trigger efficiencies* are determined using the *bootstrap method*<sup>10</sup> with respect to the  $p_T$  of the jet. In Figure 3.10 the single-jet trigger efficiencies for L1 and HLT are shown. Efficiencies plots for multi-jet and  $H_T$  triggers are shown in Appendix B.1.

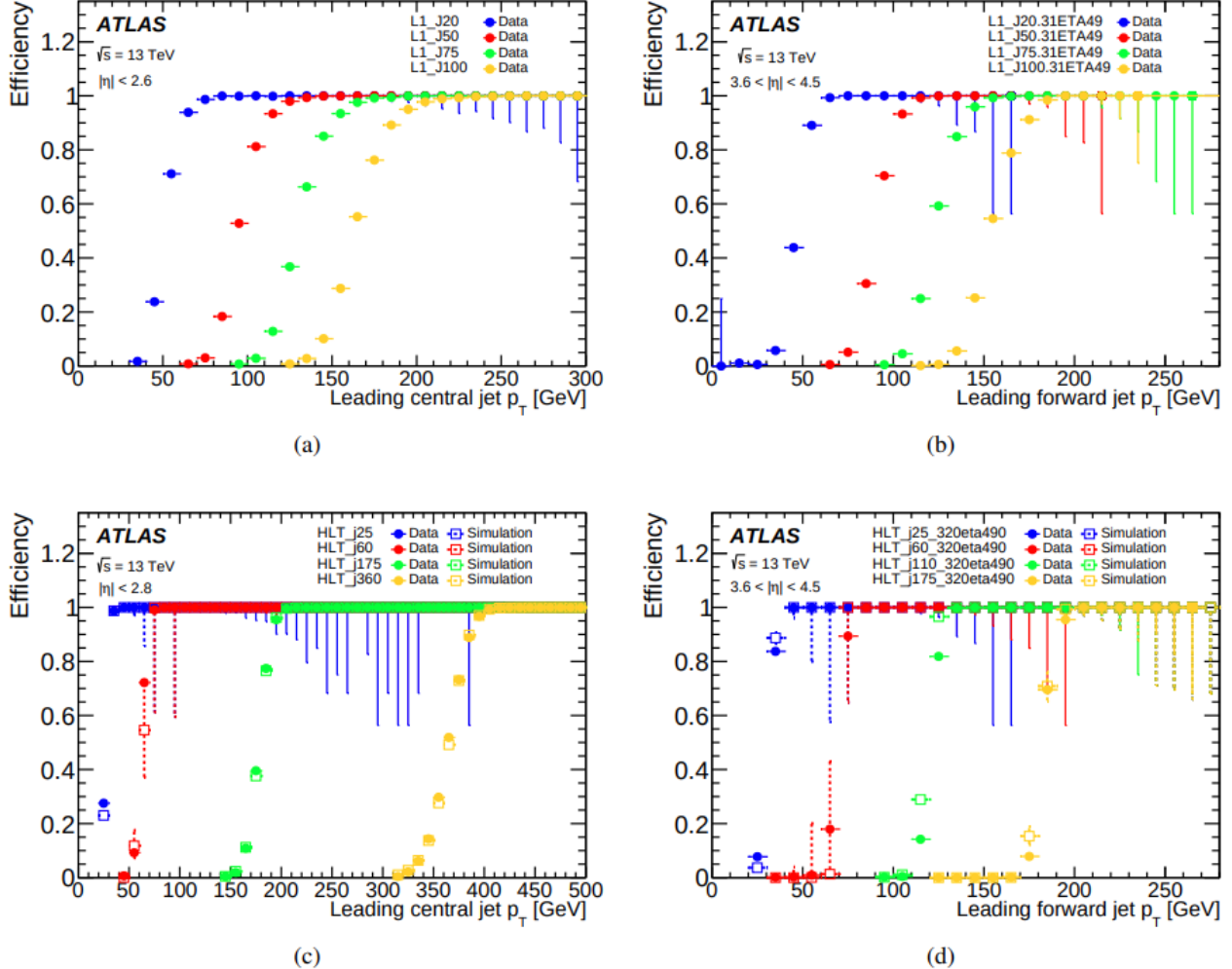


Figure 3.10: Single-jet trigger efficiencies for L1 and HLT for central and forward regions of the calorimeter, as a function of offline jet  $p_T$  for: (a) L1 in central region, (b) L1 in the forward region, (c) HLT in the central region and (d) HLT in the forward region.

<sup>10</sup>It gives relative efficiency from single jet triggers.

## 3.5 Missing Transverse Energy (MET) reconstruction

The missing transverse energy is reconstructed as the negative vector sum of transverse momenta  $p_T$  of reconstructed physics objects. The physical objects considered in the  $E_T^{\text{miss}}$  calculation are electrons, photons, muons,  $\tau$ -leptons and jets (**hard terms**) [50]. The  $E_T^{\text{miss}}$  components in the  $x - y$  transverse plane are:

$$E_{x(y)}^{\text{miss}} = E_{x(y)}^{\text{miss,e}} + E_{x(y)}^{\text{miss,}\mu} + E_{x(y)}^{\text{miss,}\gamma} + E_{x(y)}^{\text{miss,}\tau} + E_{x(y)}^{\text{miss,jets}} + E_{x(y)}^{\text{miss,soft}} \quad (3.8)$$

and each term is defined as:

$$E_{x(y)}^{\text{miss}} = - \sum_i^n p_{x(y)}(i) \quad (3.9)$$

where  $i$  are electron or muon or other interested objects. Instead, the reconstructed momentum not associated to any of the hard terms is referred as the **soft term**. There exist several algorithms used to reconstruct the  $E_T^{\text{miss}}$  soft term using calorimeter energy deposits or tracks. The main used algorithm for this purpose (used by ATLAS at Run-2) is the so-called *Tracks Soft Term* (TST), which fully relies on tracks. This algorithm misses the contribution from neutral particles, but it's robust against lots of pile-up conditions.

The removal of pile-up jets is essential for the  $E_T^{\text{miss}}$  resolution: this is done with the *Jet Vertex Tagger* (*JVT*) technique<sup>11</sup>. Also a *novel forward pileup tagging technique* (*fJVT*), that exploits the correlation between central and forward jets originating from pile-up interactions is developed. This latter technique improves the  $E_T^{\text{miss}}$  resolution in high pile-up conditions (see Figure 3.11). The TST systematic uncertainties are evaluated exploiting the differences between data and MC using the balance of a soft term and a calibrated physics object. The mean of the TST distribution as a function of the hard  $p_T$  term has been measured using  $36.5 \text{ fb}^{-1}$  Run-2 ATLAS data and agrees with MC simulation within the systematic uncertainty.

### 3.5.1 Missing Transverse Energy (MET) triggers

The  $E_T^{\text{miss}}$  trigger is used in searches where the final state contains only jets and large  $E_T^{\text{miss}}$ . This  $E_T^{\text{miss}}$  trigger can be the most efficient trigger for selecting final states containing highly energetic muons. The very large rate of hadronic jet production means that, even with reasonably good calorimeter resolution, jet energy measurement can lead into a very large  $E_T^{\text{miss}}$  trigger rate. Improvements in the L1  $E_T^{\text{miss}}$  determination have been important in maintaining the L1 performance. Different HLT algorithmic strategies based on cells, jets or topo-clusters are developed. This algorithms use only energy measurements in the calorimeter. Therefore, five different algorithms are used:

---

<sup>11</sup>This technique extracts the pile-up jets using track-to-vertex association method.

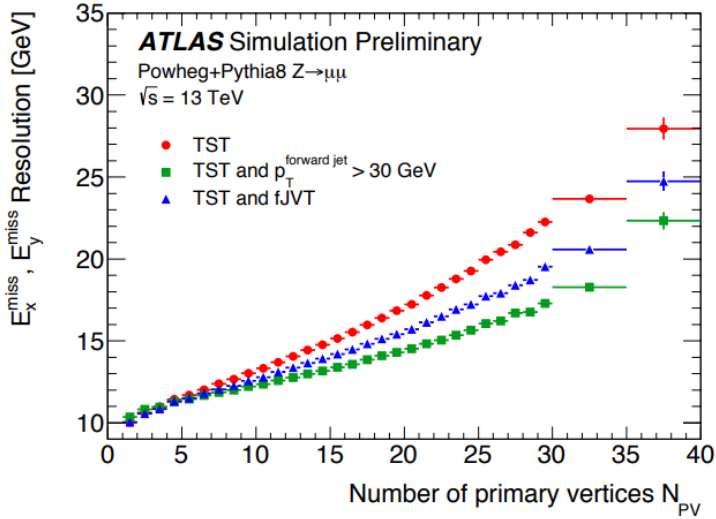


Figure 3.11: TST  $E_T^{\text{miss}}$  resolution as a function of the number of primary vertices, measured in MC simulated  $Z \rightarrow \mu\mu$  events using different strategies for pile-up suppression.

- **Cell algorithm (xe):** the measured energy in each LAr and Tile calorimeter cell and the position of the cell in the detector are used to obtain the components of the cell measured momentum in the massless approximation. Non-functioning calorimeter cells are masked out and do not contribute in the calculation. The total  $p_T^{\text{miss}}$ , given by:

$$p_T^{\text{miss}} = - \sum_i (p_{x,i}, p_{y,i}) \quad (3.10)$$

is found from the remaining contributing cells and the  $E_T^{\text{miss}}$  is calculated from its norm:  $E_T^{\text{miss}} = |p_T^{\text{miss}}|$ .

- **Jet-based algorithm (xe\_tc\_mht):** in this case the  $E_T^{\text{miss}}$  is calculated directly from the negative of the transverse momentum vector sum of all reconstructed jets.
- **Topo-cluster algorithm (xe\_tc\_lcw):** topo-clusters are built for the entire calorimeter and are used for the  $E_T^{\text{miss}}$  reconstruction. For each topo cluster, the momentum components are calculated in the approximation that particles contributing with energy to the cluster are massless and the  $p_T^{\text{miss}}$  is calculated from the negative vector sum of the components.
- **Pile-up suppression algorithm (xe\_tc\_pueta):** this algorithm is based on the topo-cluster  $E_T^{\text{miss}}$  algorithm described above, but includes a further pile-up sup-

pression method that is intended to limit the degradation of the  $E_T^{\text{miss}}$  resolution at very high pile-up.

- **Pile-up fit algorithm (xe\_tc\_pufit):** this starts again from the  $E_T^{\text{miss}}$  described above and a different pile-up suppression method is used.

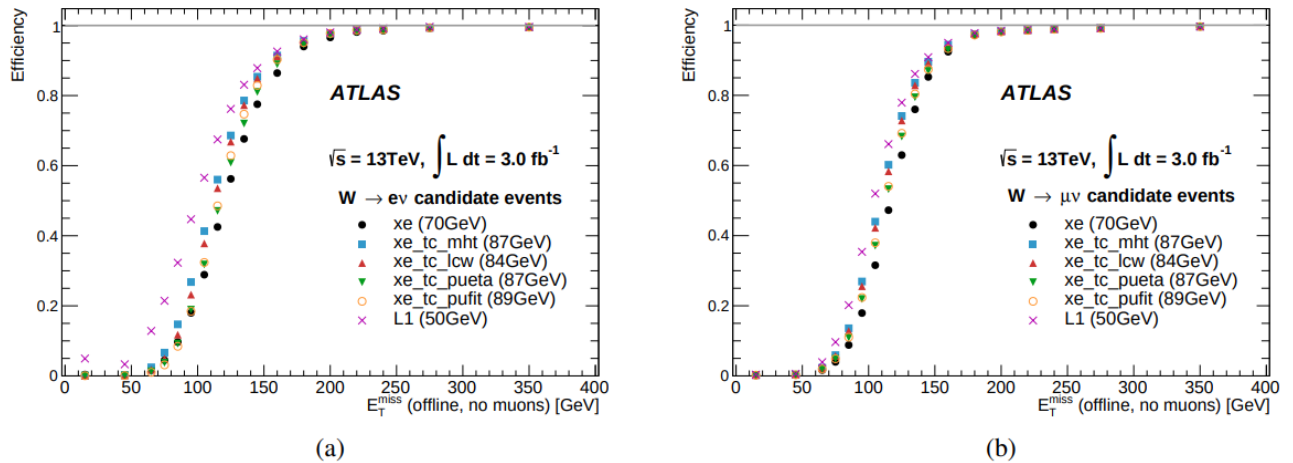


Figure 3.12:  $E_T^{\text{miss}}$  trigger efficiency curves with respect to the  $E_T^{\text{miss}}$  reconstructed offline without muon corrections for all events passing the (a)  $W \rightarrow e\nu$  or (b)  $W \rightarrow \mu\nu$  selections. Different efficiencies were measured for L1 and for combinations of L1 with each of the HLT  $E_T^{\text{miss}}$  algorithms.

Since  $E_T^{\text{miss}}$  is a global observable calculated from many contributions, each of them is taken into account with its own detector resolution. The efficiency curves of the various  $E_T^{\text{miss}}$  trigger algorithms for  $W \rightarrow e\nu$  and  $W \rightarrow \mu\nu$  selections are shown in Figure 3.12. For the selection exactly one lepton (electron or muon) with  $p_T > 25 \text{ GeV}$ ,  $m_T > 50 \text{ GeV}$  and a single lepton trigger: 24 GeV single-electron or 20 GeV single-muon are required.

## 3.6 Overlap removal

To avoid cases where detector response to a single physical object is reconstructed as two separate final-state objects, several steps are followed to remove these overlaps:

1. Calo-tagged muons sharing a track with an electron are removed, followed by the removal of any remaining electron sharing a track with a muon<sup>12</sup>.

<sup>12</sup>This step is useful to avoid cases where a muon mimics an electron through radiation of a hard photon.

2. The closest jet to each electron within an  $y - \phi$  cone of size  $\Delta R = 0.2$  is removed to reduce the proportion of electrons being reconstructed as jets. In particular, this jets must pass the JVT requirements (mentioned at the end of the Section 3.5), in addition to the standard  $p_T$  and  $|\eta|$  requirements, to be used to remove an overlapping object.
3. Electrons with a distance  $\Delta R < 0.4$  from any of the remaining non-pileup jets are removed to reduce backgrounds from non-prompt, non-isolated electrons coming from heavy-flavor hadron decays.
4. Jets with fewer than three tracks and distance  $\Delta R < 0.2$  from a muon are then removed to reduce jet fakes from muons depositing energy in the calorimeters.
5. Muons with a distance  $\Delta R < 0.4$  from any of the surviving jets are removed to avoid contamination of non-prompt muons from heavy flavor hadron decays.

# Chapter 4

## Differential cross-section measurement in the dilepton channel

The main focus of this analysis is the measurement of the differential  $WbWb$  production cross-section in the dilepton channel in proton-proton collisions, in order to study the quantum interference between singly and doubly resonant top quark production described in Section 1.3.3.

The cross-section has been measured in the fiducial phase-space as a function of two interference-sensitive variables at particle-level, that are  $m_{bl}^{\text{minimax}}$  and  $\Delta R(b_1, b_2)$ . In particular, the measurement has been performed for 1D  $m_{bl}^{\text{minimax}}$  and  $\Delta R(b_1, b_2)$  and for 2D  $m_{bl}^{\text{minimax}}$  in bins of  $\Delta R(b_1, b_2)$ .

In Appendix C.1 a preliminary study of the impact parameters of final-state lepton tracks is performed, in order to investigate possible differences in final-state leptons coming from the decay of a  $\tau$  or a  $W$  (this is not preparatory for my cross-section measurement). In Section 4.1 the data and MC samples used for the analysis are introduced. In Section 4.2 the event selections are presented, while in Section 4.4 the observables used to measure the differential cross-section are explained. Finally in Section 4.5 the analysis strategy is pointed out and in Section 4.6 all the systematic uncertainties are presented. Results are shown in Section 4.7.

### 4.1 Data and Monte Carlo samples

In this section the data and MC simulated samples used to describe the signal and background samples are introduced.

### 4.1.1 Data sample

For this measurement we used the full dataset collected by the ATLAS detector during Run-2 operations (2015-2018). This consists of data from proton-proton collisions at a center-of-mass energy of 13 TeV corresponding to a total integrated luminosity of  $139 \text{ fb}^{-1}$ .

Only the data collected during stable beam conditions and with the ATLAS detector fully functioning is included. The partial integrated luminosities for each year of operation, corresponding to each *Good Run List (GRL)*<sup>1</sup>, are respectively  $3.2 \text{ fb}^{-1}$ ,  $33 \text{ fb}^{-1}$ ,  $44 \text{ fb}^{-1}$  and  $59 \text{ fb}^{-1}$  for 2015, 2016, 2017 and 2018.

Events are considered only if they are accepted by at least one of the single-muon or single-electron triggers (see Sections 3.1.3 and 3.2.3). For each lepton type, multiple trigger conditions were combined to maintain good efficiency in the full momentum range, while controlling the trigger rate. Different transverse momentum ( $p_T$ ) thresholds were applied in the 2015 and 2016-2018 data taking. In the data sample collected in 2015, the  $p_T$  thresholds for the electrons were 24 GeV, 60 GeV and 120 GeV, while for muons 20 GeV and 50 GeV; in the data sample collected in 2016-2018, the  $p_T$  thresholds for the electrons were 26 GeV, 60 GeV and 140 GeV, while for muons they were set at 26 GeV and 50 GeV. Different  $p_T$  thresholds were employed since tighter isolation or identification requirements were applied to the triggers with lowest  $p_T$  thresholds.

### 4.1.2 Monte Carlo simulated samples

To account for all the processes that could lead to the final state studied in this measurement, MC simulated samples are taken into account in the analysis. The main MC generators used to model signal samples are:

- **$tW$  production:** it is modelled using the POWHEGBox v2 generator [51, 52, 53, 54] which provides matrix element at the NLO in  $\alpha_S$  in the 5-flavor scheme (see Section 1.3.2) with the NNPDF3.0NLO [55] for *Parton Distribution Function (PDF)* set. The renormalisation and factorisation scales are set to the top-quark mass:  $m_{top} = 172.5 \text{ GeV}$ . The DR scheme (see Section 1.3.3) is employed to treat the interference with  $t\bar{t}$  production. All the events are interfaced with PYTHIA8.230 [56] using the A14 tune [57] and the NNPDF2.3LO PDF set. Decays of bottom and charm quarks are simulated with the EVTGEN v1.6.0 event generator [58]. The inclusive cross-section is corrected to the theory prediction calculated at NLO in QCD with NNLL (Next-to-Next-Leading-Leading) soft-gluon corrections [59, 60]. The uncertainty on the cross-section due to PDF is calculated with the MSTW2008nnlo 90% CL (Confidence Level) [61, 62] PDF set and is added in quadrature to the scale uncertainty.

---

<sup>1</sup>GRLs contain the information where all the sub-detectors were in good data-taking conditions.

- **$t\bar{t}$  production:** it is modelled using the POWHEGBox v2 which provides, also in this case, matrix elements at NLO in  $\alpha_S$  with the NNPDF3.0NLO PDF. The  $h_{damp}$  parameter, that controls the matching of POWHEG and regulates the high- $p_T$  radiation against which the  $t\bar{t}$  recoils, is set to 1.5  $m_{top}$ . Dynamic renormalisation and factorisation scales are set to  $\sqrt{m_{top}^2 + p_T^2}$ . Events are interfaced with PYTHIA8.230 for the parton shower and hadronization, using the A14 tuned parameters and the NNPDF2.3LO PDF set. As in the previous case, the decays of bottom and charmed hadrons are simulated using the EvtGEN v1.6.0 event generator. The  $t\bar{t}$  sample is normalised similarly to the previous case, but now soft-gluon terms are used and calculated with TOP++2.0 program [63], which includes the NNLO QCD corrections and resums NNLL soft-gluon terms [64, 65, 66, 67, 68]. Uncertainties on the cross-section due to PDF and  $\alpha_S$  are calculated using the PDF4LHC prescription [69] with the MSTW2008 68% CL NNLO, CT10 NNLO [70] and NNPDF2.3 5F FFN [71, 72] PDF sets and are added in quadrature to the scale uncertainty.

MC generators used to generate the background samples are:

- **$Z+jets$  production:** it is simulated using the SHERPA v2.2.1 generator [73]. Matrix elements are matched and merged with the SHERPA PS based on Catani-Seymour dipole [74, 75] using the ME+PS@NLO prescription [76, 77, 78, 79]. The virtual QCD correction for matrix elements at NLO accuracy are simulated with the OPENLOOPS library [80, 81]. Samples are generated using the NNPDF2.3LO PDF set, with dedicated set of tuned parton-shower parameters. For this samples a cut-off  $m_{ll} > 40$  GeV was applied at generator level.
- **Diboson production ( $ZZ, WW, WZ$ ):** this production has been simulated with SHERPA 2.2.2 generator. In this setup multiple matrix elements are matched and merged with the SHERPA parton shower based on Catani-Seymour dipole using the MEPS@NLO prescription. The virtual QCD correction for matrix elements at NLO accuracy are provided by the OPENLOOPS library. Samples are generated using the NNPDF2.3LO PDF set, with dedicated set of tuned parton-shower parameters.
- **$t\bar{t}V$  production<sup>2</sup>:** it is modelled using MADGRAPH5\_AMC@NLO v2.3.3 generator [82] which provides matrix elements at NLO in  $\alpha_S$  with the NNPDF3.0LO PDF. The functional form of the renormalization and factorisation scales are set to  $0.5 \times \sum_i \sqrt{m_i^2 + p_{T,i}^2}$ <sup>3</sup>. Top quark decays are taken into account at LO, using MADSPIN [83] in order to preserve spin correlations. Events are interfaced with

---

<sup>2</sup> $V = W, Z$

<sup>3</sup>The sum runs over all the particles generated from the matrix element calculation.

PYTHIA8.210 for parton shower and hadronization, using, as in the previous cases, A14 tuned parameters and the NNPDF2.3LO PDF set. Decays of bottom and charm hadrons are simulated in the same ways as  $t\bar{t}$  and  $tW$ . Cross-sections are calculated at NLO QCD and NLO EW accuracy, using MADGRAPH5\_AMC@NLO. The  $t\bar{t}Z$  cross-section is further supplemented with an off-shell correction. Uncertainties are estimated from variations of the renormalization and factorization scales, as well as the strong coupling  $\alpha_S$ .

- **Non-prompt background:** it is purely estimated by MC by selecting events with non-prompt leptons, based on truth level information (from  $tW$ ,  $t\bar{t}$ ,  $Z + \text{jets}$ ,  $W + \text{jets}$ , diboson and  $t\bar{t}V$ ) and assuming all fakes come from modeled processes.

## 4.2 Event selection

In order to better characterize the interference effects, the most promising final states of the  $WbWb$  signal process are those which contain two well-reconstructed electrons and muons and have opposite-sign charge (OS). So the allowed channels are:  $ee$ ,  $e\mu$  and  $\mu\mu$  final states of:

$$pp \rightarrow WbWb \rightarrow l^+ \nu_l l^- \bar{\nu}_l b\bar{b}. \quad (4.1)$$

For this analysis we considered only the OS  $e\mu$  final-state for two reasons: firstly, this channel, among all the dileptonic final-states, allows to strongly suppress the  $Z \rightarrow ll$  background and secondly, because we expect the  $2b4l$  predictions be  $e\mu$  only. Additional required selection cuts are:

- $p_T$  of the lepton  $> 28 \text{ GeV}$ ;
- $p_T > 25 \text{ GeV}$  and  $|\eta| < 2.5$  for the jets;
- 2  $b$ -tagged jets at 60%WP with veto on 3rd  $b$ -tagged jets at 85%WP (see Section 3.4.1). These requirements allow to select very pure  $t\bar{t}/tWb$  samples thanks to the tight requirement on the 2  $b$ -tagged jets. The veto on the third jet, tagged with a looser requirement, helps in discarding events when an additional heavy-flavor jet is produced, which are poorly modelled.

No jet multiplicity restriction on the light jets are required.

Object reconstruction follows the procedure illustrated in Chapter 3: in particular, events have been selected if they fired a single-muon or a single-electron trigger.

The total number of events for each sample is shown in Table 4.1.

Sample	Total events
$t\bar{t}$	$264000 \pm 6000$
$tW$ (DR)	$8200 \pm 180$
$t\bar{t}V$	$734 \pm 3$
Fakes	$375 \pm 7$
Diboson	$44.8 \pm 0.9$
$Z + \text{jets}$	$2420 \pm 33$
Expected	$276000 \pm 6000$
Observed	278333

Table 4.1: Observed and expected number of events after the full event selection. The uncertainties for the  $t\bar{t}$  and  $tW$  samples include the uncertainties on the scale factors (see Section 4.6) and the MC statistics. The uncertainties for the background samples include only the MC statistics.

### 4.2.1 Control plots

Here, some detector-level variables control plots for events that pass the selection and that takes into account some uncertainties (of identification efficiency scale factor, reconstruction and lepton isolation scale factor,  $b$ -tagging, JVT and pileup) are shown in Figures 4.1, 4.2, 4.3 and 4.4.

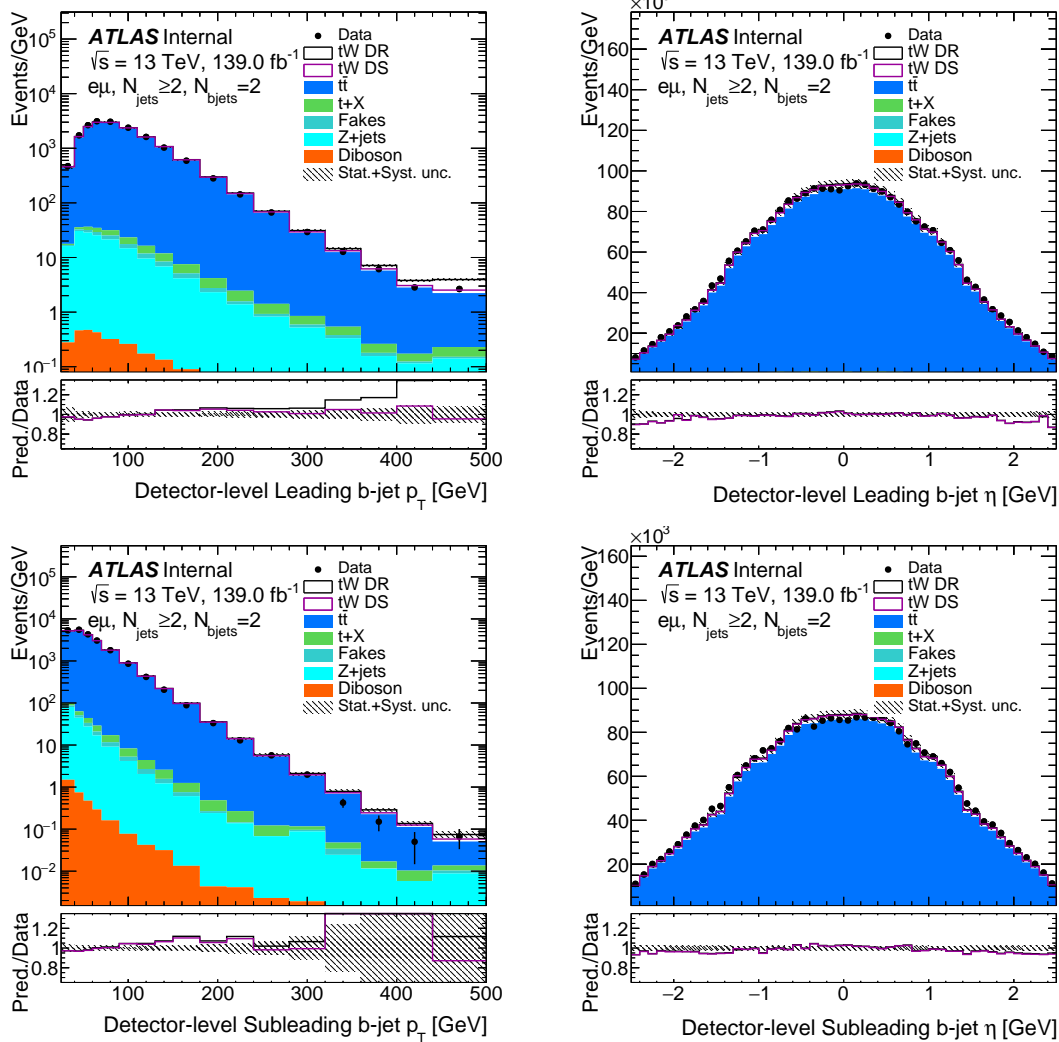


Figure 4.1: Kinematic distributions in the  $e\mu$  channel at detector-level: (upper left) leading  $b$ -jet  $p_T$  and (upper right) pseudorapidity and (lower left) subleading  $b$ -jet  $p_T$  and (lower right) pseudorapidity. Data distributions are compared with predictions using POWHEG + PYTHIA 8 as the  $t\bar{t}$  signal model and both POWHEG + PYTHIA 8 DR and DS for the  $tW$  signal model. The hatched area represents the combined statistical and systematic uncertainties (described in Section 4.6) in the total prediction, including only systematic uncertainties of the scale factors. Underflow and overflow events, if any, are included in the first and last bins. The lower panels show the ratio of the data to the total prediction obtained with both DR and DS schemes for the  $tW$  modelling.

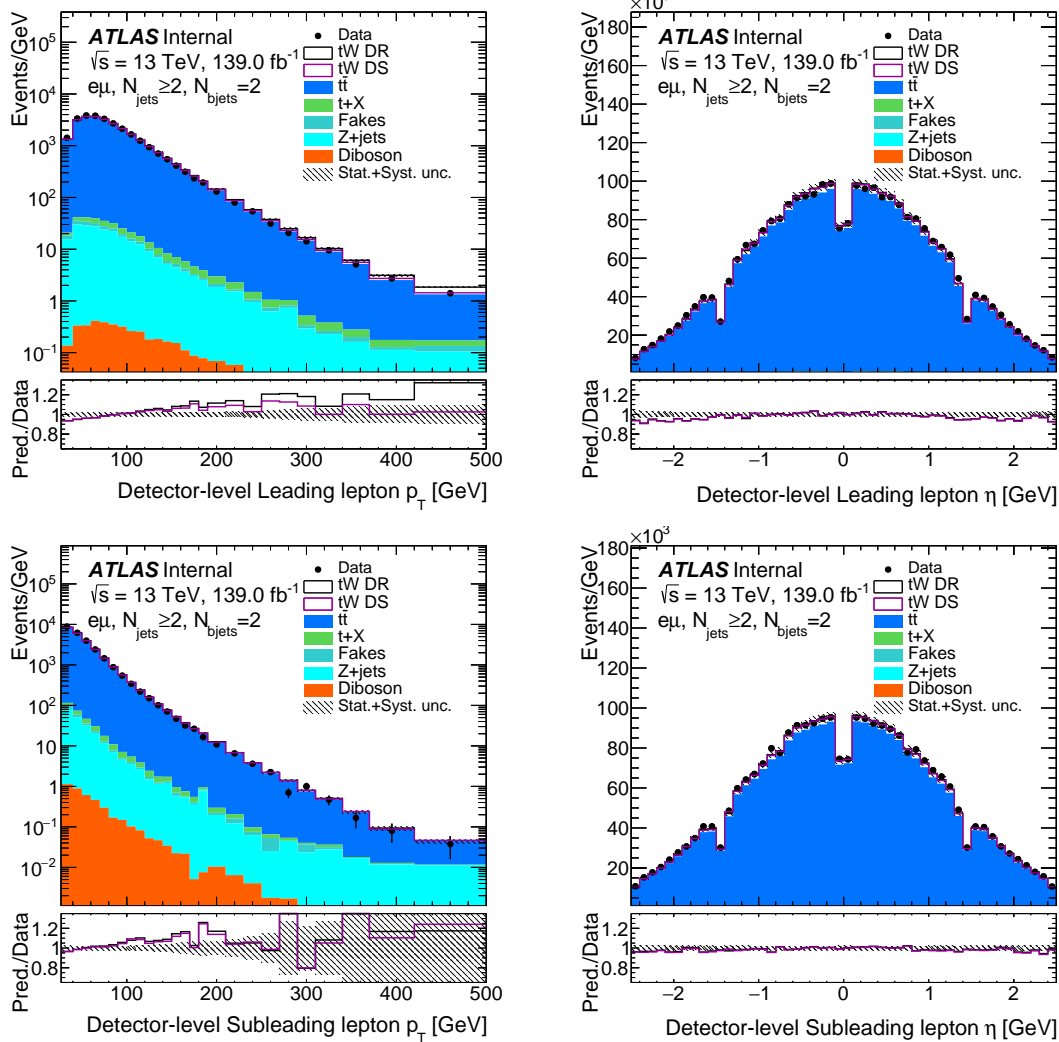


Figure 4.2: Kinematic distributions in the  $e\mu$  channel at detector-level: (upper left) leading lepton  $p_T$  and (upper right) pseudorapidity and (lower left) subleading lepton  $p_T$  and (lower right) pseudorapidity. Data distributions are compared with predictions using POWHEG + PYTHIA 8 as the  $t\bar{t}$  signal model and both POWHEG + PYTHIA 8 DR and DS for the  $tW$  signal model. The hatched area represents the combined statistical and systematic uncertainties (described in Section 4.6) in the total prediction, including only systematic uncertainties of the scale factors. Underflow and overflow events, if any, are included in the first and last bins. The lower panels show the ratio of the data to the total prediction obtained with both DR and DS schemes for the  $tW$  modelling.

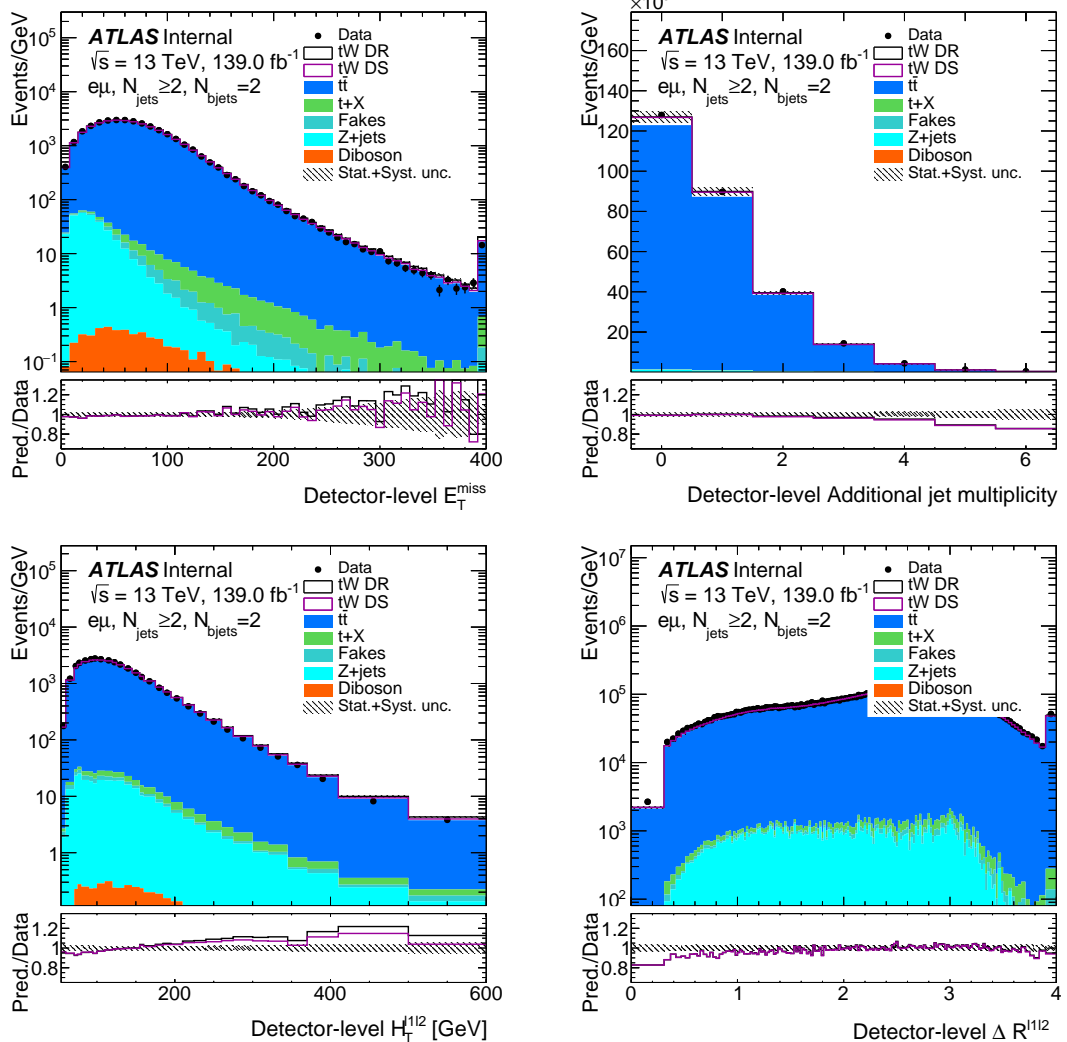


Figure 4.3: Kinematic distributions in the  $e\mu$  channel at detector-level: (upper left)  $E_T^{\text{miss}}$ , (upper right) number of extra jets, (lower left)  $H_{l_1 l_2}^T$  and (lower right)  $\Delta R_{l_1 l_2}$ . Data distributions are compared with predictions using POWHEG + PYTHIA 8 as the  $t\bar{t}$  signal model and both POWHEG + PYTHIA 8 DR and DS for the  $tW$  signal model. The hatched area represents the combined statistical and systematic uncertainties (described in Section 4.6) in the total prediction, including only systematic uncertainties of the scale factors. Underflow and overflow events, if any, are included in the first and last bins. The lower panels show the ratio of the data to the total prediction obtained with both DR and DS schemes for the  $tW$  modelling.

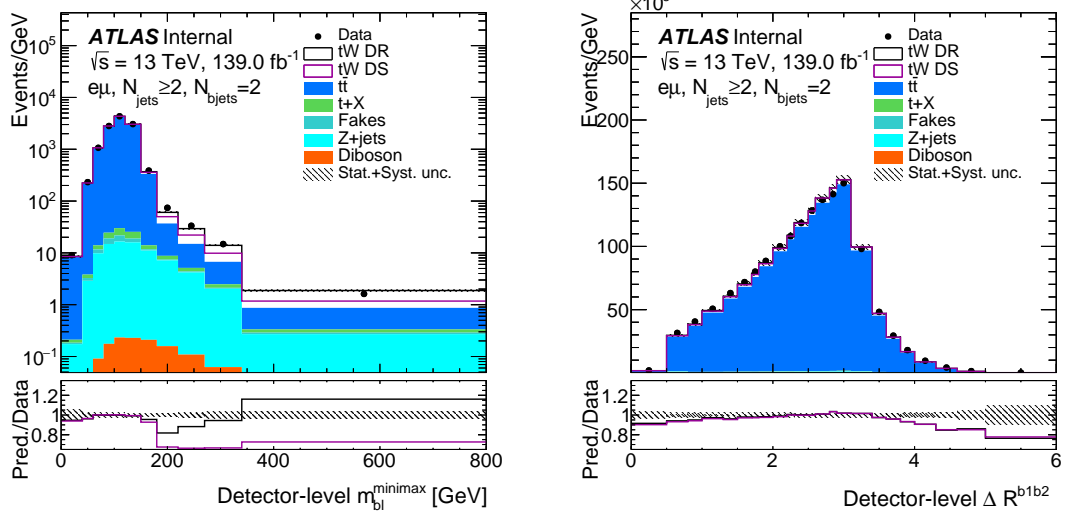


Figure 4.4: Kinematic distributions in the  $e\mu$  channel at detector-level: (left)  $m_{bl}^{\text{minimax}}$  and (right)  $\Delta R(b_1, b_2)$ . Data distributions are compared with predictions using POWHEG + PYTHIA 8 as the  $t\bar{t}$  signal model and both POWHEG + PYTHIA 8 DR and DS for the  $tW$  signal model. The hatched area represents the combined statistical and systematic uncertainties (described in Section 4.6) in the total prediction, including only systematic uncertainties of the scale factors. Underflow and overflow events, if any, are included in the first and last bins. The lower panels show the ratio of the data to the total prediction obtained with both DR and DS schemes for the  $tW$  modelling.

### 4.3 Particle-level objects

Particle-level objects are reconstructed using generator-level information from MC simulation. The physics objects are built from stable particles in the generator record, defined as those that satisfy:  $c\tau > 10 \text{ mm}$ .

Particle-level electrons and muons from the signal sample are selected from the stable particles and are required not to have been originated by an hadron, either directly or via an intermediate  $\tau$  decay. Their momentum is calculated to include the radiation loss due to *final-state radiation (FSR)* photons, classified as photons with  $\Delta R < 0.1$  that don't originate from hadron decays.  $p_T$  and  $\eta$  requirements are the same of the detector-level signal objects. Baseline leptons are defined with looser  $p_T$  requirements of 4 GeV (muons) and 5 GeV (electrons) for the overlap removal (see Section 3.6).

Particle-level jets are reconstructed by clustering truth particles (excluding those identified as baseline leptons or neutrinos from electroweak boson decays), with the anti- $k_t$  algorithm with radius parameter of  $R = 0.4$ . Baseline jets have to satisfy  $p_T > 20 \text{ GeV}$  and  $|\eta| < 2.8$ , while signal jets have to satisfy  $p_T > 25 \text{ GeV}$  and  $|\eta| < 2.5$ .

$B$ -hadrons are matched to jets by using the *ghost-association procedure* [84] in which

truth jet clustering is run as usual, except with the energy of all  $B$ -hadrons set to a negligible value. All the particle jets containing a constituent  $B$ -hadron  $b$ -tagged after this procedure.

An identical overlap removal procedure as the one illustrated in Section 3.6 is performed with the truth-level objects.

### 4.3.1 Particle-level selection

Using particle-level objects a fiducial region is defined, in order to replicate the detector-level selections as closely as possible.

Events are also required to contain exactly two  $b$ -jets, tagged with the  $B$ -hadron ghost-association matching.

This requirements define the **inclusive particle-level fiducial region**. The measured observables are unfolded to this phase space (see Section 4.5).

## 4.4 Studied observables

In this section the two observables used to measure the differential cross-section are: the  $m_{bl}^{\text{minimax}}$  and the  $\Delta R(b_1, b_2)$ .

### 4.4.1 The $m_{bl}^{\text{minimax}}$ variable

The  $m_{bl}^{\text{minimax}}$  variable has been already introduced in Section 1.3.5 and represents the invariant mass of a  $b$ -jet and a lepton. Let's assume that two leptons and  $b$ -jets are reconstructed in an event, labelling them  $b_1, b_2, l_1$  and  $l_2$ . Then one can create pairs to reconstruct four unique masses  $m_{ij} = m(b_i, l_j)$  where  $i, j = 1, 2$ . In doubly resonant  $t\bar{t}$  events, two of the masses are guaranteed to be below the top mass bound due to the not-reconstructed neutrino. But in singly-resonant  $t\bar{t}$  events, only a single pair must satisfy the top mass bound. The  $m_{bl}^{\text{minimax}}$  is constructed to efficiently take advantage of this difference (see Eq. 1.82).

There are two ways to match  $b$ -jets and leptons. Assuming that one has correctly paired the objects<sup>4</sup>, we are interested in the larger of the two masses, hence the **maximum**. This mass will be lower than the top mass bound for doubly-resonant events, while it can “evade the top mass endpoint” for singly-resonant  $tWb$  events. However, one cannot know a priori the correct way to make the  $b$ -jet-lepton pairing, so one is forced to take the **minimum** over the possible ways to assign the objects. An illustration of this procedure is shown in Figure 4.5. Thanks to this construction the  $t\bar{t}$  process mainly populates the region where  $m_{bl}^{\text{minimax}}$  is less than the top mass bound. Single top events populated the entirety of the  $m_{bl}^{\text{minimax}}$  distribution including the region where the

---

<sup>4</sup>So as to correctly group the decay products originating from the same top quark.

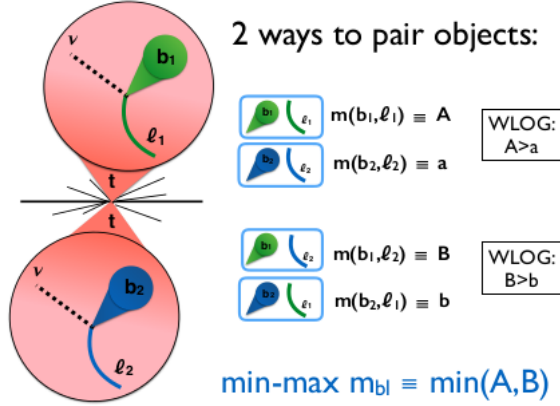


Figure 4.5: A scheme demonstrating the assignment of the leptons and  $b$ -jets to form the  $m_{bl}^{\text{minimax}}$  variable. Two possible pairings are considered: the **A-type** and the **B-type** and for each of them one can build two possible  $m_{bl}$  values. The minimum of the larger  $m_{bl}$  values from each pairing is selected as  $m_{bl}^{\text{minimax}}$ . In  $t\bar{t}$  events this choice has a kinematic endpoint at  $m_{bl}^{\text{minimax}} < \sqrt{m_t^2 - m_W^2}$  while for single-top events there is no such bound.

variable is significantly beyond the top mass. The interference effect is most significant when the objects have high- $p_T$  (see Figure 1.23). As a result of this effect, the region of large  $m_{bl}^{\text{minimax}}$  is highly pure in single top events and is very sensitive to the interference sensitive effect. At present, this is considered as the most interference-sensitive variable.

#### 4.4.2 The $\Delta R(b_1, b_2)$

The other considered observable is the  $\Delta R(b_1, b_2)$ <sup>5</sup>. It has been already introduced in Section 1.3.4 and represents the angular distance between two  $b$ -jets. The particular choice of the  $\Delta R(b_1, b_2)$  variable is inspired by the studies performed in the search for top squarks in the lepton-jets channel (see Section 1.3.4) where it is used to separate  $Wt$  from  $t\bar{t}$  contributions.

### 4.5 Analysis strategy

The goal of this analysis is to measure differential cross-sections of the inclusive  $WbWb$  process at the particle level. Single- and double-differential cross-sections have been measured as a function of the two observables described in Section 4.4.

---

<sup>5</sup>Also indicated with  $\Delta R_{b_1 b_2}$ .

In Section 4.5.1 the unfolding procedure is introduced. In Section 4.5.2 some resolution studies and binning choices for unfolding are investigated. In Section 4.5.3 closure tests are performed, in order to validate the stability of the chosen bins.

### 4.5.1 Unfolding procedure

A common problem in particle physics is the distortion of physical observables measurements due to the finite resolution and limited geometrical acceptance of the physical observables. Therefore the reconstructed distributions of physical quantities cannot be compared to theoretical distributions, or among different experiments. Data need to be corrected for these effects using the so-called **unfolding** procedure.

The purpose of this method is to return a distribution  $f(x)$  of a physical quantity  $x$ , starting from the experimental measurement  $y$  with its distribution  $g(y)$ , that is different with respect to the *true distribution*, because of detector effects.

It is possible to classify detector effects in two categories:

- **Limited acceptance effect:** it means that not all the events are used in the measurement of the physical quantity we are interested in, because of geometrical acceptance and trigger selection efficiency.
- **Limited resolution effect:** it means that it is impossible to measure any physical quantity with an infinite amount of accuracy. The true value of an observable "migrates" in another piece of the observed distribution.

Therefore,  $y$  will be different from  $x$ , and the  $g(y)$  distribution will be "smeared" with respect to  $f(x)$ . The relation that links  $f(x)$  and  $g(x)$  is given by:

$$g(y) = \int A(y, x) f(x) dx \quad (4.2)$$

where  $A(y, x)$  is the *smearing function* and describes the detector effects on the measurement.<sup>6</sup> MC simulations can be used to estimate  $A(y, x)$  and allow to evaluate detector effects on  $f(x)$  using Eq. 4.2.

Basically, the unfolding procedure tries to infer the true distribution starting from the reconstructed one. To solve this problem it is better to use binned values of  $x$  and  $y$  and represent  $f(x)$  and  $g(y)$  as histograms.

The unfolding equation can be described as follows:

$$\vec{g} = \mathbf{R} \vec{f} \quad (4.3)$$

---

<sup>6</sup>It describes the probability to reconstruct a true  $x$  value as  $y$ .

where  $\mathbf{R}$  is a  $m \times n$  matrix, called **response matrix** that contains the acceptance and smearing informations of the reconstruction process<sup>7</sup>,  $\vec{f}$  is an  $n$ -dimensional vector, called *true spectrum* and  $\vec{g}$  is an  $m$ -dimensional vector, called *reconstructed spectrum*.

Starting from the response matrix, it is possible to construct another matrix, called **migration matrix**. It is obtained through this relation:

$$M_{ij} = \frac{1}{A_j} R_{ij} \quad (4.4)$$

where  $A_j$  is the reconstruction efficiency in the true bin  $j$ . This matrix represents the probability that an event generated and selected in bin  $j$  is reconstructed in bin  $i$ . Usually, this matrix is constructed in a way that columns elements are normalized to unity in a way that, once the acceptance is accounted for, the probability to reconstruct an event in any bin is 1 [49].

If we would have infinite resolution and therefore no migrations (ideal situation), the response matrix would be diagonal with the elements representing the reconstruction efficiency of the  $x$  quantity in the  $j$ -th bin<sup>8</sup>. In this ideal case, the unfolded spectrum could be extracted from the reconstructed one, by simply dividing each bin in the reconstructed spectrum by the reconstructed efficiency.

For this analysis we used a particular unfolding approach, called **iterative Bayesian** unfolding. This unfolding procedure can be described as a “cause and effect” model, based on the Bayes theorem [85, 86].

If we suppose to have, for the studied variables,  $n$  reconstructed bins and  $m$  truth bins, we can define the “effect”  $E_i$  as the  $n_j$  events in the reconstructed bin  $j$ , while the “cause”  $C_i$  as the  $n_i$  events in the truth bin  $i$ . The effect is measured, but the cause is impossible to identify, so it needs to be estimated. We define the probability for an effect to come from a particular cause as  $P(E_j|C_i)$  and can be estimated by assuming some information of the migration matrix and a measurement efficiency and resolution calculated from MC.

This procedure can be performed by using a standard Bayesian inference analysis [87]. The probability of a cause, given a particular effect, is given by the Bayes theorem:

$$P(C_i|E_j) = \frac{P(E_j|C_i) \cdot P_0(C_i)}{\sum_{l=1}^{n_C} P(E_j|C_l) \cdot P_0(C_l)} \quad (4.5)$$

and the number of expected events in the  $i$ -th cause bin is:

$$\hat{n}(C_i) = \frac{1}{\epsilon_i} \sum_{j=1}^{n_E} P(C_i|E_j) n(E_j) \quad (4.6)$$

---

<sup>7</sup>The  $R$ -matrix is generally not diagonal, due to the fact that some events generated in bin  $j$  could be reconstructed in bin  $i \neq j$ . This phenomena is called *bin migration*.

<sup>8</sup>In this case the migration matrix would be the identity matrix.

where  $n(E_j)$  is the number of events in the effect bin  $j$ ,  $P_0(C_i)$  is the a priori probability (prior) of the cause  $C_i$  (usually taken from the MC simulation) and  $\epsilon_i$  is the efficiency of the selection in the bin  $i$ .

The population in the cause bins can be written in terms of the *unfold matrix*, defined as:

$$\hat{n}(C_i) = \sum_{j=1}^{n_E} \mathcal{M}_{ij}^{-1} n(E_j). \quad (4.7)$$

Here, the  $\mathcal{M}_{ij}^{-1}$  it is defined as:

$$\mathcal{M}_{ij}^{-1} = \frac{P(E_j|C_i) \cdot P_0(C_i)}{\sum_{l=1}^{n_E} P(E_l|C_i) \sum_{l=1}^{n_C} P(E_j|C_l) \cdot P_0(C_l)} \quad (4.8)$$

that is different from the inverse of  $M_{ij}$ .

Instead, the posterior probability of each cause  $C_i$  is evaluated as:

$$\hat{P}(C_i) = \frac{\hat{n}(C_i)}{\sum_j \hat{n}(C_j)} \quad (4.9)$$

To get the solution, this Bayesian method needs to be used iteratively, finally doing a polynomial fit of the posterior solution and using it as the prior for the next iteration. Each of this iteration will give an improved estimation of the actual distribution, until the algorithm reached a certain stability where each new result does not differ significantly from the previous one.

This unfolding procedure is implemented in the analysis by using the package ROOUNFOLD [88, 89].

For the unfolding we also need to define the following variables:

- $\vec{b}$ : the expected background events distribution with  $n$  bins.
- $f_{\text{acc}}^i = \frac{N_{\text{reco}\wedge\text{part}}^i}{N_{\text{reco}}^i}$  *acceptance factors*: for each bin of the reconstructed distribution, which corrects for reconstructed-level events which did not fall into the fiducial region defined at particle-level and thus have no associated particle-value which can be used during the unfolding. Therefore, it is defined as the fraction of signal events reconstructed in this bin that also pass the particle-level selection. The bin  $i$  here is defined by the *reconstructed-level* value of the variable.
- $\epsilon^i = \frac{N_{\text{part}\wedge\text{reco}}^i}{N_{\text{part}}^i}$  *inefficiency factors*: for each bin of the unfolded distribution, which account for efficiency and acceptance losses on going from truth to reco. The bin  $i$  here is defined by the *truth-level* value of the variable.

For our analysis, the unfolding procedure acts as follows: for each observable (see Section 4.4), the procedure starts from the number of events observed in data at reconstruction level in bin  $j$  of the distribution ( $N_{\text{reco}}^j$ ), from which the background contribution  $N_{\text{bkg}}^j$  is subtracted. Then the acceptance, migration and efficiency corrections are applied. All corrections are evaluated using the MC simulation of the signal sample.

The first step is the application of the acceptance correction  $f_{\text{acc}}^j$ . The resulting distribution is then unfolded to the particle level. The unfolding procedure uses as input the migration matrix derived from the simulated signal sample which maps the particle-level bin  $i$  in which an event falls to the bin  $j$  in which it is reconstructed. The probability for particle-level events to be reconstructed in the same bin is represented by the elements on the diagonal, and the off-diagonal elements represent the fraction of particle-level events that migrate into other bins. Therefore, the elements of each row sum to unity. For each observable, the number of bins is optimised such that the fraction of events in the diagonal bins is always greater than 50%. Validation of the unfolding procedure with the optimised binning is performed by requiring that closure (see Section 4.5.3) tests are satisfied without introducing any bias.

The last step is the application of the efficiency correction factor  $\epsilon$  to the unfolded spectrum, correcting the result with a bin-by-bin factor into the fiducial phase-space.

An important application of the unfolding method is the measurement of the differential cross-section  $d\sigma$  of a process. The differential cross-section of interest is a function of a kinematic variable  $X$  (see Section 4.4) and the procedure to measure it can be summarized as follows:

$$\frac{d\sigma^{\text{fid}}}{dX^i} \equiv \frac{1}{\mathcal{L} \cdot \Delta X^i} \cdot \frac{1}{\epsilon^i} \cdot \sum_j M^{-1} \cdot f_{\text{acc}}^j \cdot (N_{\text{obs}}^j - N_{\text{bkg}}^j), \quad (4.10)$$

where the index  $j$  runs over bins of observable  $X$  at reconstruction level while the index  $i$  labels bins at particle level,  $\Delta X^i$  is the bin width,  $\mathcal{L}$  is the integrated luminosity, and the inverted migration matrix as obtained with the iterative unfolding procedure is symbolised by  $M^{-1}$  [90]. The integrated fiducial cross-section  $\sigma^{\text{fid}}$  is obtained by integrating the differential cross-section over the bins, and its value is used to compute the normalised differential cross-sections:

$$\frac{1}{\sigma^{\text{fid}}} \cdot \frac{d\sigma^{\text{fid}}}{dX^i}. \quad (4.11)$$

### 4.5.2 Binning choice and resolution studies

The goal of the **resolution studies** is to have a bin width as fine as possible constrained by resolution on one side and the statistical uncertainty on the other. In the ideal case of a Gaussian resolution, choosing a bin width equal to  $2 \cdot \text{RMS}$  (*Root Mean Square*) deviation leads to have  $\approx 68\%$  of the reconstructed events in the correct bin.

The procedure is different for 1D and 2D distributions optimization. If we consider the **1D Binning**, the procedure is described as follows:

1. Iterative procedure starting for a fine binned distribution of  $T - R$  vs.  $T$ , where  $T$  is the true value of the observable and  $R$  is the reconstructed value.
2. Define the resolution as:

$$2 \cdot \text{RMS} \cdot (T - R) \quad (4.12)$$

in each bin of  $T$ .

3. Starting from the first bin, merge bins until:

$$\Delta_i > \delta \cdot 2 \cdot \text{RMS}_i \quad (4.13)$$

$$\sigma_{\text{stat}} \simeq \frac{\sqrt{N_i}}{N_i} < k\% \quad (4.14)$$

where  $\Delta_i$  is the bin width,  $\delta$  is a conservative factor and  $k\%$  is the upper limit for statistical uncertainty.

For the **2D binning** the 2D distributions require separate optimization for  $X$  and  $Y$  variables.

We tested both  $m_{bl}^{\text{minimax}}$  in bins of  $\Delta R(b_1, b_2)$  and viceversa. When talking about a variable  $X$  in bins of  $Y$ , we call  $X$  *internal variable* and  $Y$  *external variable*. Since  $m_{bl}^{\text{minimax}}$  rapidly falls above 170 GeV, it is difficult to achieve a high number of bins above the threshold when  $m_{bl}^{\text{minimax}}$  is an external variable.

In order to avoid significant migrations among regions of the variable  $Y$ , and to ensure that there is enough statistics in each region of the variable  $Y$  to allow a reasonable number of bins of the variable  $X$ , the procedure has been the one of defining a binning of  $Y$  with strong requirements and a binning of  $X$ , individually in each bin of  $Y$ , with the same procedure (see procedure adopted for the 1D distributions).

Requirements and chosen bins for 1D and 2D external variables are shown in Table 4.2, while requirements for 2D internal  $m_{bl}^{\text{minimax}}$  in bins of  $\Delta R(b_1, b_2)$  variable are shown in Tables 4.3. The requirement  $\sigma_{\text{stat}} < 0.5\%$  leads to a limited number of bins in the case of  $\Delta R(b_1, b_2)$  as external variable, but allows for a high number of bins for the internal variable, while for  $m_{bl}^{\text{minimax}}$ ,  $\sigma_{\text{stat}} < 2\%$  leads to 2 bins above 172 GeV.

Closure tests highlighted some statistical instabilities when unfolding  $\Delta R(b_1, b_2)$  in bins of  $m_{bl}^{\text{minimax}}$ , therefore we decided not to measure the cross-section for this variable (see more information in Section 4.5.3 and Appendix C.3).

Resolution plots, showing the RMS and mean of  $T - R$ , for the  $m_{bl}^{\text{minimax}}$  in bins of  $\Delta R(b_1, b_2)$  are presented in Figures 4.6 for the  $t\bar{t} + Wt$  DR sample, and in Figure 4.7 for the  $t\bar{t} + Wt$  DS. These plots are not centered in 0 because the distributions are not symmetric and therefore the expectation value is not centered in 0 (but it is always

Variable	Type	$\delta$	$k$	Bin edges
$m_{bl}^{\text{minimax}}$ [GeV]	1D	1	5%	0, 40, 60, 80, 100, 120, 150, 180, 220, 270, 340, 420, 580, 800
$\Delta R_{b_1 b_2}$	1D	1	5%	0, 0.5, 0.8, 1, 1.3, 1.5, 1.7, 1.8, 2, 2.2, 2.3, 2.5, 2.6, 2.8, 2.9, 3.1, 3.4, 3.6, 3.8, 4, 4.3, 4.6, 5, 6
$m_{bl}^{\text{minimax}}$ [GeV]	2D external	1	2%	0, 60, 90, 120, 160, 215, 800
$\Delta R_{b_1 b_2}$	2D external	1	0.5%	0, 1.5, 2, 2.4, 2.8, 3, 3.4, 6

Table 4.2: Requirements for binning and chosen bins for  $m_{bl}^{\text{minimax}}$  and  $\Delta R_{b_1 b_2}$  in the case of 1D and 2D external variables. For  $\Delta R_{b_1 b_2}$  the  $\delta$  value is basically irrelevant since we are dominated by statistics.

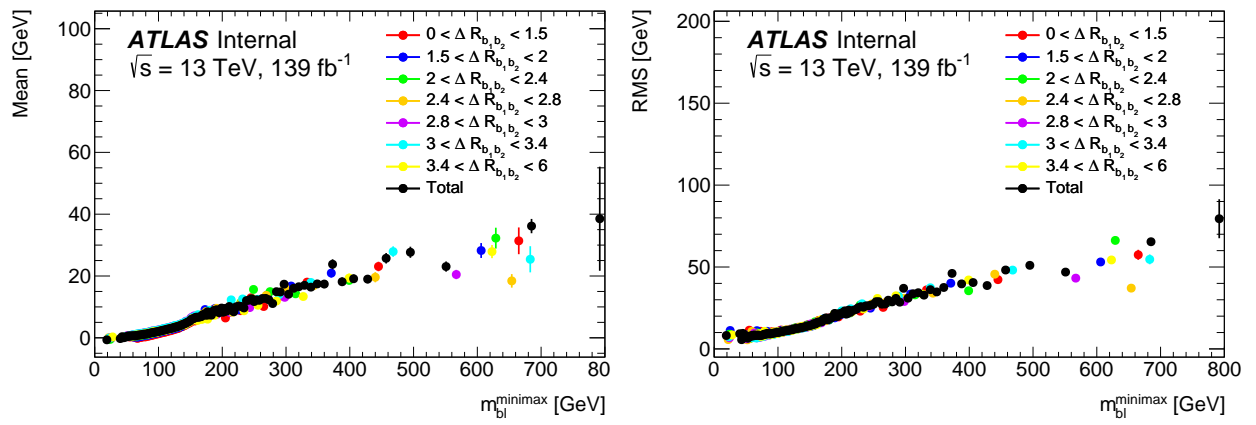


Figure 4.6: Mean and RMS of the resolution distributions for  $m_{bl}^{\text{minimax}}$  as a function of the particle-level  $m_{bl}^{\text{minimax}}$  in bins of  $\Delta R(b_1, b_2)$  in the DR scheme.

Variable	Type	$\delta$	$k$	Bin edges
$m_{bl}^{\text{minimax}}$ in $\Delta R_{b_1 b_2}$ (0, 1.5)	2D internal	2	5	0, 60, 110, 800
$m_{bl}^{\text{minimax}}$ in $\Delta R_{b_1 b_2}$ (1.5, 2)	2D internal	2	5	0, 60, 100, 150, 220, 800
$m_{bl}^{\text{minimax}}$ in $\Delta R_{b_1 b_2}$ (2, 2.4)	2D internal	2	5	0, 100, 140, 210, 800
$m_{bl}^{\text{minimax}}$ in $\Delta R_{b_1 b_2}$ (2.4, 2.8)	2D internal	2	5	0, 90, 140, 200, 800
$m_{bl}^{\text{minimax}}$ in $\Delta R_{b_1 b_2}$ (2.8, 3)	2D internal	2	5	0, 60, 100, 140, 200, 800
$m_{bl}^{\text{minimax}}$ in $\Delta R_{b_1 b_2}$ (3, 3.4)	2D internal	2	5	0, 90, 140, 800
$m_{bl}^{\text{minimax}}$ in $\Delta R_{b_1 b_2}$ (3.4 6)	2D internal	2	5	0, 70, 110, 160, 800

Table 4.3: Requirements for binning and chosen bins for  $m_{bl}^{\text{minimax}}$  in bins of  $\Delta R_{b_1 b_2}$  in the case of 2D internal variables.

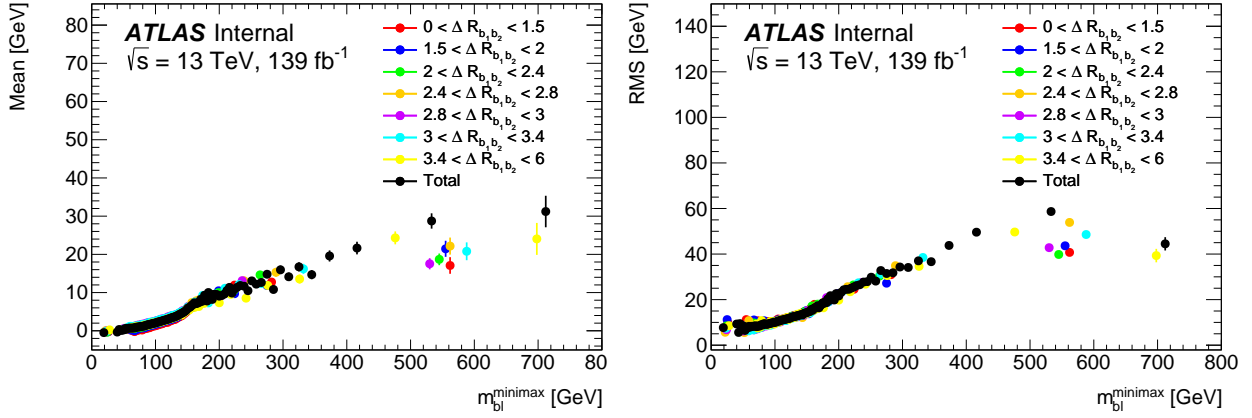


Figure 4.7: Mean and RMS of the resolution distributions for  $m_{bl}^{\text{minimax}}$  as a function of the particle-level  $m_{bl}^{\text{minimax}}$  in bins of  $\Delta R(b_1, b_2)$  in the DS scheme.

included within the final bin). Resolution plots for the  $t\bar{t}$  and  $tW$  samples are shown separately in Appendix C.2.1. Other additional informations about  $\Delta R(b_1, b_2)$  in bins of  $m_{bl}^{\text{minimax}}$  as a 2D internal variable can be found in Appendix C.2.2.

#### 4.5.3 Closure tests

In order to ensure the stability of the chosen bins and of the unfolding method, **closure** tests are necessary to make sure that no bias is introduced and any distortion possibly introduced by the unfolding procedure is negligible.

The  $t\bar{t} + Wt$  signal sample is used to perform the closure tests. In this kind of tests, a reconstructed-level distribution generated with a given model  $A$  is unfolded using corrections derived from an independent sample with the same model, and then compared to a truth-level distribution obtained using the same model [91]. Ideally, one should recover the original distribution. However, the limited statistics and the choice of regularization method usually have an effect on the unfolding results.

In order to perform these tests, the signal sample is split into two statistically-independent sub-samples (`half0` and `half1`), constructed by randomly assigning each event of the signal sample to one of the two sub-samples. The `half0` sub-sample is used as pseudo-data, while the `half1` sample is considered as MC signal and it is used for the evaluation of the unfolding corrections.

The first step of the closure tests consists on unfolding the pseudo-data sample by applying the corrections obtained with the MC signal sample. Then the unfolded pseudo-data are compared to the corresponding particle-level spectra. Finally, the compatibility of the unfolded pseudo-data and its corresponding particle-level spectrum is evaluated

using a  $\chi^2$ . For the  $\chi^2$  calculation the covariance matrix is built using both the statistical covariance matrix given by the unfolded pseudo-data and the covariance matrix given by the MC sample used for the corrections in the unfolding procedure. Closure tests are defined successful if a  $p$ -values greater than 0.05.

In Figure 4.8 1D closure tests for the particle-level normalized differential cross-section as a function of  $m_{bl}^{\text{minimax}}$  and  $\Delta R(b_1, b_2)$  are presented. In Figure 4.9, on the left, 2D closure test for the particle-level normalized differential cross-section as a function of the particle-level  $m_{bl}^{\text{minimax}}$  in bins of  $\Delta R(b_1, b_2)$  is shown; on the right, the ratio plot of the measured cross-section to different MC predictions is shown. From this latter ratio plot it is possible to see that each bin of  $\Delta R(b_1, b_2)$  is stable and therefore it is possible to consider this 2D variable for the unfolding. 2D closure tests of the particle-level normalized differential cross-section as a function of the  $\Delta R(b_1, b_2)$  in bins of  $m_{bl}^{\text{minimax}}$  are explained in Appendix C.3; they are not shown in this Section because, as mentioned in Section 4.5.2, the  $\Delta R(b_1, b_2)$  in bins of  $m_{bl}^{\text{minimax}}$  variable has been discarded due to the instability of the chosen bins.

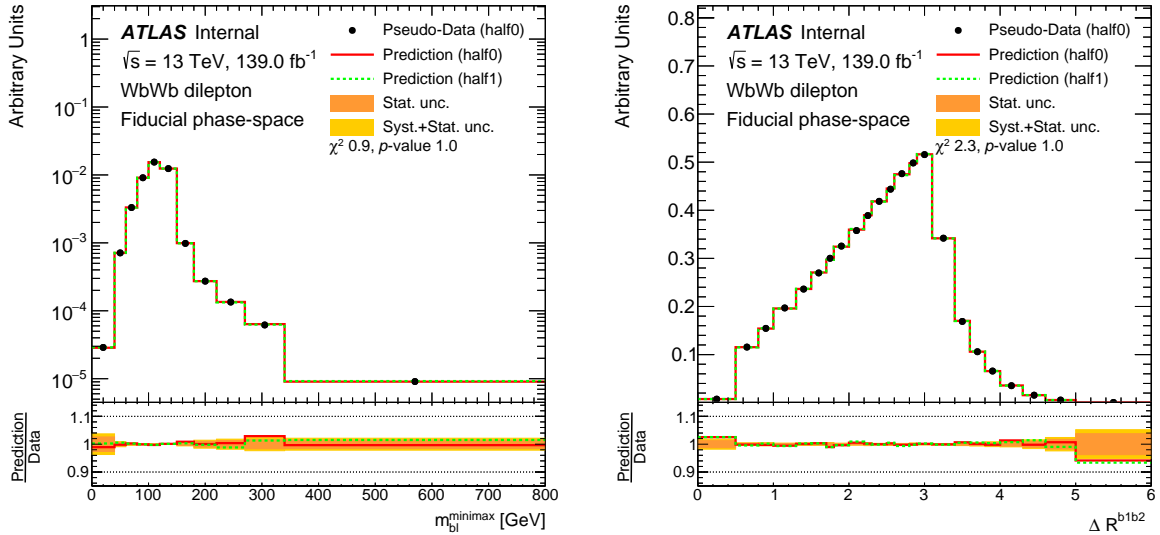


Figure 4.8: Closure tests for the particle-level normalized differential cross-sections as a function of:  $m_{bl}^{\text{minimax}}$  in logarithmic scale (left) and  $\Delta R(b_1, b_2)$  in linear scale (right). These distributions are unfolded with `half1`, using `half0` as pseudo-data. Black dots represent the unfolded pseudo-data, red line represents the prediction of `half0`, green line is the prediction of `half1`, the orange band indicates the statistical uncertainties, while the yellow band the statistical + systematic ones.  $p$ -value is referred to the `half0` sample.

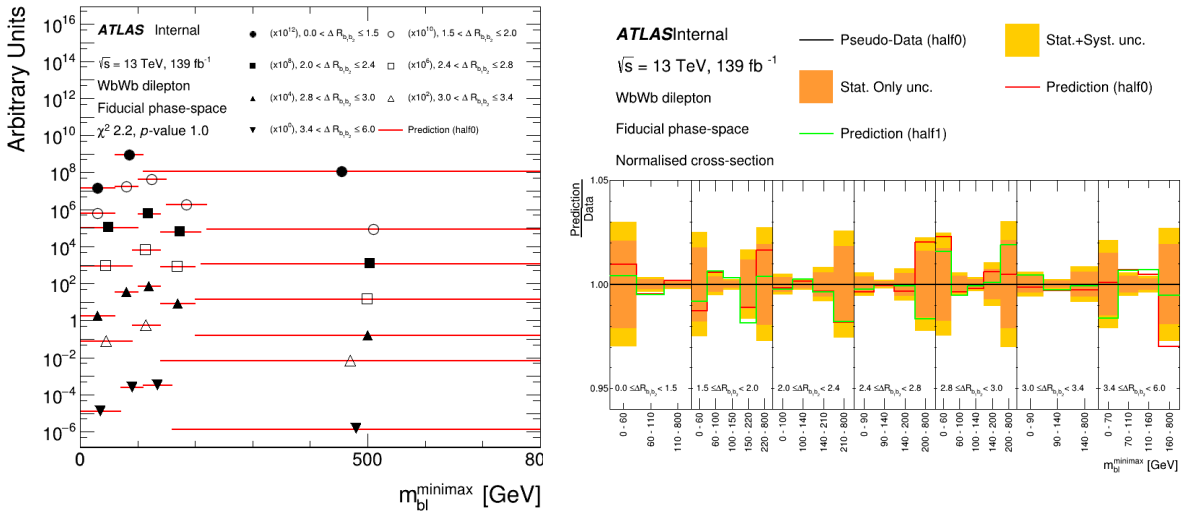


Figure 4.9: Left: 2D closure tests for the particle-level normalized differential cross-sections as a function of  $m_{bl}^{\text{minimax}}$  in bins of  $\Delta R(b_1, b_2)$ . This distribution is unfolded with `half1`, using `half0` as pseudo-data. Data points are placed in the center of each bin. Red line represents the prediction. Right: ratio plot of the measured cross-section to different MC predictions; black line represents the pseudo-data, red line represents the prediction of `half0`, green line is the prediction of `half1`, the orange band indicates the statistical uncertainties, while the yellow band the statistical + systematic ones.

## 4.6 Systematic uncertainties

The differential cross-section measurement is affected by several systematic uncertainties, in particular: systematic uncertainties due to **detector effects** and systematic uncertainties related to **signal and background MC modelling**.

Each systematic uncertainty caused by detector effects has been evaluated before and after the unfolding procedure (described in Section 4.5). Systematics are evaluated by unfolding the varied MC detector-level spectra with nominal corrections and then comparing the unfolded result with the particle-level distribution of the generator, corresponding to the detector-level spectrum which has been unfolded (in essence, looking into a non-closure under different assumptions at the detector level and correction levels). The relative uncertainties evaluated with this procedure are directly applied to the unfolded data.

In the results presented in this thesis not all the sources of systematic uncertainties have been accounted for: samples needed for the evaluation of the missing uncertainties are currently being processed. Missing uncertainties are described in Appendix C.4.

### 4.6.1 Detector related systematics

The detector systematics refer to the quality of the detector simulation used to describe the detector response for each of the reconstructed object. These systematic uncertainties are evaluated using varied simulated signal, to which a varied background is added; this is followed by the unfolding procedure, using the nominal correction factors and background estimation.

The sources of systematic uncertainties considered in this thesis are:

- **Lepton reconstruction and efficiency:** this uncertainty is related to the MC modelling of the lepton trigger, identification, energy or momentum resolution and reconstruction efficiencies, estimated from  $Z \rightarrow ee/\mu\mu$ ,  $J/\psi \rightarrow ee/\mu\mu$  and  $W \rightarrow e\nu$  processes (see Section 3). These uncertainties are relatively small and are specific to each lepton flavor and therefore uncorrelated between channels. In particular, these uncertainties are divided into *lepton scale and resolution* uncertainties and *lepton efficiency* uncertainties. Only uncertainties on the efficiency of the lepton reconstruction, identification, isolation and (for muons only) *track-to-vertex association* (TTVA) are considered here.
- **JVT:** the jet vertex tagger efficiency scale factor weight is used to correct for the JVT efficiency and hence match MC and data. This systematic is found by varying the scale factor weight of  $\pm 1\sigma$  and affects the reconstruction efficiency in the total fiducial cross-section.

- ***b*-tagging:** this systematic is associated to *b*-tagging jets originating from *b*-quarks and it is grouped into three categories: i) the efficiency of the *b*-tagging algorithm, ii) the mis-tag efficiency (due to *c*-quarks passing the *b*-tag requirement) and iii) the rate at which light-flavor jets are tagged. Efficiencies are estimated from data and are parameterized as a function of  $p_T$  and  $\eta$ .
- **Luminosity:** the uncertainty in the combined 2015–2018 integrated luminosity is 1.7% [92], obtained using the LUCID-2 detector [93] for the primary luminosity measurements.

### 4.6.2 Signal modelling

The source of signal modelling systematic uncertainties considered in this thesis are

- **Uncertainty due to the choice of the removal scheme:** the choice of the removal scheme of the  $t\bar{t}$  and  $tW$  interference used in the signal modelling affects the kinematic properties of simulated events and reconstruction efficiencies. To quantify this effect, events simulated with different removal scheme have been used to assess the impact of this source of systematic uncertainty. The uncertainty is determined by unfolding a sample obtained with the Diagram Subtraction (DS) scheme using corrections and response matrices from the sample obtained with the Diagram Removal (DR) scheme. The unfolded result is then compared to the particle level spectrum of the DS sample and that relative difference is used as the systematic uncertainty from the DR/DS choice.
- **Finite sample statistics of the MC generator:** it is related to the limited statistics of the signal sample; in this case, pseudo experiments have been used to evaluate the impact of finite statistics. The number of events in each bin was smeared by a Gaussian shift with mean equal to the yield of the bin and standard deviation equal to the uncertainty of the bin itself. Then, the smeared spectrum was unfolded. The resulting systematic uncertainty was found to be below 0.5%, increasing to 1-2% in the tails of some distributions.

No background systematics have been considered in this measurement.

### 4.6.3 Systematic uncertainties summary

Figures 4.10 and 4.11 present the uncertainties in the particle-level normalized differential cross-sections as a function of some of the different  $m_{bl}^{\text{minimax}}$ ,  $\Delta R(b_1, b_2)$  and  $m_{bl}^{\text{minimax}}$  in bins of  $\Delta R(b_1, b_2)$  in the resolved and boosted topologies, respectively.

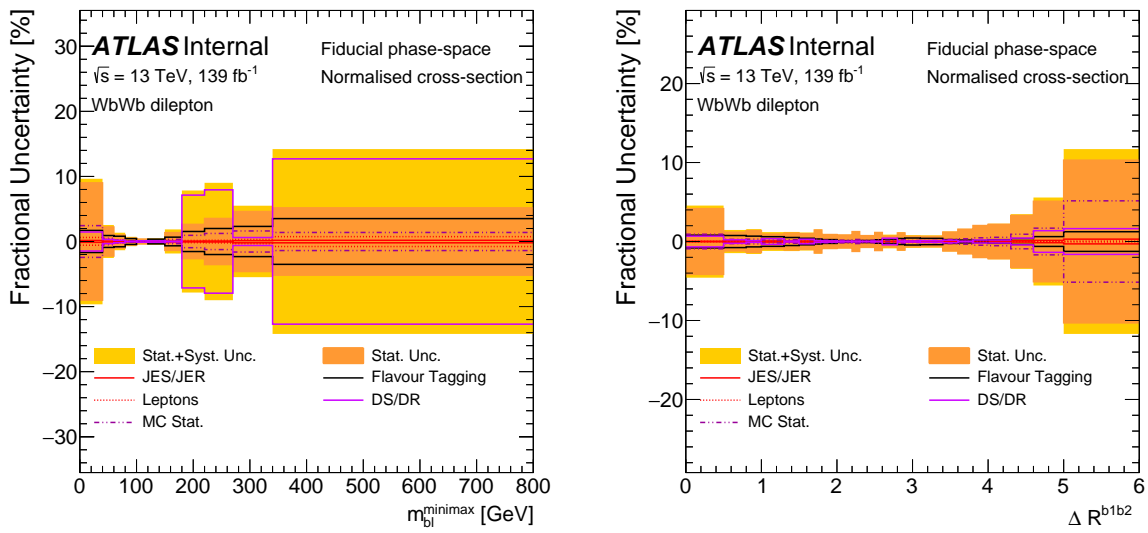


Figure 4.10: Fractional uncertainties in the particle-level normalized differential cross-sections as a function of: (left)  $m_{bl}^{\text{minimax}}$  and (right)  $\Delta R(b_1, b_2)$ . The black line represents the flavour tagging uncertainty, purple line is the DS/DR uncertainty, purple dotted line is the MC statistical uncertainty, red line is the JVT uncertainty, red dotted line is the lepton uncertainty, orange band is the statistical uncertainty and yellow band represents the statistical + systematic one.

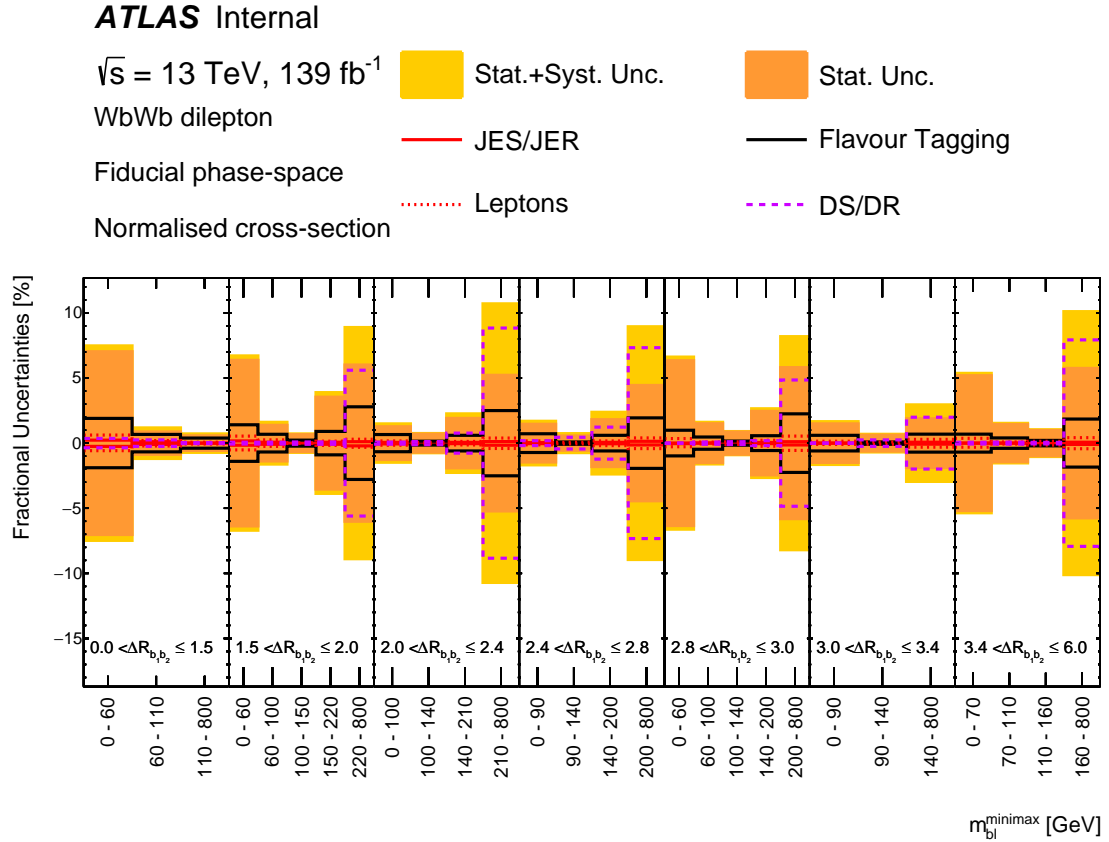


Figure 4.11: Fractional uncertainties in the particle-level normalized differential cross-section as a function of the 2D  $m_{bl}^{\text{minimax}}$  in bins of  $\Delta R(b_1, b_2)$ . The black line represents the flavour tagging uncertainty, purple dotted line is the DS/DR uncertainty, red line is the JES/JER uncertainty, red dotted line is the lepton uncertainty, orange band is the statistical uncertainty and yellow band represents the statistical + systematic one.

## 4.7 Results

In this section all the particle-level normalized differential cross-sections for the studied variables (see Section 4.4) are presented. In Figure 4.12 the particle-level normalized double-differential cross-sections as a function of the 1D particle-level  $m_{bl}^{\min\max}$  and 1D particle-level  $\Delta R(b_1, b_2)$  are shown. In Figure 4.13, on the left, the particle-level normalized differential cross-section as a function of the 2D  $m_{bl}^{\min\max}$  in bins of  $\Delta R(b_1, b_2)$  is shown and, on the right, the ratio of the measured cross-section to different MC predictions is presented.

The choice of measuring normalized differential cross-sections brings the advantage of having more precise measurements, thanks to the cancellation of correlated uncertainties, at the cost of the loss of the information on the total cross-section. The total cross-section is measured separately and is presented in Table 4.4.

Sample	Fiducial cross-section [pb]
Data	$7.49 \pm 0.22$
$t\bar{t} + tWb$ (Powheg+Pythia8, DS)	$7.4671 \pm 0.0017$
$t\bar{t} + tWb$ (Powheg+Pythia8, DR)	$7.4907 \pm 0.0015$

Table 4.4: Total fiducial  $t\bar{t} + tWb$  cross-section in the  $e\mu$  channel. The uncertainty on the measurements is due to the data statistics, the scale factor uncertainties and the interference removal scheme, as described in Section 4.6. The uncertainty on the POWHEG + PYTHIA8 predictions is based on the MC statistics only.

The DR and DS schemes model in a different way the quantum interference description. Looking at the final  $m_{bl}^{\min\max}$  distributions, we observe that DR scheme better describes the measurement in the interference region, with respect to the DS one. This is even more clear in the double-differential distribution shown in Figure 4.13. Concerning the single-differential distribution  $\Delta R(b_1, b_2)$ , present results does not allow to conclude any discrimination among DR vs DS schemes.

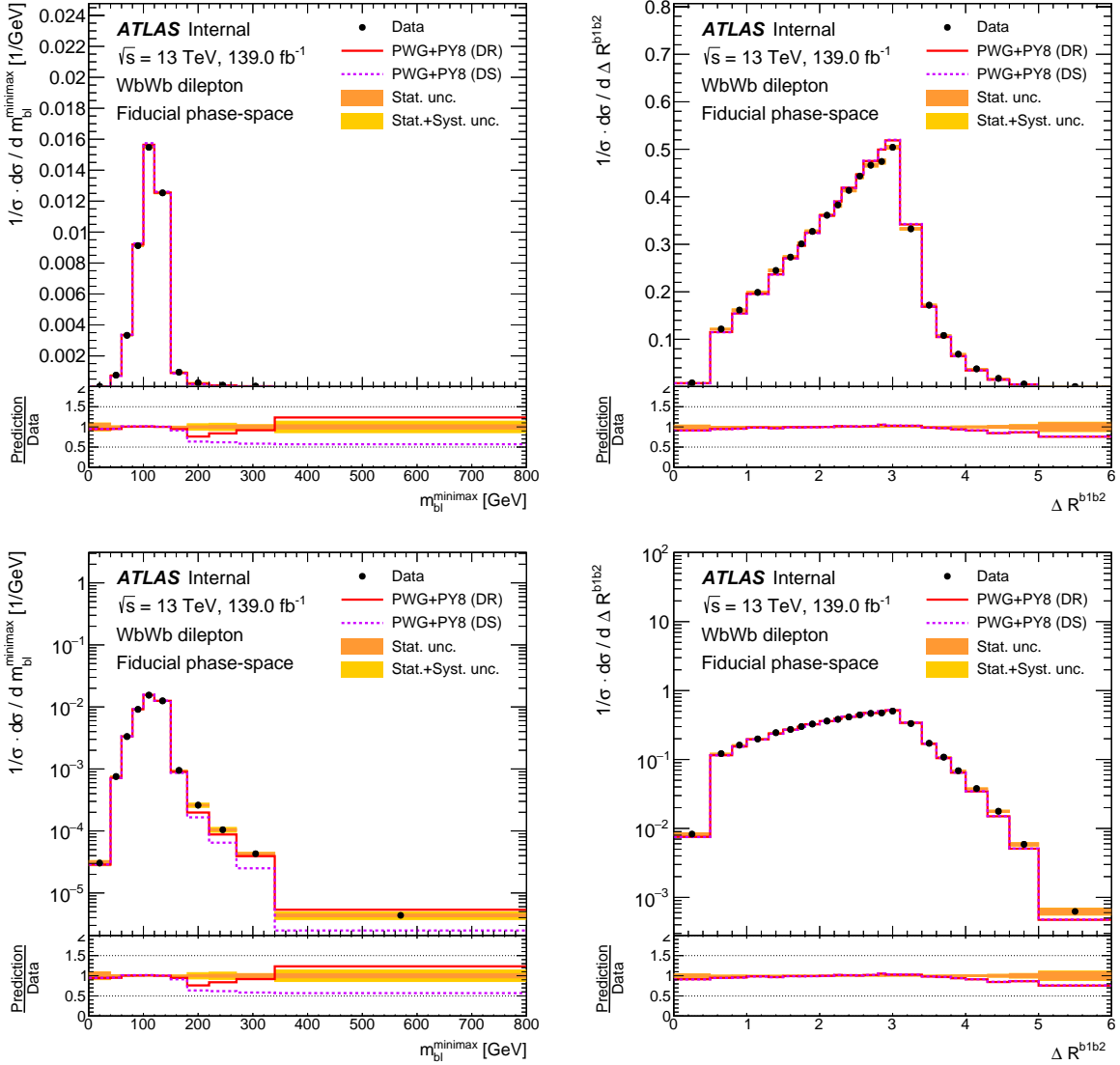


Figure 4.12: Particle-level normalized differential cross-section as a function of: (upper left)  $m_{bl}^{minimax}$  and (upper right)  $\Delta R(b_1, b_2)$  in linear scale. The black dots represent the data, red line is the PWG+PY8  $t\bar{t} + tW$  MC prediction in the DR scheme, purple dotted line is the PWG+PY8  $t\bar{t} + tW$  MC prediction in the DS scheme, orange band represents the statistical uncertainty and yellow band the statistical + systematic one. The ratio plot below shows the prediction over data ratio. In the lower left and right panels it is possible to observe the logarithmic scale distributions.

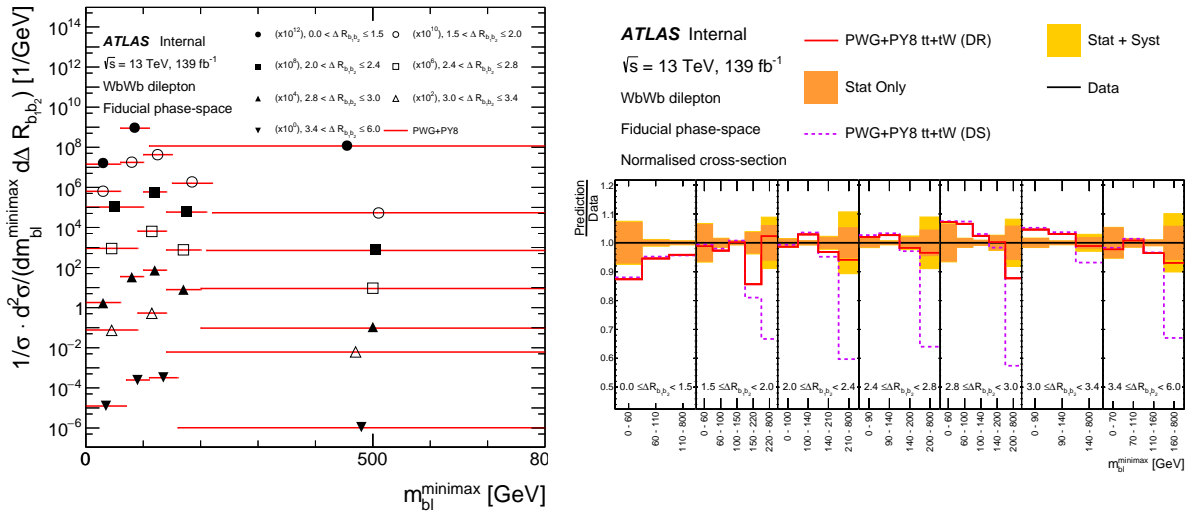


Figure 4.13: Left: Particle-level normalized differential cross-section as a function of 2D  $m_{bl}^{\minmax}$  in bins of  $\Delta R(b_1, b_2)$  in the resolved topology compared with the prediction obtained with the POWHEG + PYTHIA8 MC generator. Data points are placed to the center of each bin. Red line represents the prediction. Right: ratio plot of the measured cross-section to different MC predictions; black line represents the data, red line represents the PWG+PY8  $t\bar{t} + tW$  MC prediction in the DR scheme, purple dotted line is the PWG+PY8  $t\bar{t} + tW$  MC prediction in the DS scheme, the orange band indicates the statistical uncertainties, while the yellow band the statistical + systematic ones.

# Conclusions and outlook

This work reports the study of the quantum interference between singly and doubly resonant top quark productions. The analysis was performed on the full dataset collected by the ATLAS experiment in proton-proton collisions at the LHC during the Run-2 at  $\sqrt{s} = 13 \text{ TeV}$  with an integrated luminosity of  $139 \text{ fb}^{-1}$ .

The cross-section of the  $WbWb$  final-state in the  $e\mu$  channel at the particle level has been measured as a function of two interference-sensitive variables,  $m_{bl}^{\minimax}$  and  $\Delta R(b_1, b_2)$ , by using an iterative Bayesian unfolding method. In particular, we have extracted the single-differential cross-sections as a function of  $m_{bl}^{\minimax}$  and  $\Delta R(b_1, b_2)$  and the double-differential cross-section as a function of  $m_{bl}^{\minimax}$  in bins of  $\Delta R(b_1, b_2)$ .

The analysis strategy focused on:

- The study of the impact parameters of final-state lepton tracks.
- The production of the control plots used in the description of the event selection.
- The determination of the systematic uncertainties related to the considered variables.
- The final cross-section extraction with unfolding methods with particular focus on the resolution and binning optimization with closure tests.

In conclusion, the  $WbWb$  differential cross-section has been successfully extracted and compared to the predictions of the DR and the DS subtraction schemes. These schemes model the quantum interference description in a different way. On the basis of the final  $m_{bl}^{\minimax}$  distributions, we can preliminary conclude that the DR scheme better describes the measurement in the interference region with respect to the DS one. This is even more clear in the double-differential distribution of  $m_{bl}^{\minimax}$  in bins of  $\Delta R(b_1, b_2)$ . Concerning the single-differential distribution in  $\Delta R(b_1, b_2)$ , the present result does not allow to discriminate among DR vs DS schemes.

However, only the dominant systematic uncertainties have been considered. Once evaluated all the systematic uncertainties, it will be possible to calculate the complete covariance matrix, in order to provide a quantitative comparisons with theoretical predictions through a goodness-of-fit test.

We expect that the measurements will be limited in the  $tW$  dominated regions by the interference modelling uncertainties, that should be strongly reduced when a full  $WbWb$  simulation will be used instead of separate  $t\bar{t}$  and  $tW$  simulations.

# Appendix A

## Physical foundations complements

In this appendix all the complementary topics related to the Chapter 1 are shown. In Section A.1 a brief overview on the Dirac and Pauli matrices is presented, while in Section A.2 an introduction to the cross-section theory is outspread.

### A.1 Dirac and Pauli matrices

**Pauli matrices** are defined as:

$$\sigma_1 = \begin{pmatrix} 0 & 1 \\ 1 & 0 \end{pmatrix}, \quad \sigma_2 = \begin{pmatrix} 0 & -i \\ i & 0 \end{pmatrix}, \quad \sigma_3 = \begin{pmatrix} 1 & 0 \\ 0 & -1 \end{pmatrix} \quad (\text{A.1})$$

for them hold the following relation:

$$\sigma_1^2 = \sigma_2^2 = \sigma_3^2 = \begin{pmatrix} 1 & 0 \\ 0 & 1 \end{pmatrix} \quad (\text{A.2})$$

and also this commutation rule:

$$[\sigma_i, \sigma_j] = 2i\epsilon^{ijk}\sigma_k \quad (\text{A.3})$$

where  $\epsilon^{ijk}$  is the Levi-Cita tensor.

Instead the **Dirac Gamma matrices** are:

$$\gamma^i = \begin{pmatrix} 0 & \sigma_i \\ -\sigma_i & 0 \end{pmatrix}, \quad \gamma^0 = \begin{pmatrix} I & 0 \\ 0 & -I \end{pmatrix} \quad (\text{A.4})$$

where  $I$  is the identity matrix. They satisfy the Clifford algebra, through which, considering the Minkowski metric, they have to satisfy the following relations:

$$\gamma^0 = (\gamma^0)^\dagger, \quad \gamma^i = -(\gamma^i)^\dagger \quad (\text{A.5})$$

$$\gamma^0\gamma^0 = I, \quad \gamma^i\gamma^i = -I \quad (\text{A.6})$$

The fifth Gamma matrix is important to define the chirality operator and is defined as:

$$\gamma^5 = i\gamma^0\gamma^1\gamma^2\gamma^3 = \begin{pmatrix} 0 & I \\ I & 0 \end{pmatrix} \quad (\text{A.7})$$

It satisfies the following relation:

$$\gamma^5 = (\gamma^5)^\dagger \quad (\text{A.8})$$

## A.2 Cross section theory and perturbative expansions

At hadron colliders, due to the large quantity of processes that can happen and interfere during the measurements of a certain process (see Figure A.1), it is fundamental to do good predictions about data and quantities. Fixed-order predictions are, for example, fundamental in the case of calculations related to particular scattering processes. Higher order calculations to the quantities like the cross-section are the key to stress-test the SM and look for new physics effects. Let's start by considering the classic hadronic-process cross-section (that is for example the one of  $pp \rightarrow t\bar{t}$ ):

$$d\sigma = \sum_{i,j} \int d\vec{x}_i f_i(\vec{x}_i, \mu^2) \int d\vec{x}_j f_j(\vec{x}_j, \mu^2) d\hat{\sigma}_{ij}(\hat{s}, \mu^2, m_t) \quad (\text{A.9})$$

where the sum is extended over partons  $i$  and  $j$ ,  $f$  are the parton density functions (PDFs) of light quarks and gluons,  $\vec{x}$  is the momentum fractions,  $\hat{s}$  is the center-of-mass energy of partons and  $\hat{\sigma}$  is the partonic cross-section. The PDF, at lowest-order (LO), is the probability for finding a quark or gluon with a certain momentum fraction in a hadron; it is universal, but not perturbatively computable and it is determined via fit against data. The  $d\hat{\sigma}_{ij}$  is the hard partonic cross-section and is computable in perturbation theory [95].

It is possible to expand the Eq. A.9 with respect to a small coupling  $\alpha$ :

$$d\sigma = d\sigma^{\text{LO}}(\alpha^n) + d\sigma^{\text{NLO}}(\alpha^{n+1}) + d\sigma^{\text{NNLO}}(\alpha^{n+2}) + \dots \quad (\text{A.10})$$

the first term is at LO, the second one is at next-to-leading-order (NLO) and the third one is at next-to-next-to-leading-order (NNLO). The expansion could continue also for larger order corrections. At the LHC is considered:  $\alpha = \alpha_s$  (QCD coupling), but also  $\alpha = \alpha_{EW}$ , so the corrections could be at N-order for QCD of EW.

In QCD the coupling is a running coupling (and it depends on a parameter  $\mu$ ):

$$\alpha_s = \alpha_s(\mu) = \frac{1}{b_0 \ln \frac{\mu^2}{\Lambda^2}} + \dots \quad (\text{A.11})$$

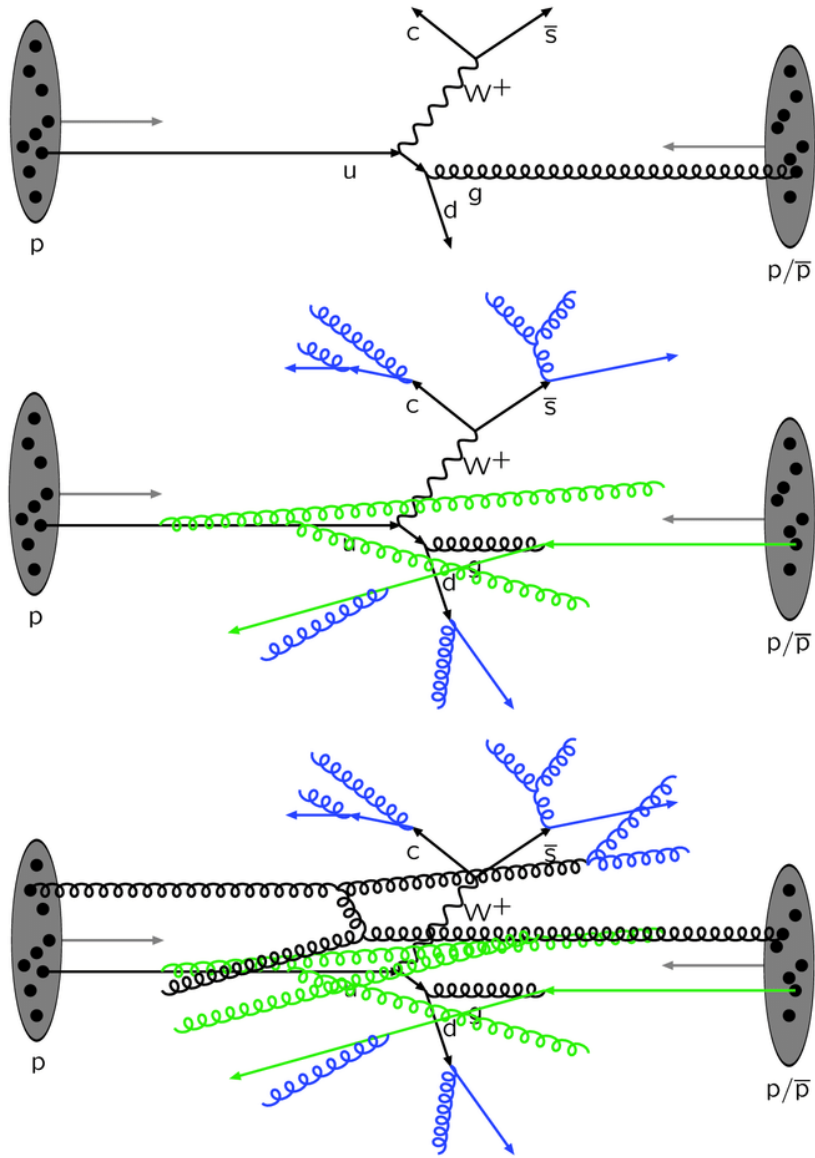


Figure A.1: Schematic view of  $p$ - $p(\bar{p})$  collision [94].

where  $b_0$  is a QCD parameter and  $\Lambda$  is the energy scale. So, the change of scale is an NLO effect ( $\propto \alpha_s$ ):

$$d\sigma^{\text{NLO}}(\mu) \propto \alpha_s(\mu)^n \quad (\text{A.12})$$

at LO, the normalization is not under control.

At NLO we have:

$$d\sigma^{\text{NLO}}(\mu) = \alpha_s(\mu)^n \mathcal{A}^{\text{LO}} + \alpha_s(\mu)^{n+1} \left( \mathcal{A}^{\text{NLO}} - nb_0 \ln \frac{\mu^2}{Q_0^2} \right) + \dots \quad (\text{A.13})$$

where  $\mathcal{A}$  are the amplitudes related to each N-order correction and  $n$  and  $Q$  are QCD parameters. So the NLO result compensates the LO scale dependence and the residual dependence is NNLO. Including higher-order corrections reduces the scale dependence. The normalization starts being under control at NLO (*compensation mechanism*).

Therefore, the ingredients to calculate fixed-order predictions for cross-sections are:

- **LO** partonic cross-section for a  $2 \rightarrow n$  process:

$$d\hat{\sigma}_{\text{LO}} = \frac{1}{2s} \int d\Phi_n |\mathcal{M}_{\text{LO}}|^2 \quad (\text{A.14})$$

where  $s$  is the squared center-of-mass energy,  $\int d\Phi_n$  is the  $n$ -particle phase-space and  $\mathcal{M}_{\text{LO}}$  is the LO matrix element.

- **NLO** partonic cross-section for a  $2 \rightarrow n$  process:

$$\begin{aligned} d\hat{\sigma}_{\text{NLO}} = & \frac{1}{2s} \int d\Phi_n [|\mathcal{M}_{\text{LO}}|^2 + 2 \text{Re}\{\mathcal{M}_{\text{LO}} \mathcal{M}_{\text{NLO},V}^*\}] \\ & + \frac{1}{2s} \int d\Phi_{n+1} |\mathcal{M}_{\text{NLO},R}|^2 \end{aligned} \quad (\text{A.15})$$

where phase spaces are at  $n$  or  $n+1$  particle level, the label  $R$  indicates the real tree-level matrix element and the label  $V$  the one-loop one.

- **NNLO** partonic cross section for a  $2 \rightarrow n$  process:

$$\begin{aligned} d\hat{\sigma}_{\text{NNLO}} = & \frac{1}{2s} \int d\Phi_n [|\mathcal{M}_{\text{LO}}|^2 + 2 \text{Re}\{\mathcal{M}_{\text{LO}} \mathcal{M}_{\text{NLO},V}^*\} + 2 \text{Re}\{\mathcal{M}_{\text{LO}} \mathcal{M}_{\text{NNLO},V}^*\}] \\ & + \frac{1}{2s} \int d\Phi_{n+1} [|\mathcal{M}_{\text{NLO},R}|^2 + 2 \text{Re}[\mathcal{M}_{\text{NLO},R} \mathcal{M}_{\text{NNLO},RV}^*]] \\ & + \frac{1}{2s} \int d\Phi_{n+2} |\mathcal{M}_{\text{NNLO},RR}|^2 \end{aligned} \quad (\text{A.16})$$

where the label are the same of before, but  $RV$  means real-virtual one loop matrix element and  $RR$  double-real tree level matrix element.

For what regard the EW higher-order corrections, we know that  $\mathcal{O}(\alpha_{EW}) \simeq \mathcal{O}(\alpha_s^2)$ , therefore, the NLO EW corrections correspond to NNLO QCD ones. Increasing the EW corrections will lead to a large effect in the tails of some distributions, like the transverse momentum  $p_T$ , the invariant mass and others. More relevant corrections from real photon radiation, photon initial states or real  $W, Z$  radiation are given.

In the cases in which QCD and EW corrections are sizeable, also mixed QCD-NLO corrections of relative  $\mathcal{O}(\alpha_{EW}\alpha_s)$  can be considered [96].

# Appendix B

## Object reconstruction complements

In this appendix all the complementary arguments related to the Chapter 3 are presented. In Section B.1 the multi-jet and  $H_T$  trigger efficiencies plots of the jet triggers are shown.

### B.1 Jet trigger efficiencies plots

**Efficiency of the  $H_T$**  and large- $R$  ( $R = 1.0$ ) triggers are shown in Figure B.1. The  $H_T$  is defined as the summed transverse energy of all jets that are reconstructed above a  $E_T$  threshold of 50 GeV. The **multi-jet trigger efficiencies** are dominated by the

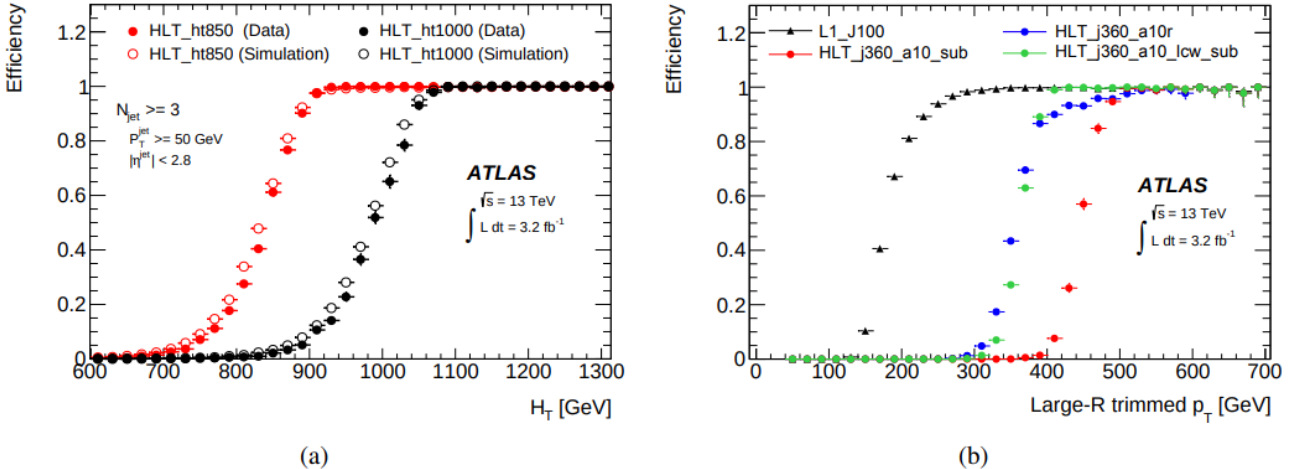


Figure B.1:  $H_T$  triggers efficiency as a function of offline  $H_T$  (a) and large- $R$  single-jet triggers as a function of offline  $p_T$  (b).

trigger efficiency of the  $N$ -th leading jet. They are shown in Figure B.2 for L1 and HLT triggers, as a function of the  $N$ -th leading jet  $p_T$ .

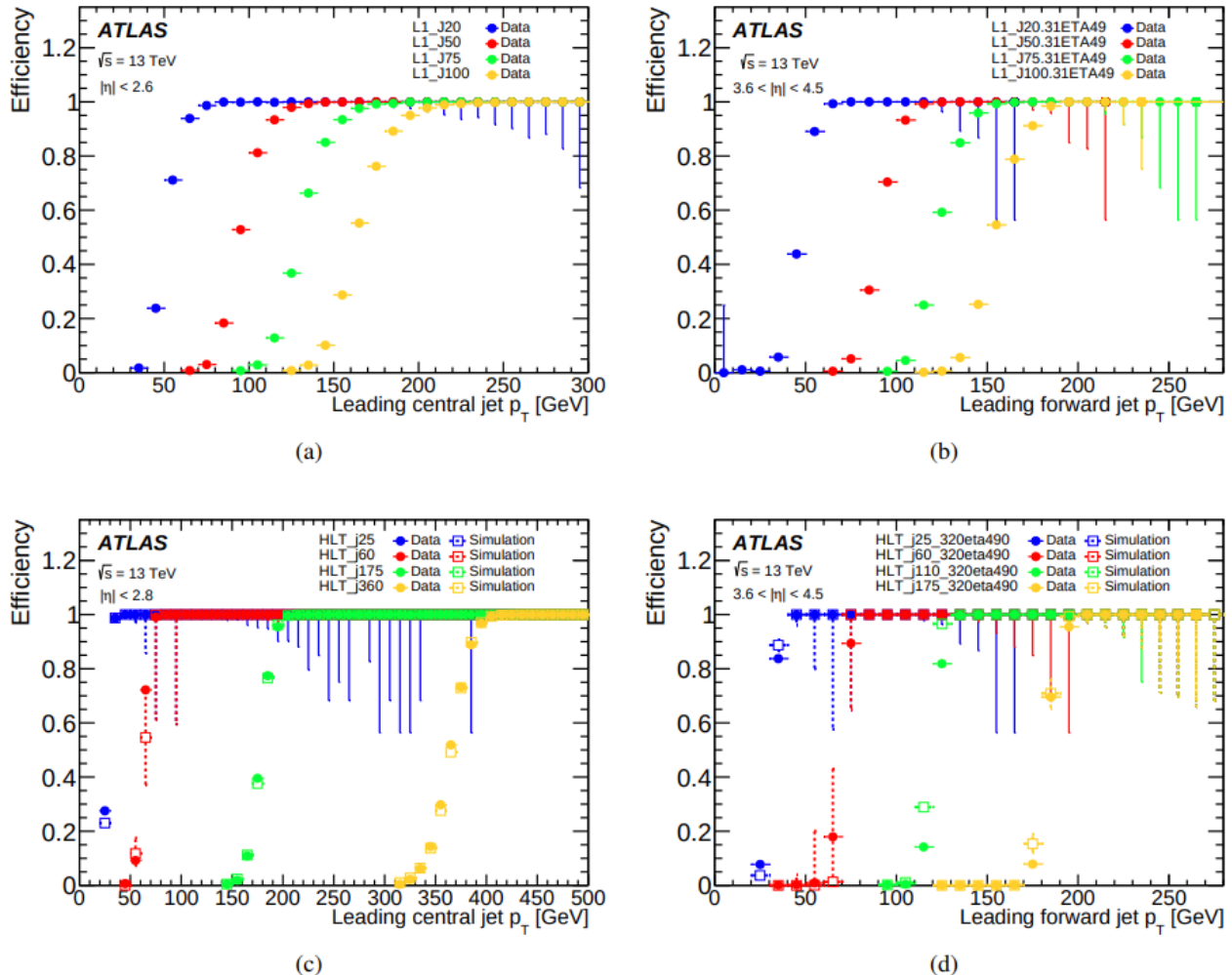


Figure B.2: The multi-jet trigger efficiencies for L1 (a) and HLT (b) triggers as a function of offline jet  $p_T$ .

# Appendix C

## Differential cross-section measurement complements

In this appendix all the complementary arguments related to the Chapter 4 are presented. In Section C.1 a study on the impact parameters of final-state lepton tracks is shown. In Section C.2 resolutions plots for  $t\bar{t}$  and  $tW$  with the binning choice and the corresponding resolution studies for  $\Delta R(b_1, b_2)$  in bins of  $m_{bl}^{\min\max}$  as a 2D internal variable are presented. In Section C.3 closure tests for the 2D  $\Delta R(b_1, b_2)$  variable in bins of  $m_{bl}^{\min\max}$  are pointed out. Finally, in Section C.4, additional sources of systematic uncertainties not used in the measurement (but useful for future improvements) are shown.

### C.1 Study of the impact parameters of final-state lepton tracks

In the perspective of performing the analysis using a full  $2b4l$  sample, which will not contain final states with two same flavor leptons ( $ee/\mu\mu/\tau\tau$ ), studies are needed to understand how to suppress  $e\mu$  events where the leptons come from the decay of a tau.

One possibility is to look at the track parameters, since in the case of the  $\tau$  decay the electrons and muons will originate from the  $\tau$  decay vertex rather than the collision's primary vertex.

The **transverse impact parameter**  $d_0$  is defined as the distance of closest approach in the  $r - \phi$  plane of the track to the primary vertex (see Section 2.2.1 for the definition of the used detector reference frame), while the **longitudinal impact parameter**  $z_0 \sin \theta$  is defined as the distance of the track to the primary vertex in the longitudinal plane at the point of closest approach in  $r - \phi$  [97] (see Figure C.1 for a graphical representation). Potentially,  $d_0$  and  $z_0 \sin \theta$  impact parameters are sensitive to events with intermediate tau leptons. The purpose of this analysis step has been the one of producing and

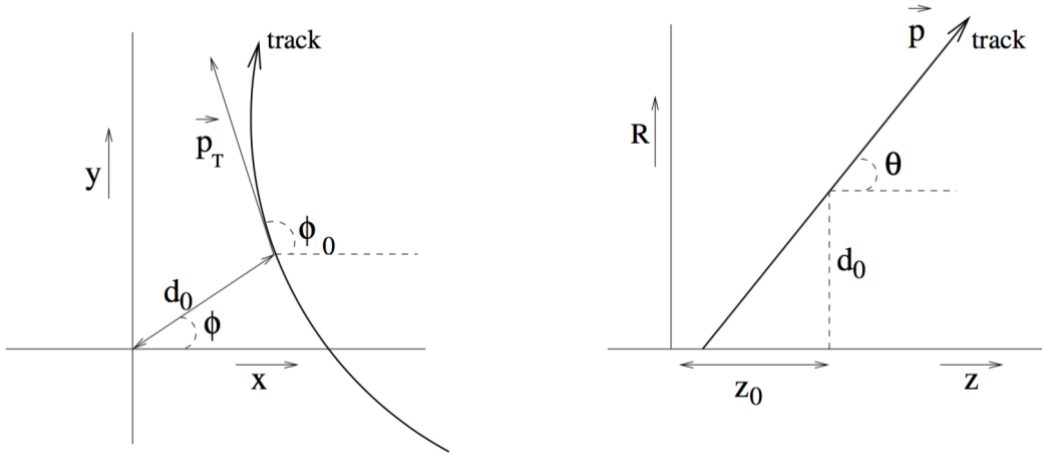


Figure C.1: Illustration of the impact parameters of a track in the transverse plane (left) and RZ-plane (right), as defined in the global ATLAS tracking frame [98]:  $\phi_0$  is the angle with the x-axis in the X-Y plane at the impact point,  $\theta$  is the angle with the z-axis in the R-Z plane,  $p$  is the momentum and  $p_T$  the transverse component.

studying the impact parameters plots for final-state lepton events coming or not from intermediate tau leptons decays. In Figures C.2, C.3 and C.4 respectively the impact parameters distributions for electrons, muons and electrons + muons events are shown, while in Figure C.5 the 2D dimensional distributions are presented. This analysis has been performed in lepton+jets events from  $t\bar{t}$  decays that, in this case, holds the same informations as the  $WbWb$  final-states.

As a conclusion it is possible to observe that both the impact parameters are sensitive to the origin of the final-state leptons, but the most sensitive one is the  $d_0$  parameter for electrons: as shown in Figure C.2 (left), electrons coming from  $\tau$  have a much wider distribution in respect to the other coming from  $W$ .

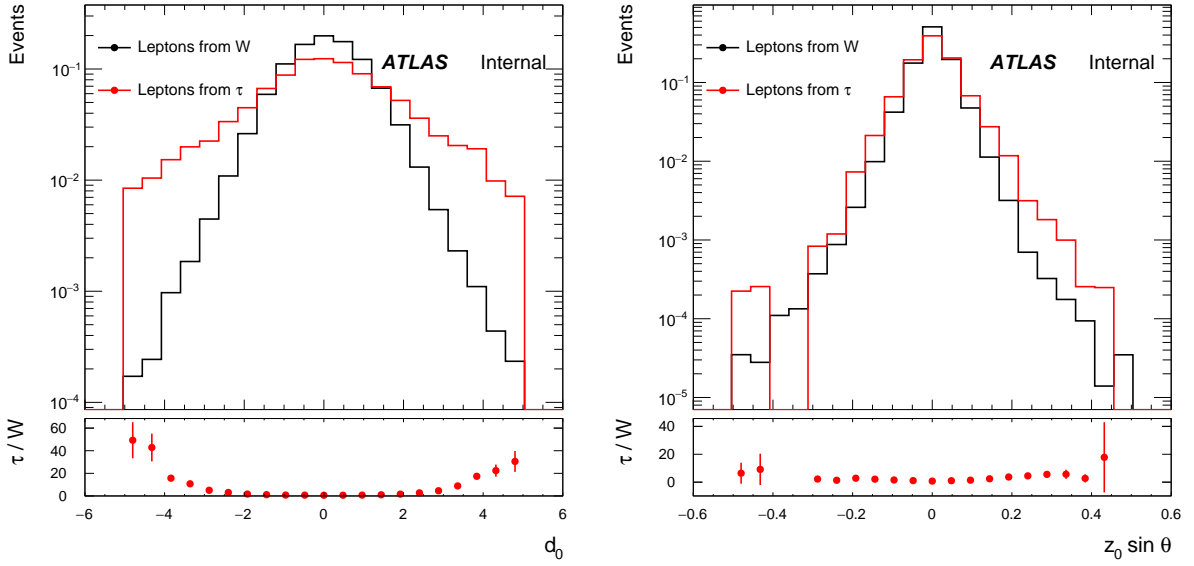


Figure C.2:  $d_0$  and  $z_0 \sin \theta$  impact parameters distributions for **electrons** coming from  $\tau$  or  $W$ . The  $\tau/W$  plot shows the ratio between lepton events coming from  $\tau$  and  $W$  respectively.

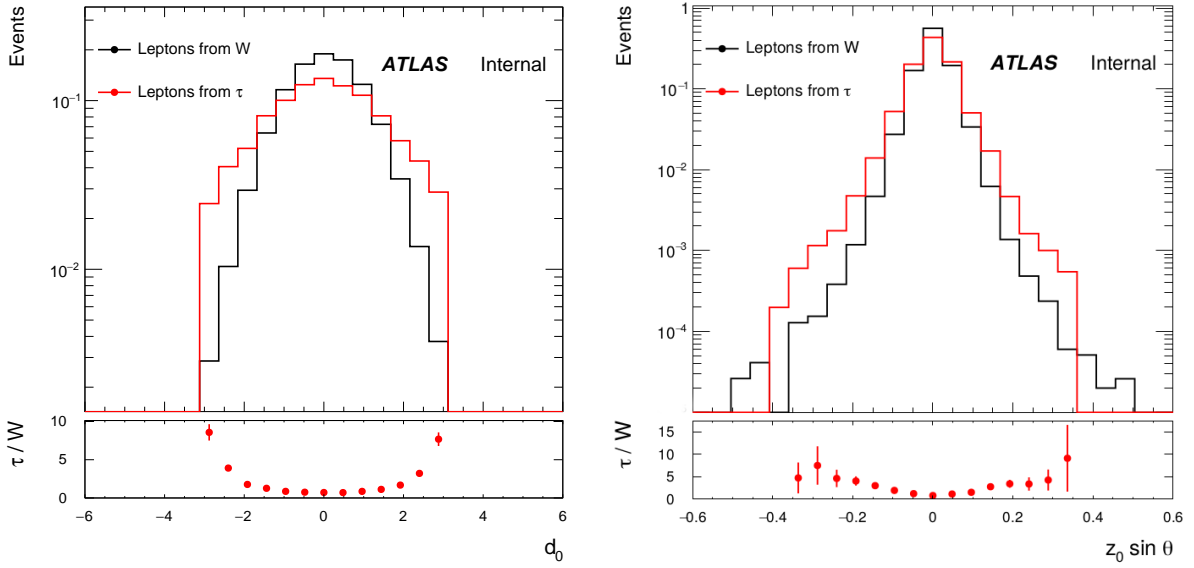


Figure C.3:  $d_0$  and  $z_0 \sin \theta$  impact parameters distributions for **muons** coming from  $\tau$  or  $W$ . The  $\tau/W$  plot shows the ratio between lepton events coming from  $\tau$  and  $W$  respectively.

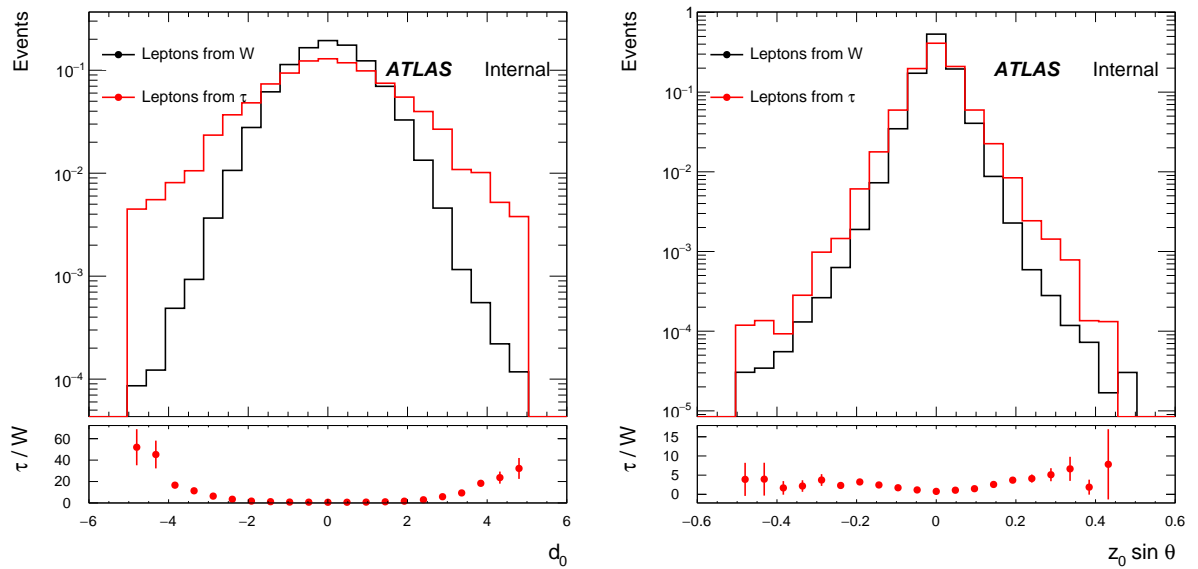


Figure C.4:  $d_0$  and  $z_0 \sin \theta$  impact parameters distributions for electrons and muons coming from  $\tau$  or  $W$ . The  $\tau/W$  plot shows the ratio between lepton events coming from  $\tau$  and  $W$  respectively.

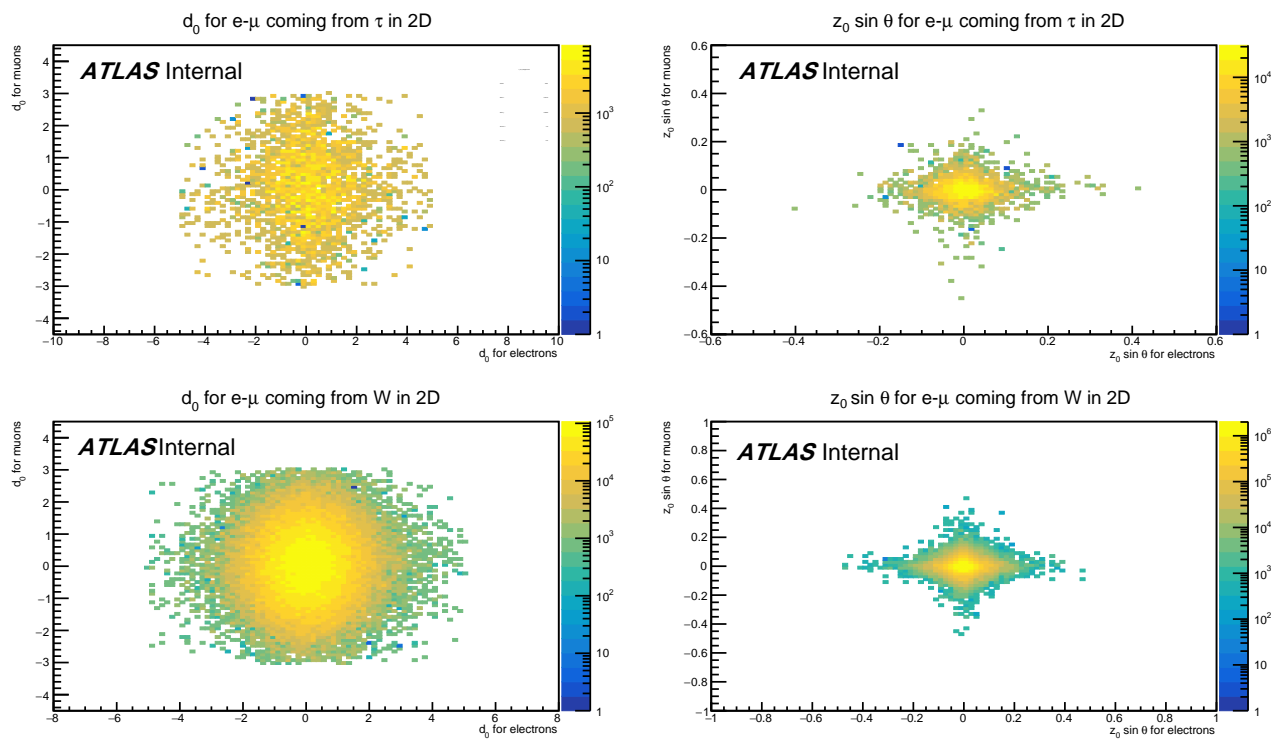


Figure C.5: 2D impact parameters plots for leptons coming from  $\tau$  or  $W$ . Plots are in logarithmic scale for the  $z$  axis.

## C.2 Resolution plots and binning choice complements

In this section, complementary informations to the resolution plots and the binning choice are presented. In particular, complementary topics are provided for: resolution plots for  $m_{bl}^{\minimax}$  and  $\Delta R(b_1, b_2)$  variables with  $t\bar{t}$  and  $tW$  samples only (see Section C.2.1) and resolution plots and binning choice for the  $\Delta R(b_1, b_2)$  in bins of  $m_{bl}^{\minimax}$  2D variable (see Section C.2.2), discharged due to bin instability.

### C.2.1 Resolution plots for $t\bar{t}$ and $tW$

Resolution plots for  $m_{bl}^{\minimax}$  and  $\Delta R(b_1, b_2)$  variables with  $t\bar{t}$  (see Figures C.6 and C.7) and  $tW$  (see Figures C.8-C.11) samples only are shown below.

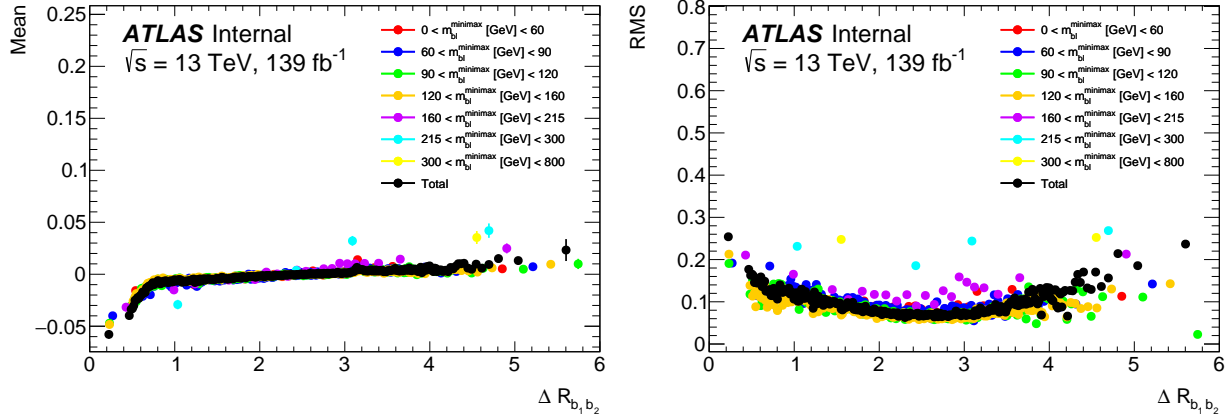


Figure C.6: Mean and RMS of the resolution distributions for  $\Delta R(b_1, b_2)$  as a function of the particle-level  $\Delta R(b_1, b_2)$  in bins of  $m_{bl}^{\minimax}$  for the  $t\bar{t}$  sample.

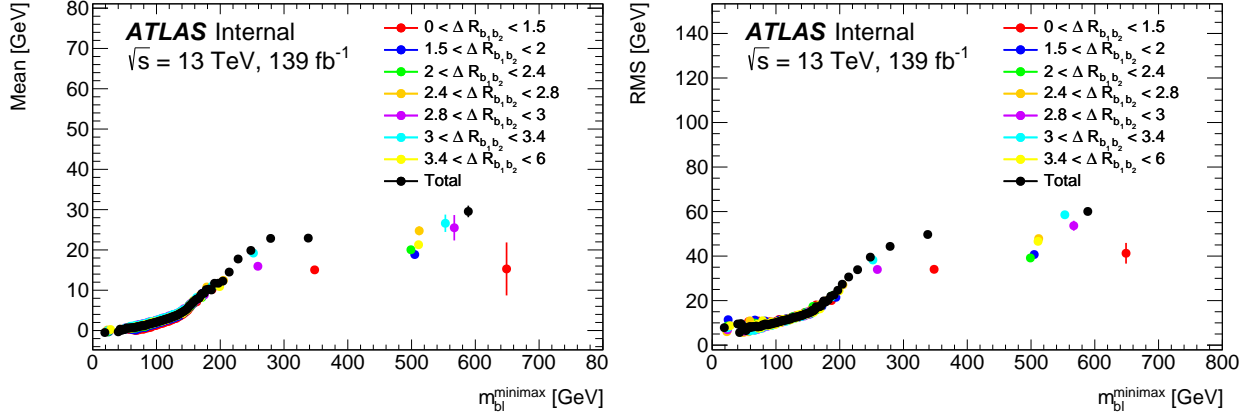


Figure C.7: Mean and RMS of the resolution distributions for  $m_{bl}^{\text{minimax}}$  as a function of the particle-level  $m_{bl}^{\text{minimax}}$  in bins of  $\Delta R(b_1, b_2)$  for the  $t\bar{t}$  sample.

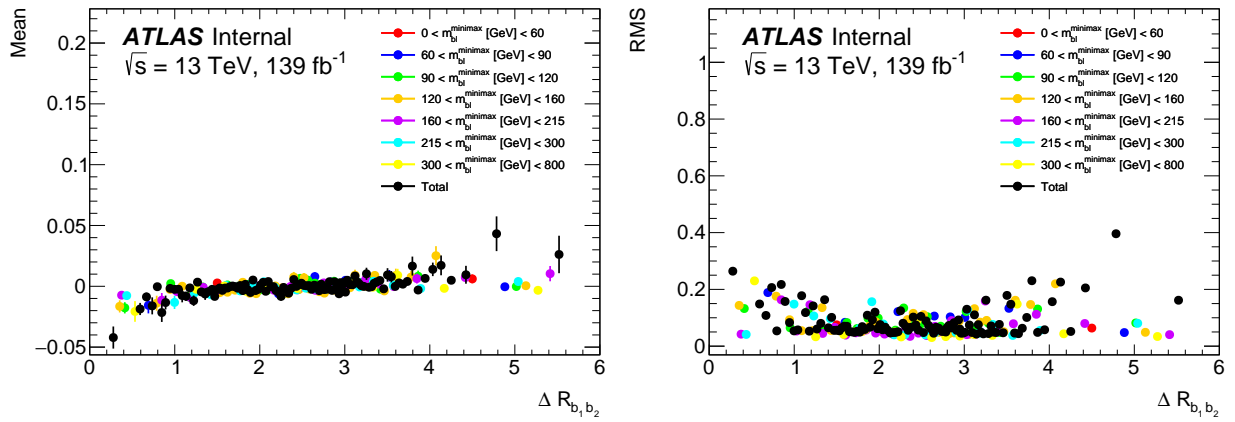


Figure C.8: Mean and RMS of the resolution distributions for  $\Delta R(b_1, b_2)$  as a function of the particle-level  $\Delta R(b_1, b_2)$  in bins of  $m_{bl}^{\text{minimax}}$  for the  $tW$  sample in the DR scheme.

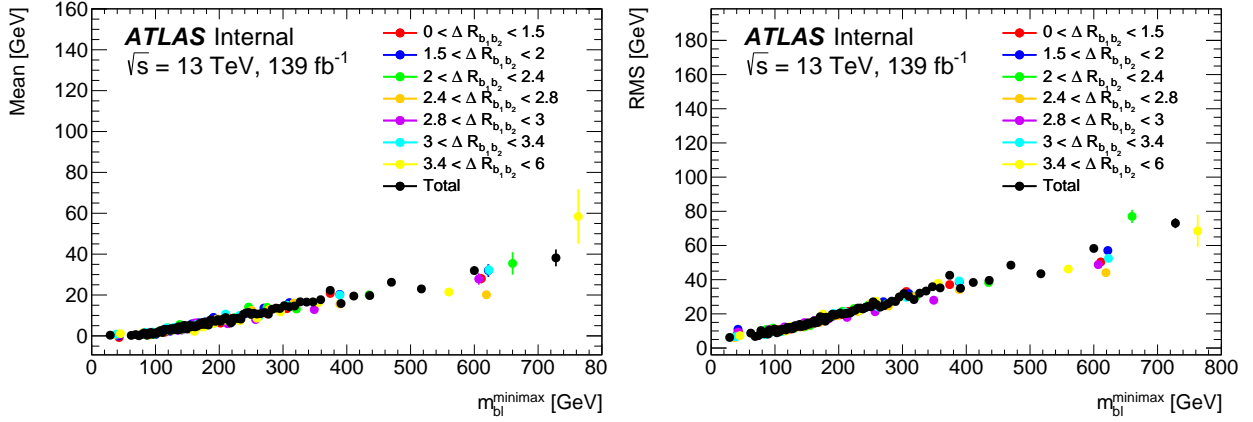


Figure C.9: Mean and RMS of the resolution distributions for  $m_{bl}^{minimax}$  as a function of the particle-level  $m_{bl}^{minimax}$  in bins of  $\Delta R(b_1, b_2)$  for the  $tW$  sample in the DR scheme.

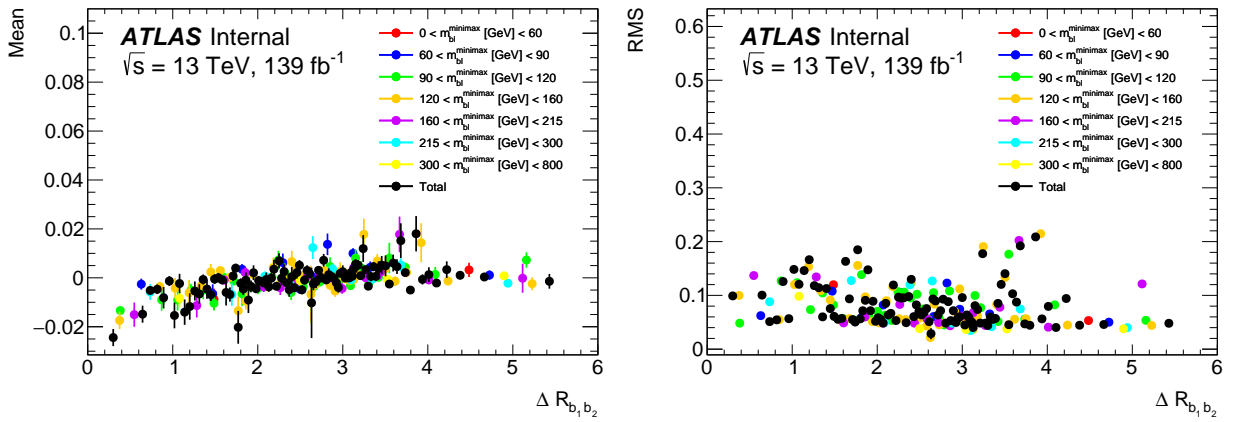


Figure C.10: Mean and RMS of the resolution distributions for  $\Delta R(b_1, b_2)$  as a function of the particle-level  $\Delta R(b_1, b_2)$  in bins of  $m_{bl}^{minimax}$  for the  $tW$  sample in the DS scheme.

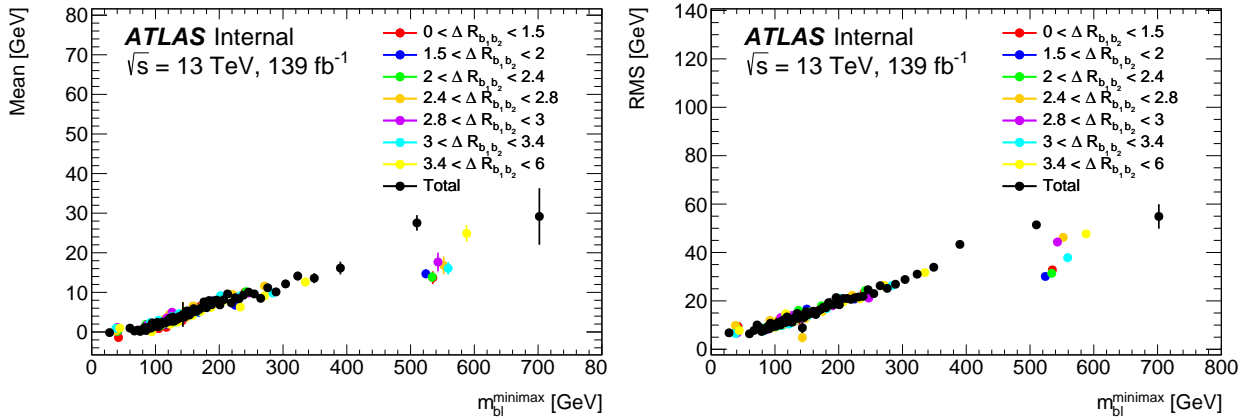


Figure C.11: Mean and RMS of the resolution distributions for  $m_{bl}^{\text{minimax}}$  as a function of the particle-level  $m_{bl}^{\text{minimax}}$  in bins of  $\Delta R(b_1, b_2)$  for the  $tW$  sample in the DS scheme.

### C.2.2 Binning and resolution plots for $\Delta R(b_1, b_2)$ in bins of $m_{bl}^{\text{minimax}}$

Binning choice for the  $\Delta R(b_1, b_2)$  in bins of  $m_{bl}^{\text{minimax}}$  as a 2D internal variable is shown in Table C.1. Resolution plot, showing the RMS and mean of  $T - R$  as a function of  $T$ ,

Variable	Type	$\delta$	$k$	Bin edges
$\Delta R_{b_1 b_2}$ in $m_{bl}^{\text{minimax}} (0, 60)$	2D internal	2	5	0, 1.7, 2.8, 6
$\Delta R_{b_1 b_2}$ in $m_{bl}^{\text{minimax}} (60, 90)$	2D internal	2	5	0, 1.7, 2, 2.4, 2.7, 3, 3.3, 3.7, 4.1, 6
$\Delta R_{b_1 b_2}$ in $m_{bl}^{\text{minimax}} (90, 120)$	2D internal	2	5	0, 0.6, 1.1, 1.5, 1.8, 2.1, 2.4, 2.7, 3, 3.3, 3.6, 4, 4.4, 6
$\Delta R_{b_1 b_2}$ in $m_{bl}^{\text{minimax}} (120, 160)$	2D internal	2	5	0, 0.6, 1, 1.4, 1.8, 2.1, 2.3, 2.6, 2.9, 3.2, 3.5, 3.9, 6
$\Delta R_{b_1 b_2}$ in $m_{bl}^{\text{minimax}} (160, 215)$	2D internal	2	5	0, 1.5, 2.9, 6
$\Delta R_{b_1 b_2}$ in $m_{bl}^{\text{minimax}} (215, 800)$	2D internal	2	5	0, 2.4, 3.3, 6

Table C.1: Requirements for binning and chosen bins for  $\Delta R_{b_1 b_2}$  in bins of  $m_{bl}^{\text{minimax}}$  in the case of 2D internal variables.

for the  $\Delta R(b_1, b_2)$  in bins of the  $m_{bl}^{\text{minimax}}$  variable obtained with the  $t\bar{t} + Wt$  DR sample is shown in Figure C.12, while with the  $t\bar{t} + Wt$  DS in Figure C.13.

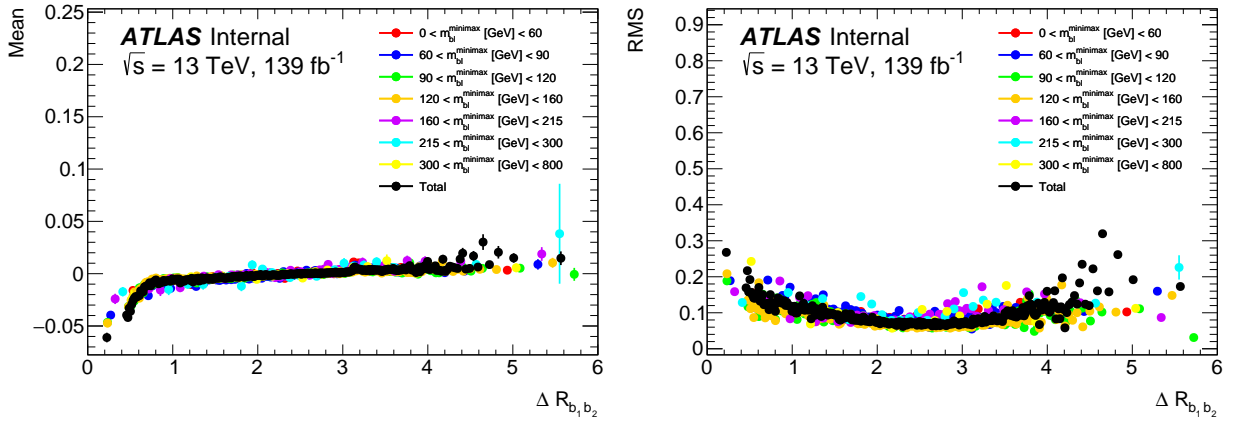


Figure C.12: Mean and RMS of the resolution distributions for  $\Delta R(b_1, b_2)$  as a function of the particle-level  $\Delta R(b_1, b_2)$  in bins of  $m_{bl}^{\text{minimax}}$  in the DR scheme.

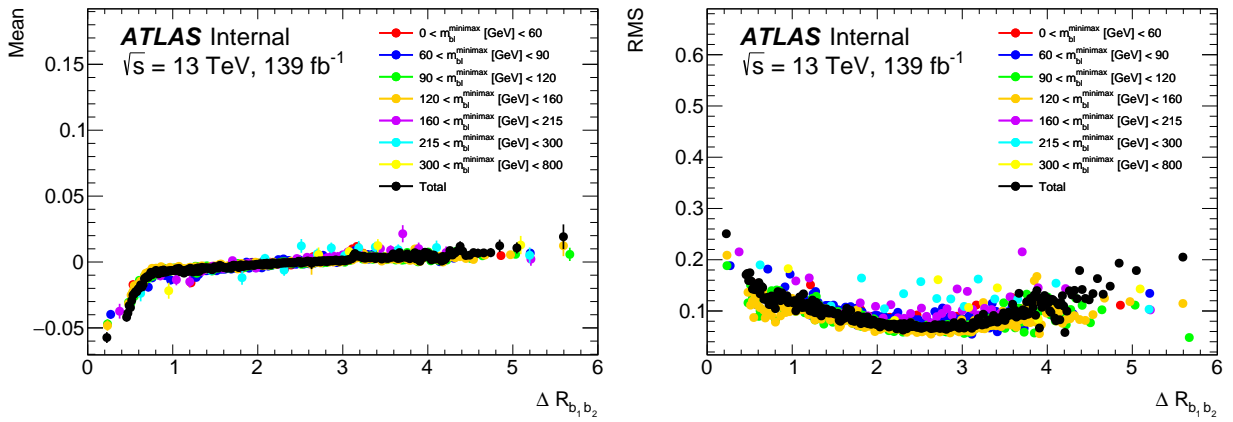


Figure C.13: Mean and RMS of the resolution distributions for  $\Delta R(b_1, b_2)$  as a function of the particle-level  $\Delta R(b_1, b_2)$  in bins of  $m_{bl}^{\text{minimax}}$  in the DS scheme.

### C.3 Closure tests for $\Delta R(b_1, b_2)$ in bins of $m_{bl}^{\text{minimax}}$

In this appendix closure tests for the particle-level normalized differential cross-section as a function of  $\Delta R(b_1, b_2)$  in bins of  $m_{bl}^{\text{minimax}}$  variable are shown. In Figure C.14, on the left, for the particle-level normalized differential cross-section as a function of  $\Delta R(b_1, b_2)$  in bins of  $m_{bl}^{\text{minimax}}$  variable is presented, while, on the right, the ratio plot of the measured cross-section to different MC predictions is showed off. Because of the

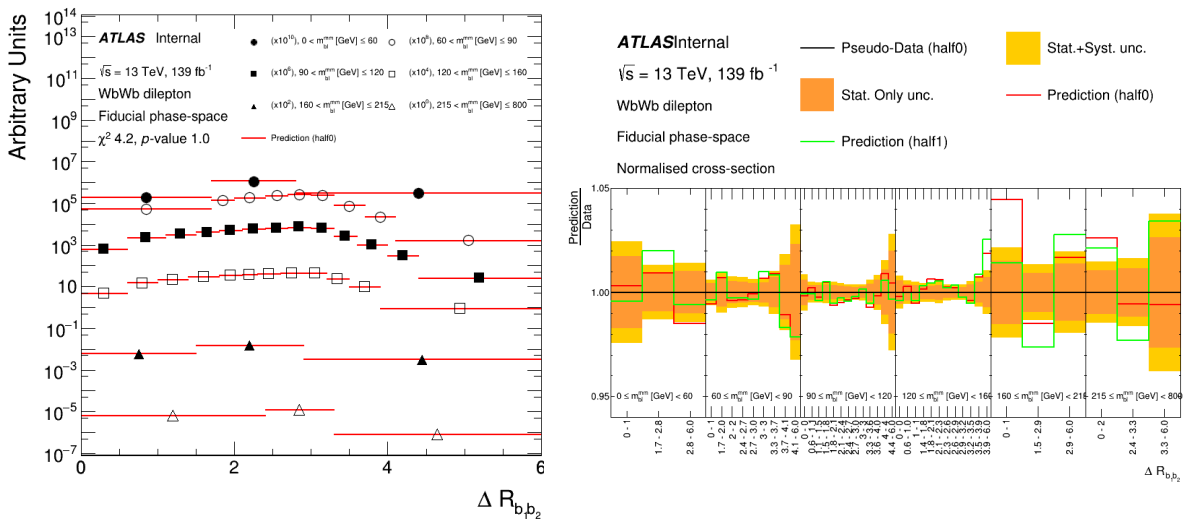


Figure C.14: Left: closure tests for the particle-level normalized differential cross-section as a function of 2D  $\Delta R(b_1, b_2)$  in bins of  $m_{bl}^{\text{minimax}}$ . This distribution is unfolded with `half1`, using `half0` as pseudo-data. Data points are placed in the center of each bin. Red line represents the prediction. Right: ratio plot of the measured cross-section to different MC predictions; black line represents the pseudo-data, red line represents the prediction of `half0`, green line is the prediction of `half1`, the orange band indicates the statistical uncertainties, while the yellow band indicates the statistical + systematic ones. For the bins  $(120 < m_{bl}^{\text{minimax}} < 160)$ ,  $(160 < m_{bl}^{\text{minimax}} < 215)$  and  $(215 < m_{bl}^{\text{minimax}} < 300)$  the instability is substantial. For this plots it has been used the notation  $m_{bl}^{\text{mm}}$  to indicate the  $m_{bl}^{\text{minimax}}$  variable.

instability of some bins (see Figure C.14 right) we decided to discard this variable and to do not use it in the main analysis.

## C.4 Systematic uncertainties not used in the analysis

Additional sources of systematic uncertainties not used in this analysis, but that can be considered for future improvements on the measurement, are described in this Section. They belong to the three categories of systematics mentioned at the beginning of Section 4.6.

Some of the additional *detector related systematics* are:

- **Jet energy scale:** this systematic is due to the uncertainty on the jet-energy scale and is estimated by varying the jet energies according to the uncertainties derived from simulation and in-situ calibration measurements.
- **Missing  $E_T^{\text{miss}}$ :** it is associated to the momenta and the energies of reconstructed objects (lepton and jets) and it is also propagated to the  $E_T^{\text{miss}}$  calculation. The  $E_T^{\text{miss}}$  reconstruction also receives contributions from the presence of low- $p_T$  jets and calorimeter cells not included in the reconstructed objects.

Some of the additional *signal modelling systematics* are:

- **Matrix element and parton shower models:** also the choice of the MC generator used in the signal modelling affects the kinematic properties of simulated  $t\bar{t} + Wt$  events and reconstruction efficiencies:  $t\bar{t} + Wt$  events simulated with different settings of POWHEG, AMC@NLO with various parton showers have to be used to assess the impact of different NLO matrix element calculations and parton shower models. The uncertainty due to the choice of matrix element generator has to be determined by unfolding MC@NLO+PYTHIA8 sample using corrections and response matrices from the POWHEG + PYTHIA 8 sample. The unfolded result is then compared to the particle level spectrum of the MC@NLO+PYTHIA8 sample and that relative uncertainty is used as the systematic uncertainty from the ME generator. The uncertainty due to the choice of parton shower or hadronization model has to be determined by unfolding a POWHEG + HERWIG 7 sample with respect to a POWHEG + PYTHIA 8 sample. The uncertainty of this is then projected onto the unfolded data by taking the relative difference with respect to the POWHEG + HERWIG 7 truth spectrum, and symmetrized.
- **Initial- and final-state QCD radiation for the signal sample:** the amount of ISR/FSR changes the number of jets in the event as well as the transverse momentum of the  $t\bar{t} + Wt$  system. To evaluate the uncertainty due to the ISR/FSR effects,  $t\bar{t} + Wt$  MC samples with modified ISR/FSR modelling have to be used. A sample generated using POWHEG + PYTHIA 8 has to be unfolded, where the factorization and renormalization scales as well as the  $h_{\text{damp}}$  parameter are simultaneously varied. The other variation is defined by scaling  $\mu_R$  and  $\mu_F$ . Then, the

spectrum, unfolded using the nominal POWHEG + PYTHIA 8 generator, has to be compared to the truth-level spectrum of the corresponding generator.

- **Parton distribution functions:** the impact of the choice of different PDF sets has to be assessed by applying an event-by-event reweighting procedure to a  $t\bar{t} + Wt$  sample generated with POWHEG + PYTHIA 8 using the 30 PDF set of the PDF4LHC15 prescription [99] as well as using the central values of the NNPDF3.0 PDF.

Also *background systematics* can be considered for future developments. Experimental and theoretical uncertainties are used to calculate the background systematics contributions, determined by MC simulation. This translates into an uncertainty on the background subtraction used in the correction procedure. This systematic is evaluated using simulated signal events to which a varied background is added and nominal background subtracted, followed by the unfolding procedure using the nominal correction factors. Background modelling systematics are divided into 3 main sub-categories, associated to each background sample and are: **systematics on  $Z+jets$** , **systematics on diboson background** and **systematics on  $t\bar{t}V$  background**.

# Acknowledgments

Questo elaborato conclude un grande percorso durato 5 anni, 5 anni di duro lavoro, sacrifici e tante soddisfazioni. Tutto ciò che ho ottenuto dal 2015 ad oggi non sarebbe stato possibile se accanto a me non ci fossero state le persone che ci sono tutt'ora. Cercherò di menzionarvi tutti, senza tralasciare nessuno e senza ovviamente classificarvi in ordine di importanza visto che tutti, a modo vostro, avete contribuito in maniera fondamentale alla mia crescita personale e culturale.

Voglio ringraziare mia mamma Daniela, mio papà Marco e mio fratello Edoardo, che mi hanno dovuto sopportare sin dall'inizio, subendosi tutte le mie sconfitte e i miei successi, senza mai smettere di credere in me e nel mio obiettivo, spronandomi ogni giorno a fare di meglio e a farmi diventare la versione migliore di me stesso. Avete assistito sin dall'inizio alle mie prime sconfitte e ai miei primi successi vedendomi cambiare giorno dopo giorno e assistendo in prima persona alla lunga e difficile scalata verso la conquista del mio sogno. Grazie soprattutto a mia mamma, che ha lavorato sin da quando sono nato per farmi guadagnare una determinazione, una sicurezza e una consapevolezza nei miei obiettivi senza cui non sarei mai potuto andare avanti; questa passione per la scienza è nata soprattutto grazie a te che, con il tuo duro lavoro e i tuoi sforzi, mi hai fatto capire davvero quanto sia importante la dedizione e la tenacia nel raggiungere le aspirazioni più importanti della vita. Grazie.

Voglio ringraziare la mia Federica, la quale, nonostante mi stia accanto da solamente 1 anno e mezzo è diventata la persona che più crede in me e nei miei obiettivi. Sin dal primo giorno in cui ti ho conosciuta hai cambiato il mio modo di essere e di vivere. Ero spaventato, all'inizio, da un possibile cambiamento e dalle conseguenze che avrebbe portato, ma ora come ora posso dire che sei stata la cosa più bella che mi sia mai capitata. Tu, in primis, hai assistito alle mie ultime sconfitte, ai miei dispiaceri, ma soprattutto hai contribuito ai miei successi: questo lavoro e queste fatiche non sarebbero mai volte al termine senza di te al mio fianco. Ogni volta che nella mia testa ho pensato di mollare, tu mi hai sempre spronato a combattere e a vincere, perché è questo che fa una squadra e noi due siamo la squadra più forte che esista.

Voglio ringraziare la mia Quark Family, composta da Jack, Marco, Carmine, Comby e Alfa, i quali hanno partecipato insieme a me a questa conquista. Voi, più di tutti, potete capire cosa vuol dire essere arrivati a questo traguardo. Ricordo ancora le risate,

i dispiaceri, i momenti di follia pre-esame, i pranzi dopo lezione, le serate a divertirci, i pomeriggi passati al telefono ad interrogarci riguardo all'esame del giorno successivo, le disperazioni, gli errori improponibili visualizzati dal terminale durante i vari laboratori di informatica... Mi avete affiancato passo dopo passo, standomi vicino anche in questi ultimi tempi, dove purtroppo, per cause avverse, abbiamo avuto poche occasioni di vederci. A chi di voi, come me, ha già raggiunto questo traguardo, faccio i miei complimenti e auguro il meglio per il futuro, mentre a chi sta lavorando duro per arrivarci auguro il mio più grande in bocca al lupo, che l'interazione forte tra quarks sia con voi!

Voglio ringraziare tutti i miei amici, quelli di TGIF, quelli del Team B., in particolare Fenko, Enri, Edo, Fra, Chiapps, Coatz, Dave, Fillo, Ale Goti, Frenk, Gullo, Nico, Marti, Anna, Silvia, Samu, Vale, Gianca, Ciccio, Fox, Gala, Geo, Gigi, Grox, Pio, Tommy e Paolo e tutti gli altri che mi hanno accompagnato, alcuni sin dall'inizio, altri da poco dopo, in questo lungo cammino. Anche se non avete partecipato direttamente al mio percorso, avete sempre ascoltato le mie storie e mi siete sempre stati accanto, perchè è questo che fanno i veri amici: accompagnarti sempre nei successi e nei fallimenti, senza abbandonarti mai.

Voglio ringraziare anche tutti gli altri miei parenti, in particolare i miei nonni, che mi hanno sostenuto sin da quando sono nato e mi hanno anche loro cresciuto, rendendomi ciò che sono ora. Ricordo ancora quando dissi a miei nonni Luciano e Cocchi per la prima volta che avevo deciso di iscrivermi a fisica: i loro occhi si illuminarono, pieni di stupore e curiosità. Siete tra le persone che più credono in me, mi avete sempre saputo ascoltare, anche quando gli argomenti che vi raccontavo erano incomprensibili, perchè mi avete sempre amato, sin dal primo giorno della mia vita. Ringrazio tanto anche il mio nonno Isidoro, che purtroppo non riesco a vedere spesso a causa della distanza che ci separa. Anche se abitiamo in due città differenti, ho sempre sentito il tuo supporto e la tua vicinanza, proprio come se fossi sempre stato accanto a me. Ringrazio ovviamente anche tutte le mie cugine e i miei zii per avermi sempre supportato.

Voglio ringraziare molto anche il team di ATLAS di Bologna che ha reso possibile questa esperienza e che mi ha insegnato davvero tanto sotto qualsiasi punto di vista. In particolare ringrazio ovviamente il mio relatore, il prof. Maximiliano Sioli, che mi ha introdotto nel mondo della ricerca e mi ha fornito questa opportunità unica di crescita ed esperienza, e naturalmente il mio correlatore, il dott. Marino Romano, che mi ha affiancato durante tutto lo sviluppo di questo elaborato, insegnandomi cosa vuol dire fare ricerca e quanto sia importante la dedizione e la determinazione a risolvere i problemi.

Voglio ringraziare anche i Bar Giants, in particolare il mio amico Jack, che ha contribuito a non farmi mai perdere la motivazione e la determinazione nello sport e nell'allenamento, altra parte fondamentale della mia vita, aiutandomi a conciliarlo mentalmente con lo studio e il lavoro. Ringrazio anche i miei amici della palestra, tra cui Lello, Nathan e Matte, per non avermi mai fatto perdere la voglia di raggiungere i miei obiettivi in questi anni di duro lavoro.

Ringrazio anche tutti gli altri miei amici dell'università, tra cui Simo, Ceci, Beppe,

Cesare, Lore, Margo e Michi e tutti quelli del corso di fisica nucleare subnucleare per avermi, anche loro, affiancato sin dall'inizio del mio percorso.

Infine ringrazio chiunque altro abbia creduto in me, perché nel suo piccolo avrà probabilmente contribuito a spronarmi a diventare quello che sono ora.

# List of Figures

1.1	Fundamental particles of the SM with some of their properties. . . . .	5
1.2	In (a): example of an EM interaction between an electron and a positron through the exchange of a photon. In (b): Triple vertex diagram with photons are not allowed in QED. . . . .	6
1.3	Feynman representation of the $\beta$ -decay of the neutron: $n \rightarrow p + e^- + \bar{\nu}_e$ . . . . .	8
1.4	Allowed vertices in QFD theory. . . . .	9
1.5	Allowed vertices in the QCD theory. . . . .	10
1.6	Production of $t\bar{t}$ via $q\bar{q}$ annihilation. . . . .	11
1.7	Examples of CC and NC allowed electroweak processes. In (a): NC vertex of a generic fermion $f$ . In (b): CC vertex of a generic lepton $l^-$ and the corresponding neutrino $\nu_l$ . . . . .	13
1.8	Example of decay channel of $t$ quark into $W^+$ and $b$ with subsequent decay: $W^+ \rightarrow l^+ \nu_l$ . . . . .	15
1.9	Quark masses $m$ and their absolute and relative uncertainties $\Delta m/m$ , indicated by vertical size of the error bands. . . . .	16
1.10	Plot of $m_W$ vs $m_t$ . In figure the 68% and 95% CL contours for the indirect determination of $m_t$ and $m_W$ from global SM fits to EW precision data are shown [9]. . . . .	17
1.11	Illustration of the impossibility of the $W$ boson from the decay of the $t$ to be right-handed (referred to helicity). . . . .	17
1.12	Radiative corrections from the top quark of higher order of the bosonic propagator of $W$ . . . . .	18
1.13	Regions of absolute stability, meta-stability and instability of the SM vacuum in the $m_t$ vs $m_h$ (Higgs boson mass) plane. The gray areas denote the allowed region at 1, 2, and 3 $\sigma$ . . . . .	19
1.14	Production of $t\bar{t}$ pair at the LHC, through gluon-gluon fusion. . . . .	20
1.15	Alternative diagrams for the $t\bar{t}$ production process through gluon-gluon fusion at the LHC. . . . .	22
1.16	The NNPDF3.1 NNLO PDFs, evaluated at $\mu^2 = 10^4 \text{GeV}^2$ [15]. . . . .	22

1.17	Summary of LHC and Tevatron measurements for the $t\bar{t}$ production cross-section as a function of the centre-of-mass energy compared to the NNLO QCD calculation complemented with NNLL resummation (2019) [16]. . . . .	24
1.18	$Wt$ channel single-top production process at the LHC at LO. . . . .	24
1.19	Example of NLO diagram contributions to the $tWb$ single-top production. . . . .	25
1.20	Summary of the ATLAS and CMS Collaborations measurements of the single top production cross-sections in the $t$ -channel at 13 TeV center-of-mass energy. The measurements are compared with a theoretical calculation based on NLO QCD, computed assuming a top mass of 172.5 GeV [16]. . . . .	27
1.21	Single-top control region (STCR1). Data are compared to the background after the simultaneous fit on the $\Delta R(b_1, b_2)$ distribution. To increase the purity of $Wt$ events, a cut is applied, in order to take events only for $\Delta R(b_1, b_2) > 1.2$ . Label $L$ stands for <i>lepton</i> , $\tau$ for <i>hadronic decay</i> , $1L$ $1\tau$ for <i>semileptonic decay</i> and $V$ for <i>vector boson</i> . . . . .	30
1.22	Normalized differential cross-section as a function of the $m_{bl}^{\text{minimax}}$ , compared with different theoretical models of the $t\bar{t} + tWb$ signal with various interference effects. Uncertainties of each data point include all statistical and systematic sources, while uncertainties for each of the MC predictions corresponds to theoretical ones. . . . .	31
1.23	On the left the differential DR, LS and LO distributions as a function of $p_T^L$ are reported. On the right, the integrals of the same distributions, divided by the respective total rates are shown. Results are relevant for $p_T^{\text{veto}} = 10$ GeV. . . . .	32
2.1	A diagram showing the complete structure of the LHC facility at CERN. There are the 4 main experiments (ATLAS, CMS, LHCb and ALICE) and the small accelerators that feed protons into the collider (PS, SPS, LINAC 2 and Booster) [23]. . . . .	34
2.2	Minimal layout of the LHC structure: there are 8 interaction points (IPs) in total, which only 4 of them host the detectors (ATLAS, CMS, ALICE and LHCb). Beam 1 and beam 2 are circulating in opposite direction to encourage collisions [25]. . . . .	35
2.3	Figure (a): total integrated luminosity collected by ATLAS in Run-2. Figure (b): recorded luminosity as a function of the number of interactions per crossing in each year of Run-2 [27]. . . . .	37
2.4	Cross-section of an LHC magnet. It consists of the following parts: (1) heat exchanger pipe, (2) superconducting busbars, (3) superconducting coils, (4) beam screen, (5) vacuum vessel, (6) radiation screen, (7) shrinking cylinder, (8) thermal shield, (9) non magnetic collars and (10) iron yoke [28]. . . . .	38

2.5	View of the main components of the ATLAS detector. The dimensions are 25 m in height $\times$ 44 m in length. It is composed by: muon chambers, toroid magnets, solenoid magnet, tracker system (pixel detector, semiconductor tracker and transition radiation tracker), liquid Argon electromagnetic and hadronic calorimeters and tile calorimeters. . . . .	40
2.6	Graphical representation of the right-handed Cartesian reference frame: the x-axis is pointing towards the center of the LHC, the y-axis is pointing upwards and the z-axis is tangent to the beam line. The angles $\phi$ and $\theta$ are respectively the azimuthal angle from the x-axis in the transverse plane and the polar angle measured from the z-axis in the x-y longitudinal plane. Furthermore, $\vec{p}$ is the momentum and $p_T$ its transverse component. . . . .	42
2.7	Pseudo-rapidity in function of the polar angle $\theta$ . . . . .	43
2.8	Geometrical representation of the magnet system. It is formed by: barrel toroids, solenoid and two end-cap toroids. The eight barrel toroid coils, with the end-cap coils interleaved are visible. The solenoid winding lies inside the calorimeter volume [33]. . . . .	44
2.9	Layout of the ATLAS Inner Detector. It is formed by: semiconductor tracker, transition radiation tracker and pixel detectors. . . . .	45
2.10	Cut-away view of the ATLAS calorimetry. EM calorimeter is divided into a barrel part and two end-caps components. HAD calorimeter is composed by tile, end-cap and forward calorimeter regions [34]. . . . .	47
2.11	Cut-away view of the ATLAS muon spectrometer. It is composed by: monitored drift tubes (MDTs), cathode strip chambers (CSC), resistive plate chambers (RPCs) and thin gap chambers (TGCs). It has also a barrel and an end-cap toroid. Its dimensions are: 24 m in diameter by 44 m in lenght. . . . .	48
2.12	Block diagram of the ATLAS TDAQ system. It is possible to see the two-stage trigger system (L1 and HLT) and the detector read-out with data flow. . . . .	50
3.1	Schematic view of the path of an electron through the detector. The red line is the hypothetical trajectory of an electron, traversing first the tracking system and then entering the EMCAL. The dashed line indicates the path of a photon produced via bremsstrahlung in the tracking system [41]. . . . .	53
3.2	Measured LH electron-identification efficiencies in $Z \rightarrow ee$ events for the Loose, Medium and Tight operating points, as a function of $E_T$ and $\eta$ . Vertical bars represent the statistical and total uncertainties. Bottom panel shows the data-to-simulation ratios. . . . .	55

3.3	LH electron-identification efficiencies for electron candidates with $E_T > 30$ GeV for the Loose, Medium and Tight operating points, as a function of primary vertices in the 2016 data taking, using the $Z \rightarrow ee$ process. The histogram shows the distribution of the number of primary vertices for the data. Inner uncertainties are statistical, while the total ones include both statistical and systematics components. Bottom panel shows the data-to-simulation ratios. . . . .	56
3.4	Sketch of the calorimeter isolation method: the grid represents the second-layer calorimeter cells in the $\eta$ and $\phi$ directions. The electron candidate is located in the center of the purple circle representing the isolation cone. All topological clusters are represented in red. The yellow-rectangled cells correspond to the subtracted cells in the core subtraction method (subtraction of the core energy around the candidate). . . . .	57
3.5	Scheme of all the reconstructed muon candidates [45]. . . . .	60
3.6	Left: distribution of the track based relative isolation variable. Right: distribution of the calorimeter-based relative isolation variable. Variables are measured in $Z \rightarrow \mu\mu$ events. Muons included in the plots satisfy Medium identification criteria and are well separated from the other muon from the $Z$ boson, that have $\Delta R_{\mu\mu} > 0.3$ . Bottom panel shows the ratio to data to simulation. Dots show the distribution of data, while histograms show distribution from simulation. . . . .	62
3.7	Absolute efficiencies for muons with respect to the offline muon $p_T$ in the barrel ( $ \eta  < 1.05$ , left panel) and endcap ( $1.05 <  \eta  < 2.4$ , right panel) regions. Relative efficiency of the HLT with respect to L1 is superimposed in the plots with blue line. . . . .	63
3.8	Muon trigger efficiency in the barrel region as a function of the number of reconstructed vertices. Efficiencies of L1, HLT and the total efficiency are shown for offline muons reconstructed in the barrel region with $p_T > 27$ GeV. . . . .	63
3.9	L1 (red dots) and HLT (blue triangles) online tau identification efficiency for tau candidates identified by the offline Medium tau identification, as a function of the offline $p_T$ (left) and the number of primary vertices (right). Error bars correspond to statistical uncertainties. . . . .	65
3.10	Single-jet trigger efficiencies for L1 and HLT for central and forward regions of the calorimeter, as a function of offline jet $p_T$ for: (a) L1 in central region, (b) L1 in the forward region, (c) HLT in the central region and (d) HLT in the forward region. . . . .	68
3.11	TST $E_T^{\text{miss}}$ resolution as a function of the number of primary vertices, measured in MC simulated $Z \rightarrow \mu\mu$ events using different strategies for pile-up suppression. . . . .	70

- 3.12  $E_T^{\text{miss}}$  trigger efficiency curves with respect to the  $E_T^{\text{miss}}$  reconstructed offline without muon corrections for all events passing the (a)  $W \rightarrow e\nu$  or (b)  $W \rightarrow \mu\nu$  selections. Different efficiencies were measured for L1 and for combinations of L1 with each of the HLT  $E_T^{\text{miss}}$  algorithms. . . . . 71
- 4.1 Kinematic distributions in the  $e\mu$  channel at detector-level: (upper left) leading  $b$ -jet  $p_T$  and (upper right) pseudorapidity and (lower left) sub-leading  $b$ -jet  $p_T$  and (lower right) pseudorapidity. Data distributions are compared with predictions using POWHEG + PYTHIA 8 as the  $t\bar{t}$  signal model and both POWHEG + PYTHIA 8 DR and DS for the  $tW$  signal model. The hatched area represents the combined statistical and systematic uncertainties (described in Section 4.6) in the total prediction, including only systematic uncertainties of the scale factors. Underflow and overflow events, if any, are included in the first and last bins. The lower panels show the ratio of the data to the total prediction obtained with both DR and DS schemes for the  $tW$  modelling. . . . . 78
- 4.2 Kinematic distributions in the  $e\mu$  channel at detector-level: (upper left) leading lepton  $p_T$  and (upper right) pseudorapidity and (lower left) subleading lepton  $p_T$  and (lower right) pseudorapidity. Data distributions are compared with predictions using POWHEG + PYTHIA 8 as the  $t\bar{t}$  signal model and both POWHEG + PYTHIA 8 DR and DS for the  $tW$  signal model. The hatched area represents the combined statistical and systematic uncertainties (described in Section 4.6) in the total prediction, including only systematic uncertainties of the scale factors. Underflow and overflow events, if any, are included in the first and last bins. The lower panels show the ratio of the data to the total prediction obtained with both DR and DS schemes for the  $tW$  modelling. . . . . 79
- 4.3 Kinematic distributions in the  $e\mu$  channel at detector-level: (upper left)  $E_T^{\text{miss}}$ , (upper right) number of extra jets, (lower left)  $H_{l_1 l_2}^T$  and (lower right)  $\Delta R_{l_1 l_2}$ . Data distributions are compared with predictions using POWHEG + PYTHIA 8 as the  $t\bar{t}$  signal model and both POWHEG + PYTHIA 8 DR and DS for the  $tW$  signal model. The hatched area represents the combined statistical and systematic uncertainties (described in Section 4.6) in the total prediction, including only systematic uncertainties of the scale factors. Underflow and overflow events, if any, are included in the first and last bins. The lower panels show the ratio of the data to the total prediction obtained with both DR and DS schemes for the  $tW$  modelling. . . . . 80

4.4	Kinematic distributions in the $e\mu$ channel at detector-level: (left) $m_{bl}^{\minimax}$ and (right) $\Delta R(b_1, b_2)$ . Data distributions are compared with predictions using POWHEG + PYTHIA 8 as the $t\bar{t}$ signal model and both POWHEG + PYTHIA 8 DR and DS for the $tW$ signal model. The hatched area represents the combined statistical and systematic uncertainties (described in Section 4.6) in the total prediction, including only systematic uncertainties of the scale factors. Underflow and overflow events, if any, are included in the first and last bins. The lower panels show the ratio of the data to the total prediction obtained with both DR and DS schemes for the $tW$ modelling. . . . .	81
4.5	A scheme demonstrating the assignment of the leptons and $b$ -jets to form the $m_{bl}^{\minimax}$ variable. Two possible pairings are considered: the <b>A-type</b> and the <b>B-type</b> and for each of them one can build two possible $m_{bl}$ values. The minimum of the larger $m_{bl}$ values from each pairing is selected as $m_{bl}^{\minimax}$ . In $t\bar{t}$ events this choice has a kinematic endpoint at $m_{bl}^{\minimax} < \sqrt{m_t^2 - m_W^2}$ while for single-top events there is no such bound. . . . .	83
4.6	Mean and RMS of the resolution distributions for $m_{bl}^{\minimax}$ as a function of the particle-level $m_{bl}^{\minimax}$ in bins of $\Delta R(b_1, b_2)$ in the DR scheme. . . . .	89
4.7	Mean and RMS of the resolution distributions for $m_{bl}^{\minimax}$ as a function of the particle-level $m_{bl}^{\minimax}$ in bins of $\Delta R(b_1, b_2)$ in the DS scheme. . . . .	91
4.8	Closure tests for the particle-level normalized differential cross-sections as a function of: $m_{bl}^{\minimax}$ in logarithmic scale (left) and $\Delta R(b_1, b_2)$ in linear scale (right). These distributions are unfolded with <code>half1</code> , using <code>half0</code> as pseudo-data. Black dots represent the unfolded pseudo-data, red line represents the prediction of <code>half0</code> , green line is the prediction of <code>half1</code> , the orange band indicates the statistical uncertainties, while the yellow band the statistical + systematic ones. $p$ -value is referred to the <code>half0</code> sample. . . . .	92
4.9	Left: 2D closure tests for the particle-level normalized differential cross-sections as a function of $m_{bl}^{\minimax}$ in bins of $\Delta R(b_1, b_2)$ . This distribution is unfolded with <code>half1</code> , using <code>half0</code> as pseudo-data. Data points are placed in the center of each bin. Red line represents the prediction. Right: ratio plot of the measured cross-section to different MC predictions; black line represents the pseudo-data, red line represents the prediction of <code>half0</code> , green line is the prediction of <code>half1</code> , the orange band indicates the statistical uncertainties, while the yellow band the statistical + systematic ones. . . . .	93

4.10	Fractional uncertainties in the particle-level normalized differential cross-sections as a function of: (left) $m_{bl}^{\minimax}$ and (right) $\Delta R(b_1, b_2)$ . The black line represents the flavour tagging uncertainty, purple line is the DS/DR uncertainty, purple dotted line is the MC statistical uncertainty, red line is the JVT uncertainty, red dotted line is the lepton uncertainty, orange band is the statistical uncertainty and yellow band represents the statistical + systematic one. . . . .	96
4.11	Fractional uncertainties in the particle-level normalized differential cross-section as a function of the 2D $m_{bl}^{\minimax}$ in bins of $\Delta R(b_1, b_2)$ . The black line represents the flavour tagging uncertainty, purple dotted line is the DS/DR uncertainty, red line is the JES/JER uncertainty, red dotted line is the lepton uncertainty, orange band is the statistical uncertainty and yellow band represents the statistical + systematic one. . . . .	97
4.12	Particle-level normalized differential cross-section as a function of: (upper left) $m_{bl}^{\minimax}$ and (upper right) $\Delta R(b_1, b_2)$ in linear scale. The black dots represent the data, red line is the PWG+PY8 $t\bar{t} + tW$ MC prediction in the DR scheme, purple dotted line is the PWG+PY8 $t\bar{t} + tW$ MC prediction in the DS scheme, orange band represents the statistical uncertainty and yellow band the statistical + systematic one. The ratio plot below shows the prediction over data ratio. In the lower left and right panels it is possible to observe the logarithmic scale distributions. . . . .	99
4.13	Left: Particle-level normalized differential cross-section as a function of 2D $m_{bl}^{\minimax}$ in bins of $\Delta R(b_1, b_2)$ in the resolved topology compared with the prediction obtained with the POWHEG + PYTHIA8 MC generator. Data points are placed to the center of each bin. Red line represents the prediction. Right: ratio plot of the measured cross-section to different MC predictions; black line represents the data, red line represents the PWG+PY8 $t\bar{t} + tW$ MC prediction in the DR scheme, purple dotted line is the PWG+PY8 $t\bar{t} + tW$ MC prediction in the DS scheme, the orange band indicates the statistical uncertainties, while the yellow band the statistical + systematic ones. . . . .	100
A.1	Schematic view of $p$ - $p(\bar{p})$ collision [94]. . . . .	105
B.1	$H_T$ triggers efficiency as a function of offline $H_T$ (a) and large- $R$ single-jet triggers as a function of offline $p_T$ (b). . . . .	107
B.2	The multi-jet trigger efficiencies for L1 (a) and HLT (b) triggers as a function of offline jet $p_T$ . . . . .	108

C.1	Illustration of the impact parameters of a track in the transverse plane (left) and RZ-plane (right), as defined in the global ATLAS tracking frame [98]: $\phi_0$ is the angle with the x-axis in the X-Y plane at the impact point, $\theta$ is the angle with the z-axis in the R-Z plane, $p$ is the momentum and $p_T$ the transverse component. . . . .	110
C.2	$d_0$ and $z_0 \sin \theta$ impact parameters distributions for <b>electrons</b> coming from $\tau$ or $W$ . The $\tau/W$ plot shows the ratio between lepton events coming from $\tau$ and $W$ respectively. . . . .	111
C.3	$d_0$ and $z_0 \sin \theta$ impact parameters distributions for <b>muons</b> coming from $\tau$ or $W$ . The $\tau/W$ plot shows the ratio between lepton events coming from $\tau$ and $W$ respectively. . . . .	111
C.4	$d_0$ and $z_0 \sin \theta$ impact parameters distributions for electrons and muons coming from $\tau$ or $W$ . The $\tau/W$ plot shows the ratio between lepton events coming from $\tau$ and $W$ respectively. . . . .	112
C.5	2D impact parameters plots for leptons coming from $\tau$ or $W$ . Plots are in logarithmic scale for the $z$ axis. . . . .	113
C.6	Mean and RMS of the resolution distributions for $\Delta R(b_1, b_2)$ as a function of the particle-level $\Delta R(b_1, b_2)$ in bins of $m_{bl}^{\text{minimax}}$ for the $t\bar{t}$ sample. . . .	114
C.7	Mean and RMS of the resolution distributions for $m_{bl}^{\text{minimax}}$ as a function of the particle-level $m_{bl}^{\text{minimax}}$ in bins of $\Delta R(b_1, b_2)$ for the $t\bar{t}$ sample. . . .	115
C.8	Mean and RMS of the resolution distributions for $\Delta R(b_1, b_2)$ as a function of the particle-level $\Delta R(b_1, b_2)$ in bins of $m_{bl}^{\text{minimax}}$ for the $tW$ sample in the DR scheme. . . . .	115
C.9	Mean and RMS of the resolution distributions for $m_{bl}^{\text{minimax}}$ as a function of the particle-level $m_{bl}^{\text{minimax}}$ in bins of $\Delta R(b_1, b_2)$ for the $tW$ sample in the DR scheme. . . . .	116
C.10	Mean and RMS of the resolution distributions for $\Delta R(b_1, b_2)$ as a function of the particle-level $\Delta R(b_1, b_2)$ in bins of $m_{bl}^{\text{minimax}}$ for the $tW$ sample in the DS scheme. . . . .	116
C.11	Mean and RMS of the resolution distributions for $m_{bl}^{\text{minimax}}$ as a function of the particle-level $m_{bl}^{\text{minimax}}$ in bins of $\Delta R(b_1, b_2)$ for the $tW$ sample in the DS scheme. . . . .	117
C.12	Mean and RMS of the resolution distributions for $\Delta R(b_1, b_2)$ as a function of the particle-level $\Delta R(b_1, b_2)$ in bins of $m_{bl}^{\text{minimax}}$ in the DR scheme. . . .	119
C.13	Mean and RMS of the resolution distributions for $\Delta R(b_1, b_2)$ as a function of the particle-level $\Delta R(b_1, b_2)$ in bins of $m_{bl}^{\text{minimax}}$ in the DS scheme. . . .	119



# List of Tables

1.1	Representation of the 4 fundamental forces mediators. The spin is reported in multiples of $\hbar$ , the mass in $\text{GeV}/c^2$ . . . . .	4
2.1	General performance goals of the ATLAS detector: the required resolution and the $\eta$ coverage (for measurement and trigger) of each main component of the ATLAS experiment are shown. . . . .	44
4.1	Observed and expected number of events after the full event selection. The uncertainties for the $t\bar{t}$ and $tW$ samples include the uncertainties on the scale factors (see Section 4.6) and the MC statistics. The uncertainties for the background samples include only the MC statistics. . . . .	77
4.2	Requirements for binning and chosen bins for $m_{bl}^{\min\max}$ and $\Delta R_{b_1 b_2}$ in the case of 1D and 2D external variables. For $\Delta R_{b_1 b_2}$ the $\delta$ value is basically irrelevant since we are dominated by statistics. . . . .	89
4.3	Requirements for binning and chosen bins for $m_{bl}^{\min\max}$ in bins of $\Delta R_{b_1 b_2}$ in the case of 2D internal variables. . . . .	90
4.4	Total fiducial $t\bar{t} + tWb$ cross-section in the $e\mu$ channel. The uncertainty on the measurements is due to the data statistics, the scale factor uncertainties and the interference removal scheme, as described in Section 4.6. The uncertainty on the POWHEG + PYTHIA8 predictions is based on the MC statistics only. . . . .	98
C.1	Requirements for binning and chosen bins for $\Delta R_{b_1 b_2}$ in bins of $m_{bl}^{\min\max}$ in the case of 2D internal variables. . . . .	118

# Bibliography

- [1] Mark Thomson. *Modern particle physics*. New York: Cambridge University Press, 2013. ISBN: 978-1-107-03426-6.
- [2] S. Braibant, G. Giacomelli, and M. Spurio. *Particelle e interazioni fondamentali: Il mondo delle particelle*. UNITEXT. Springer Milan, 2010. ISBN: 9788847011618. URL: <https://books.google.it/books?id=6YKRe94BTKAC>.
- [3] Tanabashi et al. “Review of Particle Physics”. In: *Phys. Rev. D* 98 (3 Aug. 2018), p. 030001. DOI: [10.1103/PhysRevD.98.030001](https://doi.org/10.1103/PhysRevD.98.030001). URL: <https://link.aps.org/doi/10.1103/PhysRevD.98.030001>.
- [4] Joshua P. Ellis. “TikZ-Feynman: Feynman diagrams with TikZ”. In: *Computer Physics Communications* 210 (2017), pp. 103–123. ISSN: 0010-4655. DOI: <https://doi.org/10.1016/j.cpc.2016.08.019>. URL: <http://www.sciencedirect.com/science/article/pii/S0010465516302521>.
- [5] C. Quigg. *Gauge Theories of the Strong, Weak and Electromagnetic Interactions*. Vol. 56. 1983. ISBN: 978-0-8053-6020-2.
- [6] Antonio Pich. “The Standard model of electroweak interactions”. In: *2006 European School of High-Energy Physics*. 2008, pp. 1–49. arXiv: [0705.4264 \[hep-ph\]](https://arxiv.org/abs/0705.4264).
- [7] Arnulf Quadt. “Top quark physics at hadron colliders”. In: *Eur. Phys. J. C* 48 (2006), pp. 835–1000. DOI: [10.1140/epjc/s2006-02631-6](https://doi.org/10.1140/epjc/s2006-02631-6).
- [8] Martin C. Smith and Scott S. Willenbrock. “Top-quark pole mass”. In: arXiv:hep-ph/9612329. 1997. DOI: [10.1103/PhysRevLett.79.3825](https://doi.org/10.1103/PhysRevLett.79.3825).
- [9] Giorgio Cortiana. “Top-quark mass measurements: Review and perspectives”. In: *Reviews in Physics* 1 (2016), pp. 60–76. ISSN: 2405-4283. DOI: <https://doi.org/10.1016/j.revip.2016.04.001>. URL: <http://www.sciencedirect.com/science/article/pii/S2405428316300028>.
- [10] *First combination of Tevatron and LHC measurements of the top-quark mass*. Tech. rep. ATLAS-CONF-2014-008. ATLAS-CONF-2014-008. CDF-NOTE-11071. CMS-PAS-TOP-13-014. D0-NOTE-6416. Work within the Tevatron Electroweak (TEV-EW-WG) and the Top Physics LHC (TOP-LHC-WG) working groups. Geneva: CERN, Mar. 2014. URL: <https://cds.cern.ch/record/1669819>.

- [11] Jens Erler and Matthias Schott. “Electroweak Precision Tests of the Standard Model after the Discovery of the Higgs Boson”. In: *Prog. Part. Nucl. Phys.* 106 (2019), pp. 68–119. DOI: [10.1016/j.ppnp.2019.02.007](https://doi.org/10.1016/j.ppnp.2019.02.007). arXiv: [1902.05142 \[hep-ph\]](https://arxiv.org/abs/1902.05142).
- [12] Giuseppe Degrassi et al. “Higgs mass and vacuum stability in the Standard Model at NNLO”. In: *Journal of High Energy Physics* 2012 (May 2012). DOI: [10.1007/JHEP08\(2012\)098](https://doi.org/10.1007/JHEP08(2012)098).
- [13] Michele Gallinaro. “Top quark physics: A tool for discoveries”. In: *Journal of Physics: Conference Series* 447 (July 2013), p. 012012. DOI: [10.1088/1742-6596/447/1/012012](https://doi.org/10.1088/1742-6596/447/1/012012). URL: <https://doi.org/10.1088%2F1742-6596%2F447%2F1%2F012012>.
- [14] Morad Aaboud et al. “Probing the quantum interference between singly and doubly resonant top-quark production in  $pp$  collisions at  $\sqrt{s} = 13$  TeV with the ATLAS detector”. In: *Phys. Rev. Lett.* 121.15 (2018), p. 152002. DOI: [10.1103/PhysRevLett.121.152002](https://doi.org/10.1103/PhysRevLett.121.152002). arXiv: [1806.04667 \[hep-ex\]](https://arxiv.org/abs/1806.04667).
- [15] Richard D. Ball et al. “Parton distributions from high-precision collider data.” In: *Eur. Phys. J. C* 77.CAVENDISH-HEP-17-06. 10 (June 2017), 663. 95 p. DOI: [10.1140/epjc/s10052-017-5199-5](https://doi.org/10.1140/epjc/s10052-017-5199-5). URL: <https://cds.cern.ch/record/2267455>.
- [16] CERN (Conseil Européen pour la Recherche Nucléaire). URL: <https://twiki.cern.ch/twiki/bin/view/LHCPhysics/LHCTopWGSummaryPlots>. (accessed: 22.05.2020).
- [17] F. Cascioli et al. “A unified NLO description of top-pair and associated Wt production”. In: *The European Physical Journal C* 74.3 (Mar. 2014). ISSN: 1434-6052. DOI: [10.1140/epjc/s10052-014-2783-9](https://doi.org/10.1140/epjc/s10052-014-2783-9). URL: <http://dx.doi.org/10.1140/epjc/s10052-014-2783-9>.
- [18] Stefano Frixione et al. “Single-top hadroproduction in association with aWboson”. In: *Journal of High Energy Physics* 2008.07 (July 2008), pp. 029–029. DOI: [10.1088/1126-6708/2008/07/029](https://doi.org/10.1088/1126-6708/2008/07/029). URL: <https://doi.org/10.1088%2F1126-6708%2F2008%2F07%2F029>.
- [19] Shouhua Zhu. “Next-to-leading order QCD corrections to  $b\bar{g} \rightarrow t\bar{W}$ — at the CERN Large Hadron Collider”. In: *Physics Letters B* 524.3 (2002), pp. 283–288. ISSN: 0370-2693. DOI: [https://doi.org/10.1016/S0370-2693\(01\)01404-6](https://doi.org/10.1016/S0370-2693(01)01404-6). URL: <http://www.sciencedirect.com/science/article/pii/S0370269301014046>.
- [20] Chris D. White et al. “Isolating Wt production at the LHC”. In: *Journal of High Energy Physics* 2009 (2009), p. 074.

- [21] The ATLAS Collaboration. “Search for top squarks in final states with one isolated lepton, jets, and missing transverse momentum in  $s = 13$  TeV pp collisions with the ATLAS detector”. In: *Physical Review D* 94.5 (2016). ISSN: 2470-0010. DOI: [10.1103/PhysRevD.94.052009](https://doi.org/10.1103/PhysRevD.94.052009).
- [22] CERN (Conseil Européen pour la Recherche Nucléaire). URL: <https://home.cern/>. (accessed: 12.04.2020).
- [23] Alexander Gude. “Measurement of the phistar distribution of Z bosons decaying to electron pairs with the CMS experiment at a center-of-mass energy of 8 TeV”. PhD thesis. May 2015.
- [24] Lyndon Evans and Philip Bryant. “The CERN Large Hadron Collider: Accelerator and Experiments”. In: *JINST* 3 S08001 (2008).
- [25] X. Buffat et al. “Stability diagrams of colliding beams in the Large Hadron Collider”. In: *Physical Review Special Topics - Accelerators and Beams* 17 (Nov. 2014). DOI: [10.1103/PhysRevSTAB.17.111002](https://doi.org/10.1103/PhysRevSTAB.17.111002).
- [26] Ewa Stanecka and on Collaboration. “The ATLAS Inner Detector operation, data quality and tracking performance”. In: *Proceedings of 32nd International Symposium on Physics in Collision, PIC 2012* (Mar. 2013). arXiv: [1303.3630v1](https://arxiv.org/abs/1303.3630v1).
- [27] ATLAS Collaboration. *ATLAS data quality operations and performance for 2015-2018 data-taking*. Tech. rep. arXiv:1911.04632. Geneva: CERN, Nov. 2019. URL: <https://cds.cern.ch/record/2700249>.
- [28] Rafal Noga. “Modeling and control of the String2 LHC Prototype at CERN”. PhD thesis. Sept. 2007.
- [29] Helmut Wiedemann. *Particle Accelerator Physics*. Springer, 2015.
- [30] K. Schindl. “The injector chain for the LHC”. In: *LEP performance. Proceedings, 9th Workshop, Chamonix, France, January 26-29, 1999*. Mar. 1999, pp. 47–52.
- [31] The ATLAS collaboration et al. “The ATLAS experiment at the CERN Large Hadron Collider”. In: *JINST* 3 S08003 (2008).
- [32] David E Baynham et al. “ATLAS end cap toroid magnets cryostat design, manufacture and integration at CERN”. In: *Applied Superconductivity, IEEE Transactions on* 14 (July 2004), pp. 522–525. DOI: [10.1109/TASC.2004.829710](https://doi.org/10.1109/TASC.2004.829710).
- [33] Benjamin Pearson. “Searches for a high-mass Higgs-like diboson resonance in the  $H \rightarrow WW \rightarrow \ell\nu qq$  decay channel using  $pp$  collisions at both  $\sqrt{s} = 8$  and 13 TeV with the ATLAS detector at the LHC”. PhD thesis. Oklahoma U., 2016.
- [34] Fabian Kuger. “Signal Formation Processes in Micromegas Detectors and Quality Control for large size Detector Construction for the ATLAS New Small Wheel”. In: (Aug. 2017).

- [35] P Strizenec. “Performance of the ATLAS Liquid Argon Calorimeter after three years of LHC, operation and plans for a future upgrade”. In: *Journal of Instrumentation* 9.09 (Sept. 2014), pp. C09007–C09007. DOI: [10.1088/1748-0221/9/09/c09007](https://doi.org/10.1088/1748-0221/9/09/c09007). URL: <https://doi.org/10.1088%2F1748-0221%2F9%2F09%2Fc09007>.
- [36] N C Benekos et al. “ATLAS muon spectrometer simulation and its validation algorithms”. In: *Journal of Physics: Conference Series* 119.3 (July 2008), p. 032009. DOI: [10.1088/1742-6596/119/3/032009](https://doi.org/10.1088/1742-6596/119/3/032009). URL: <https://doi.org/10.1088%2F1742-6596%2F119%2F3%2F032009>.
- [37] ATLAS Collaboration. *Operation of the ATLAS trigger system in Run 2*. 2020. arXiv: [2007.12539 \[physics.ins-det\]](https://arxiv.org/abs/2007.12539).
- [38] ATLAS Collaboration. *Technical Design Report for the Phase-II Upgrade of the ATLAS TDAQ System*. Tech. rep. CERN-LHCC-2017-020. ATLAS-TDR-029. Geneva: CERN, Sept. 2017. URL: <https://cds.cern.ch/record/2285584>.
- [39] P. Calafiura et al. “The Athena control framework in production, new developments and lessons learned”. In: *14th International Conference on Computing in High-Energy and Nuclear Physics*. 2005, pp. 456–458.
- [40] The ATLAS Collaboration. “Electron reconstruction and identification in the ATLAS experiment using the 2015 and 2016 LHC proton-proton collision data at  $s=13$  TeV”. In: *The European Physical Journal C* 79 (Aug. 2019).
- [41] *Electron efficiency measurements with the ATLAS detector using the 2015 LHC proton-proton collision data*. Tech. rep. ATLAS-CONF-2016-024. Geneva: CERN, June 2016. URL: <https://cds.cern.ch/record/2157687>.
- [42] Leonor Alberich. “Photon and electron identification with the ATLAS detector”. In: *PoS ICHEP2016* (2017), p. 1235. DOI: [10.22323/1.282.1235](https://doi.org/10.22323/1.282.1235).
- [43] The ATLAS Collaboration. “Performance of electron and photon triggers in ATLAS during LHC Run 2”. In: *Eur. Phys. J. C* 80.arXiv:1909.00761. 1 (Sept. 2019), 47. 56 p. DOI: [10.1140/epjc/s10052-019-7500-2](https://doi.org/10.1140/epjc/s10052-019-7500-2). URL: <https://cds.cern.ch/record/2688248>.
- [44] The ATLAS Collaboration. “Muon reconstruction performance of the ATLAS detector in proton–proton collision data at  $\sqrt{s} = 13$  TeV”. In: *Eur. Phys. J. C* 76.5 (2016), p. 292. DOI: [10.1140/epjc/s10052-016-4120-y](https://doi.org/10.1140/epjc/s10052-016-4120-y). arXiv: [1603.05598 \[hep-ex\]](https://arxiv.org/abs/1603.05598).
- [45] Sebastien Rettie. *Muon identification and performance in the ATLAS experiment*. Tech. rep. ATL-PHYS-PROC-2018-052. Geneva: CERN, June 2018. DOI: [10.22323/1.316.0097](https://doi.org/10.22323/1.316.0097). URL: <https://cds.cern.ch/record/2626330>.
- [46] Andrea Ventura and ATLAS Collaboration. “ATLAS Muon Trigger Performance”. In: (Sept. 2019). URL: <https://cds.cern.ch/record/2688754>.

- [47] *Measurement of the tau lepton reconstruction and identification performance in the ATLAS experiment using pp collisions at  $\sqrt{s} = 13$  TeV*. Tech. rep. ATLAS-CONF-2017-029. Geneva: CERN, May 2017. URL: <https://cds.cern.ch/record/2261772>.
- [48] Steven Schramm. *ATLAS Jet Reconstruction, Calibration, and Tagging of Lorentz-boosted Objects*. Tech. rep. ATL-PHYS-PROC-2017-236. Geneva: CERN, Nov. 2017. URL: <https://cds.cern.ch/record/2291608>.
- [49] Marino Romano. “Measurement of the differential cross-section of  $t\bar{t}$  pairs in  $pp$  collisions at  $\sqrt{s} = 13$  TeV with the ATLAS detector at the LHC”. PhD thesis. Alma Mater Studiorum, 2013.
- [50] Aliaksei Hrynevich. *ATLAS jet and missing energy reconstruction, calibration and performance in LHC Run-2*. Tech. rep. ATL-PHYS-PROC-2017-045. 06. Geneva: CERN, May 2017. DOI: [10.1088/1748-0221/12/06/C06038](https://doi.org/10.1088/1748-0221/12/06/C06038). URL: <https://cds.cern.ch/record/2263777>.
- [51] Emanuele Re. “Single-top  $Wt$ -channel production matched with parton showers using the POWHEG method”. In: *Eur. Phys. J. C* 71 (2011), p. 1547. DOI: [10.1140/epjc/s10052-011-1547-z](https://doi.org/10.1140/epjc/s10052-011-1547-z). arXiv: [1009.2450 \[hep-ph\]](https://arxiv.org/abs/1009.2450).
- [52] Paolo Nason. “A new method for combining NLO QCD with shower Monte Carlo algorithms”. In: *JHEP* 11 (2004), p. 040. DOI: [10.1088/1126-6708/2004/11/040](https://doi.org/10.1088/1126-6708/2004/11/040). arXiv: [hep-ph/0409146](https://arxiv.org/abs/hep-ph/0409146).
- [53] Stefano Frixione, Paolo Nason, and Carlo Oleari. “Matching NLO QCD computations with parton shower simulations: the POWHEG method”. In: *JHEP* 11 (2007), p. 070. DOI: [10.1088/1126-6708/2007/11/070](https://doi.org/10.1088/1126-6708/2007/11/070). arXiv: [0709.2092 \[hep-ph\]](https://arxiv.org/abs/0709.2092).
- [54] Simone Alioli et al. “A general framework for implementing NLO calculations in shower Monte Carlo programs: the POWHEG BOX”. In: *JHEP* 06 (2010), p. 043. DOI: [10.1007/JHEP06\(2010\)043](https://doi.org/10.1007/JHEP06(2010)043). arXiv: [1002.2581 \[hep-ph\]](https://arxiv.org/abs/1002.2581).
- [55] Richard D. Ball et al. “Parton distributions for the LHC run II”. In: *JHEP* 04 (2015), p. 040. DOI: [10.1007/JHEP04\(2015\)040](https://doi.org/10.1007/JHEP04(2015)040). arXiv: [1410.8849 \[hep-ph\]](https://arxiv.org/abs/1410.8849).
- [56] Torbjörn Sjöstrand et al. “An introduction to PYTHIA 8.2”. In: *Comput. Phys. Commun.* 191 (2015), p. 159. DOI: [10.1016/j.cpc.2015.01.024](https://doi.org/10.1016/j.cpc.2015.01.024). arXiv: [1410.3012 \[hep-ph\]](https://arxiv.org/abs/1410.3012).
- [57] ATLAS Collaboration. *ATLAS Pythia 8 tunes to 7 TeV data*. ATL-PHYS-PUB-2014-021. 2014. URL: <https://cds.cern.ch/record/1966419>.
- [58] D. J. Lange. “The EvtGen particle decay simulation package”. In: *Nucl. Instrum. Meth. A* 462 (2001), p. 152. DOI: [10.1016/S0168-9002\(01\)00089-4](https://doi.org/10.1016/S0168-9002(01)00089-4).

- [59] Nikolaos Kidonakis. “Two-loop soft anomalous dimensions for single top quark associated production with a  $W^-$  or  $H^-$ ”. In: *Phys. Rev. D* 82 (2010), p. 054018. DOI: [10.1103/PhysRevD.82.054018](https://doi.org/10.1103/PhysRevD.82.054018). arXiv: [1005.4451 \[hep-ph\]](https://arxiv.org/abs/1005.4451).
- [60] Nikolaos Kidonakis. “Top Quark Production”. In: *Proceedings, Helmholtz International Summer School on Physics of Heavy Quarks and Hadrons (HQ 2013): JINR, Dubna, Russia, July 15-28, 2013*. 2014, pp. 139–168. DOI: [10.3204/DESY-PROC-2013-03/Kidonakis](https://doi.org/10.3204/DESY-PROC-2013-03/Kidonakis). arXiv: [1311.0283 \[hep-ph\]](https://arxiv.org/abs/1311.0283).
- [61] A. D. Martin et al. “Uncertainties on  $\alpha_S$  in global PDF analyses and implications for predicted hadronic cross sections”. In: *Eur. Phys. J. C* 64 (2009), pp. 653–680. DOI: [10.1140/epjc/s10052-009-1164-2](https://doi.org/10.1140/epjc/s10052-009-1164-2). arXiv: [0905.3531 \[hep-ph\]](https://arxiv.org/abs/0905.3531).
- [62] A. D. Martin et al. “Parton distributions for the LHC”. In: *Eur. Phys. J. C* 63 (2009), pp. 189–285. DOI: [10.1140/epjc/s10052-009-1072-5](https://doi.org/10.1140/epjc/s10052-009-1072-5). arXiv: [0901.0002 \[hep-ph\]](https://arxiv.org/abs/0901.0002).
- [63] Michal Czakon and Alexander Mitov. “Top++: A program for the calculation of the top-pair cross-section at hadron colliders”. In: *Comput. Phys. Commun.* 185 (2014), p. 2930. DOI: [10.1016/j.cpc.2014.06.021](https://doi.org/10.1016/j.cpc.2014.06.021). arXiv: [1112.5675 \[hep-ph\]](https://arxiv.org/abs/1112.5675).
- [64] M. Beneke et al. “Hadronic top-quark pair production with NNLL threshold resummation”. In: *Nucl. Phys. B* 855 (2012), pp. 695–741. DOI: [10.1016/j.nuclphysb.2011.10.021](https://doi.org/10.1016/j.nuclphysb.2011.10.021). arXiv: [1109.1536 \[hep-ph\]](https://arxiv.org/abs/1109.1536).
- [65] Peter Bärnreuther, Michal Czakon, and Alexander Mitov. “Percent-Level-Precision Physics at the Tevatron: Next-to-Next-to-Leading Order QCD Corrections to  $q\bar{q} \rightarrow t\bar{t} + X$ ”. In: *Phys. Rev. Lett.* 109 (2012), p. 132001. DOI: [10.1103/PhysRevLett.109.132001](https://doi.org/10.1103/PhysRevLett.109.132001). arXiv: [1204.5201 \[hep-ph\]](https://arxiv.org/abs/1204.5201).
- [66] Michal Czakon and Alexander Mitov. “NNLO corrections to top pair production at hadron colliders: the quark-gluon reaction”. In: *JHEP* 01 (2013), p. 080. DOI: [10.1007/JHEP01\(2013\)080](https://doi.org/10.1007/JHEP01(2013)080). arXiv: [1210.6832 \[hep-ph\]](https://arxiv.org/abs/1210.6832).
- [67] Michal Czakon and Alexander Mitov. “NNLO corrections to top-pair production at hadron colliders: the all-fermionic scattering channels”. In: *JHEP* 12 (2012), p. 054. DOI: [10.1007/JHEP12\(2012\)054](https://doi.org/10.1007/JHEP12(2012)054). arXiv: [1207.0236 \[hep-ph\]](https://arxiv.org/abs/1207.0236).
- [68] Michal Czakon, Paul Fiedler, and Alexander Mitov. “Total Top-Quark Pair-Production Cross Section at Hadron Colliders Through  $O(\alpha_S^4)$ ”. In: *Phys. Rev. Lett.* 110 (2013), p. 252004. DOI: [10.1103/PhysRevLett.110.252004](https://doi.org/10.1103/PhysRevLett.110.252004). arXiv: [1303.6254 \[hep-ph\]](https://arxiv.org/abs/1303.6254).
- [69] Jon Butterworth et al. “PDF4LHC recommendations for LHC Run II”. In: *J. Phys. G* 43 (2016), p. 023001. DOI: [10.1088/0954-3899/43/2/023001](https://doi.org/10.1088/0954-3899/43/2/023001). arXiv: [1510.03865 \[hep-ph\]](https://arxiv.org/abs/1510.03865).

- [70] J. Gao et al. “CT10 next-to-next-to-leading order global analysis of QCD”. In: *Phys. Rev. D* 89 (2014), p. 033009. doi: [10.1103/PhysRevD.89.033009](https://doi.org/10.1103/PhysRevD.89.033009). arXiv: [1302.6246 \[hep-ph\]](https://arxiv.org/abs/1302.6246).
- [71] Richard D. Ball et al. “Parton distributions with LHC data”. In: *Nucl. Phys. B* 867 (2013), p. 244. doi: [10.1016/j.nuclphysb.2012.10.003](https://doi.org/10.1016/j.nuclphysb.2012.10.003). arXiv: [1207.1303 \[hep-ph\]](https://arxiv.org/abs/1207.1303).
- [72] H.-L. Lai et al. “New parton distributions for collider physics”. In: *Phys. Rev. D* 82 (2010), p. 074024. doi: [10.1103/PhysRevD.82.074024](https://doi.org/10.1103/PhysRevD.82.074024). arXiv: [1007.2241 \[hep-ph\]](https://arxiv.org/abs/1007.2241).
- [73] T. Gleisberg et al. “Event generation with SHERPA 1.1”. In: *JHEP* 02 (2009), p. 007. doi: [10.1088/1126-6708/2009/02/007](https://doi.org/10.1088/1126-6708/2009/02/007). arXiv: [0811.4622 \[hep-ph\]](https://arxiv.org/abs/0811.4622).
- [74] Tanju Gleisberg and Stefan Hoeche. “Comix, a new matrix element generator”. In: *JHEP* 12 (2008), p. 039. doi: [10.1088/1126-6708/2008/12/039](https://doi.org/10.1088/1126-6708/2008/12/039). arXiv: [0808.3674 \[hep-ph\]](https://arxiv.org/abs/0808.3674).
- [75] Steffen Schumann and Frank Krauss. “A Parton shower algorithm based on Catani-Seymour dipole factorisation”. In: *JHEP* 03 (2008), p. 038. doi: [10.1088/1126-6708/2008/03/038](https://doi.org/10.1088/1126-6708/2008/03/038). arXiv: [0709.1027 \[hep-ph\]](https://arxiv.org/abs/0709.1027).
- [76] Stefan Hoeche et al. “A critical appraisal of NLO+PS matching methods”. In: *JHEP* 09 (2012), p. 049. doi: [10.1007/JHEP09\(2012\)049](https://doi.org/10.1007/JHEP09(2012)049). arXiv: [1111.1220 \[hep-ph\]](https://arxiv.org/abs/1111.1220).
- [77] Stefan Hoeche et al. “QCD matrix elements + parton showers: The NLO case”. In: *JHEP* 04 (2013), p. 027. doi: [10.1007/JHEP04\(2013\)027](https://doi.org/10.1007/JHEP04(2013)027). arXiv: [1207.5030 \[hep-ph\]](https://arxiv.org/abs/1207.5030).
- [78] S. Catani et al. “QCD matrix elements + parton showers”. In: *JHEP* 11 (2001), p. 063. doi: [10.1088/1126-6708/2001/11/063](https://doi.org/10.1088/1126-6708/2001/11/063). arXiv: [hep-ph/0109231](https://arxiv.org/abs/hep-ph/0109231).
- [79] Stefan Hoeche et al. “QCD matrix elements and truncated showers”. In: *JHEP* 05 (2009), p. 053. doi: [10.1088/1126-6708/2009/05/053](https://doi.org/10.1088/1126-6708/2009/05/053). arXiv: [0903.1219 \[hep-ph\]](https://arxiv.org/abs/0903.1219).
- [80] Fabio Caccioli, Philipp Maierhofer, and Stefano Pozzorini. “Scattering Amplitudes with Open Loops”. In: *Phys. Rev. Lett.* 108 (2012), p. 111601. doi: [10.1103/PhysRevLett.108.111601](https://doi.org/10.1103/PhysRevLett.108.111601). arXiv: [1111.5206 \[hep-ph\]](https://arxiv.org/abs/1111.5206).
- [81] Ansgar Denner, Stefan Dittmaier, and Lars Hofer. “Collier: a fortran-based Complex One-Loop Library in Extended Regularizations”. In: *Comput. Phys. Commun.* 212 (2017), pp. 220–238. doi: [10.1016/j.cpc.2016.10.013](https://doi.org/10.1016/j.cpc.2016.10.013). arXiv: [1604.06792 \[hep-ph\]](https://arxiv.org/abs/1604.06792).

- [82] J. Alwall et al. “The automated computation of tree-level and next-to-leading order differential cross sections, and their matching to parton shower simulations”. In: *JHEP* 07 (2014), p. 079. DOI: [10.1007/JHEP07\(2014\)079](https://doi.org/10.1007/JHEP07(2014)079). arXiv: [1405.0301 \[hep-ph\]](https://arxiv.org/abs/1405.0301).
- [83] Pierre Artoisenet et al. “Automatic spin-entangled decays of heavy resonances in Monte Carlo simulations”. In: *JHEP* 03 (2013), p. 015. DOI: [10.1007/JHEP03\(2013\)015](https://doi.org/10.1007/JHEP03(2013)015). arXiv: [1212.3460 \[hep-ph\]](https://arxiv.org/abs/1212.3460).
- [84] Matteo Cacciari, Gavin P. Salam, and Gregory Soyez. “The Catchment Area of Jets”. In: *JHEP* 04 (2008), p. 005. DOI: [10.1088/1126-6708/2008/04/005](https://doi.org/10.1088/1126-6708/2008/04/005). arXiv: [0802.1188 \[hep-ph\]](https://arxiv.org/abs/0802.1188).
- [85] G. Cowan. *Statistical data analysis*. Oxford University Press, USA, 1998.
- [86] William T Eadie et al. *Statistical methods in experimental physics*. Amsterdam: North-Holland, 1971. URL: <https://cds.cern.ch/record/100342>.
- [87] G. D’Agostini. “A Multidimensional unfolding method based on Bayes’ theorem”. In: *Nucl. Instrum. Meth.* A362 (1995), pp. 487–498. DOI: [10.1016/0168-9002\(95\)00274-X](https://doi.org/10.1016/0168-9002(95)00274-X).
- [88] Tim Adye. “Unfolding algorithms and tests using RooUnfold”. In: *PHYSTAT 2011*. Geneva: CERN, 2011, pp. 313–318. DOI: [10.5170/CERN-2011-006.313](https://doi.org/10.5170/CERN-2011-006.313). arXiv: [1105.1160 \[physics.data-an\]](https://arxiv.org/abs/1105.1160).
- [89] Tim Adye. *Unfolding algorithms and tests using RooUnfold*. 2011. arXiv: [1105.1160 \[physics.data-an\]](https://arxiv.org/abs/1105.1160).
- [90] Biondi, Silvia. “Experience with using unfolding procedures in ATLAS”. In: *EPJ Web Conf.* 137 (2017), p. 11002. DOI: [10.1051/epjconf/201713711002](https://doi.org/10.1051/epjconf/201713711002). URL: <https://doi.org/10.1051/epjconf/201713711002>.
- [91] Riccardo Di Sipio. “Eikos: a Bayesian unfolding method for differential cross-section measurements”. In: (Aug. 2018). arXiv: [1808.01930 \[hep-ex\]](https://arxiv.org/abs/1808.01930).
- [92] *Luminosity determination in pp collisions at  $\sqrt{s} = 13$  TeV using the ATLAS detector at the LHC*. Tech. rep. ATLAS-CONF-2019-021. Geneva: CERN, June 2019. URL: <https://cds.cern.ch/record/2677054>.
- [93] G. Avoni et al. “The new LUCID-2 detector for luminosity measurement and monitoring in ATLAS”. In: *JINST* 13.07 (2018), P07017. DOI: [10.1088/1748-0221/13/07/P07017](https://doi.org/10.1088/1748-0221/13/07/P07017).
- [94] Florian Bechtel and Peter Schleper. “The Underlying Event in Proton-Proton Collisions”. In: (May 2020).
- [95] Gavin P. Salam. “Elements of QCD for hadron colliders”. In: *2009 European School of High-Energy Physics*. Nov. 2010. arXiv: [1011.5131 \[hep-ph\]](https://arxiv.org/abs/1011.5131).

- [96] P. Nason, S. Dawson, and R.K. Ellis. “The total cross section for the production of heavy quarks in hadronic collisions”. In: *Nuclear Physics B* 303.4 (1988), pp. 607–633. ISSN: 0550-3213. DOI: [https://doi.org/10.1016/0550-3213\(88\)90422-1](https://doi.org/10.1016/0550-3213(88)90422-1). URL: <http://www.sciencedirect.com/science/article/pii/0550321388904221>.
- [97] ATLAS Collaboration. *Optimisation of the ATLAS b-tagging performance for the 2016 LHC Run*. Tech. rep. ATL-PHYS-PUB-2016-012. Geneva: CERN, June 2016. URL: <https://cds.cern.ch/record/2160731>.
- [98] Kunlin Ran. “Study on Simulation of ATLAS ITK Strips”. In: (2016).
- [99] Jon Butterworth et al. “PDF4LHC recommendations for LHC Run II”. In: *J. Phys. G* 43 (2016), p. 023001. DOI: <10.1088/0954-3899/43/2/023001>. arXiv: [1510.03865 \[hep-ph\]](1510.03865).

ERRATA: results presented in Chapter 4 refer to all light lepton combinations ( $ee$ ,  $e\mu$ ,  $\mu\mu$ ) and not only to  $e\mu$  lepton pairs.